



PHD

Increasing wind energy integration into power grids using multifunctional superconducting devices design

Elshiekh, Mariam

Award date:
2020

Awarding institution:
University of Bath

[Link to publication](#)

Alternative formats

If you require this document in an alternative format, please contact:
openaccess@bath.ac.uk

General rights

Copyright and moral rights for the publications made accessible in the public portal are retained by the authors and/or other copyright owners and it is a condition of accessing publications that users recognise and abide by the legal requirements associated with these rights.

- Users may download and print one copy of any publication from the public portal for the purpose of private study or research.
- You may not further distribute the material or use it for any profit-making activity or commercial gain
- You may freely distribute the URL identifying the publication in the public portal ?

Take down policy

If you believe that this document breaches copyright please contact us providing details, and we will remove access to the work immediately and investigate your claim.



UNIVERSITY OF
BATH

Increasing wind energy integration into power grids using multifunctional superconducting devices design

Mariam Elshiekh

A thesis submitted for the degree of Doctor of Philosophy (PhD)
Department of Electrical and Electronic Engineering
University of Bath
2020

COPYRIGHT

Attention is drawn to the fact that copyright of this thesis rests with its author. This copy of the thesis has been supplied on condition that anyone who consults it is understood to recognise that its copyright rests with its author and that no quotation from the thesis and no information derived from it may be published without the prior written consent of the author.

This thesis may be available for consultation within the University Library and may be photocopied to other libraries for the purpose of consultation.

Signature_____

Date_____

Abstract

Electricity generation from wind power plants has increased dramatically during recent decades because of their clean operation, low maintenance, and low running costs. However, integration of wind farms into power grids still has some problems, such as power fluctuations that affect grid stability.

In addition, faults can occur in the power system as a result of a variety of sudden events, such as lightning striking the power line or utility poles shorting the power lines to ground. With higher penetration of wind farms into existing power grids, short circuits could increase to levels that will exceed the switchgear capacity to handle them. The use of fault-current limiters is an urgent requirement to avoid having to upgrade existing protection systems. Although superconducting fault-current limiters (SFCLs) are considered a promising solution to the increasing fault levels, they are still expensive. Integrating the current-limiting function into other superconducting devices will help in mitigating this cost issue. Two superconducting devices have been studied in this thesis and are proposed for limiting fault currents in addition to their primary functions.

The first device is the superconducting fault-current-limiting transformer (SFCLT), which is proposed as a replacement for normal power transformers and superconducting fault-current limiters with the added advantages of lowering losses and volume, and increasing safety compared to normal transformers. The performance of the SFCLT was investigated in relation to the thermal behaviour of the superconducting windings. It works as a low-impedance transformer in normal conditions and as a resistive-type fault-current limiter during fault periods. With incorporation of the SFCLT, the losses of the system decrease and the transformer could limit the high fault currents in the grid within a few milliseconds.

Superconducting magnetic energy storage (SMES) devices are very effective in smoothing wind farm output power because they exhibit large power densities and fast

response times compared to other energy storage devices. However, increasing the fault-current level by adding new wind-generation units to existing power grids can be very harmful to wind power generators and other power system elements. High current levels may destroy the generators and other power system apparatus. Using a fault-current limiter device will be very useful in limiting the fault currents but it will add cost and complexity to the system. Thus, integration of the fault-current-limiting function into the SMES circuit will be a valuable addition to wind turbine systems, and so the second device studied in this research is the superconducting magnetic energy storage fault-current limiter (SMES-FCL). The SMES-FCL is designed to be connected to an AC system that contains a wind turbine generator with a squirrel-cage-type induction motor. The SMES-FCL is used to smooth the output power generated from the wind turbine and compensate the voltage drop to support the load. It is used to limit different types of faults to reduce the short-circuit level of a system and protect the system components from the first cycle.

With the rapid increase in offshore wind farms, there is a need to connect such farms to loads or the grid by DC line. To improve the stability of a DC system that has a wind turbine generator and reduce high fault currents, a DC SMES-FCL is developed and tested. Thus, a control for a wind turbine based on a doubly-fed induction generator (DFIG) is developed and simulated in MATLAB/Simulink software before connection to a DC line. This DC SMES-FCL is tested in different conditions, and the results demonstrate the benefits of using SMES-FCLs in such systems to improve system stability and reduce fault-current levels.

Acknowledgements

Firstly, praise is to Allah, Lord of the Worlds, for providing me with strength and surrounding me with good people such that I could complete this work.

I would like to express my sincere gratitude to my supervisor Prof. Weijia Yuan for his close supervision and his continuous support during my thesis journey. Special thanks to Dr Xiaoze Pei and Dr Min Zhang for their support and constructive discussions during the development of my thesis.

I would also like to thank my colleagues in the applied superconductivity group at the University of Bath with whom I shared a great time: Hamoud Alafnan, Qixing Sun, Dong Xing, Zixuan Zhu, Jiawen Xi, Dr Fei Liang, Dr Yawei Wang, Dr Xiaojian Li and Dr Zhenyu Zhang. With special thanks to Sriharsha Venuturumilli and Muhammad Zulfiqar Ali for their help and support. Thanks too to my colleagues at Strathclyde University: Abdelrahman Elwakeel, Felix Huber, Zhidun Zeng, Fangjing Weng and Tian Lan.

My deep gratitude to my family for their support, love and continuous prayers for me. Thanks to my mother, father, brother and sisters. Special thanks to my small family: my husband Mostafa and my children Zaid and Marya.

Table of Contents

Chapter 1	1
1.1 Introduction to wind energy	1
1.2 Types of wind turbine generators	2
1.3 Challenges of integrating wind energy into power grids	3
1.4 Aims and goals of the thesis	6
1.5 Thesis organization	7
Chapter 2	Superconductivity applications
in electrical power grids	10
2.1 Introduction to superconductivity	10
2.2 Applications of superconductivity to electrical power systems	14
2.2.1 Superconducting cables	14
2.2.2 Superconducting machines (SCM)	16
2.2.3 Superconducting fault-current limiters (SFCL)	17
2.2.4 Superconducting transformers (SCT)	23
2.2.5 Superconducting magnetic energy storage (SMES)	27
Chapter 3	Superconducting fault-current-limiting
transformers	33
3.1 Introduction	33
3.2 Literature review of fault-current-limiting HTS transformers	36
3.3 Transformer design	37
3.4 Transformer cost estimation	41
3.5 Transformer modelling	42
3.6 Model investigation	47
3.6.1 Case 1: One-cycle fault	47
3.6.2 Case 2: Five-cycle fault	50
3.7 Application of a 100 MVA SFCLT to a wind farm power grid	53
3.7.1 Case 1: SLG fault at location A	55
3.7.2 Case 2: SLG fault at location C	57
3.7.3 Case 3: 3PhG fault at location A	57
3.8 Summary	60
Chapter 4	SMES-FCL in AC power systems
4.1	62
4.2 Design aspects and cost-effectiveness of SMES systems	66

4.2.1	The superconducting magnet	67
4.2.2	The refrigeration system	69
4.2.3	Power-conditioning system	70
4.2.4	Operating costs	70
4.3	Applications of SMES in electrical power systems	70
4.4	Literature review of SMES-FCL in power systems	71
4.5	Principle of SMES-FCL operation	72
4.5.1	VSC control	73
4.5.2	DC-chopper control	74
4.5.3	Fault-current-limitation control	75
4.6	SMES-FCL system parameters	76
4.7	Investigation of the SMES-FCL as an energy storage device	76
4.8	Investigation of the SMES-FCL as a fault-current limiter	79
4.8.1	Fault scenario 1: Three-phase-to-ground fault with 0.1 Ω fault resistance	80
4.8.2	Fault scenario 2: Three-phase-to-ground fault with 0.01 Ω fault resistance	83
4.8.3	Fault scenario 3: Line-to-ground fault with 0.1 Ω fault resistance	85
4.8.4	Fault scenario 4: Line-to-line fault with 0.1 Ω fault resistance	88
4.9	Summary	89
Chapter 5		92
5.1	Introduction	92
5.2	Principle of operation of the DC SMES-FCL	93
5.3	Simulation results for DC SMES-FCL	97
5.4	DC quench test of the superconducting coils	99
5.5	Experimental test of the SMES-FCL in a DC system	103
5.6	Application of the DC SMES-FCL in a DFIG-DC system	110
5.6.1	Introduction to DFIG-DC systems	111
5.6.2	System description	112
5.6.3	Control of DC-DFIG	114
5.6.4	Results and discussion	116
5.7	Summary	125
Chapter 6		Conclusions and future work
		126
Refferances		130

List of Figures

Figure 1-1 Some voltage grid code examples	5
Figure 2-1 The Meissner effect [22]	11
Figure 2-2 Superconductivity boundaries	11
Figure 2-3 Magnetization of the types of superconducting materials	12
Figure 2-4 Single-phase cable [35]	15
Figure 2-5 Triaxial three-phase cable [35]	16
Figure 2-6 Resistive-type SFCL	18
Figure 2-7 Shielded-core-type SFCL: (a) set-up scheme; (b) equivalent electrical circuit; (c) magnetic field; (d) electrical circuit [45]	19
Figure 2-8 Bridge-type SFCL [35]	21
Figure 2-9 Saturated-core-type SFCL [47]	21
Figure 2-10 Characteristics of various energy storage devices [66]	30
Figure 3-1 Full-core and partial-core transformers [92]	38
Figure 3-2 Winding arrangements for a 100 MVA HTS transformer	41
Figure 3-3 Transformer-equivalent circuit	42
Figure 3-4 Superconductive winding modes of operation: (a) superconducting state; (b) flux-flow state; (c) normal resistance state; (d) recovery state	46
Figure 3-5 Test system for fault-current-limiting HTS transformer	47
Figure 3-6 Case 1: Current at primary of SFCLT	48
Figure 3-7 Case 1: Current at secondary of SFCLT	49
Figure 3-8 Case 1: Primary and secondary windings temperatures	49
Figure 3-9 Case 1: Primary windings resistance	50
Figure 3-10 Case 1: Secondary windings resistance	50
Figure 3-11 Case 2: Primary-side currents	51
Figure 3-12 Case 2: Secondary-side currents	51
Figure 3-13 Case 2: Primary and secondary windings temperatures	52
Figure 3-14 Case 2: Resistance of the primary windings	52
Figure 3-15 Case 2: Resistance of the secondary windings	52
Figure 3-16 Current limitation (%) of SFCLT w.r.t. stabilizer thickness	53
Figure 3-17 Generation integration with fault-current-limiting transformers	54
Figure 3-18 Case 1: Primary-side currents with and without the limitation effect of the SFCLT	55
Figure 3-19 Case 1: Secondary-side currents with and without the limitation effect of the SFCLT	56
Figure 3-20 Case 1: Temperature of the primary and secondary windings of the SFCLT (the lower figure represents a detailed inset of the upper figure)	56
Figure 3-21 Case 2: Primary-side currents with and without the limitation effect of the SFCLT, and temperature of SFCLT primary	57
Figure 3-22 Case 3: Primary-side currents without SFCLT	58
Figure 3-23 Case 3: Primary-side currents with SFCLT	58
Figure 3-24 Case 3: Secondary-side currents without SFCLT	59
Figure 3-25 Case 3: Secondary-side currents with SFCLT	59
Figure 3-26 Case 3: Primary and secondary windings temperatures	60
Figure 4-1 Different power-conditioning systems for SMES in AC systems: (a) thyristor-based PCS; (b) CSC-based PCS; (c) VSC-based PCS [104]	65
Figure 4-2 Total superconducting costs (\$M) versus stored energy (MJ) [110]	67

Figure 4-3 Three common types of SC magnet: (a) single-solenoid; (b) four-solenoid; (c) toroidal [113]	68
Figure 4-4 SMES-FCL system configuration	73
Figure 4-5 Control sequence of the VSC	74
Figure 4-6 Control scheme of the DC chopper	75
Figure 4-7 Generated power and load power	77
Figure 4-8 SMES current during smoothing output power operation.....	77
Figure 4-9 RMS voltages of the load with and without SMES-FCL following a 100 ms voltage drop at the generator terminals	78
Figure 4-10 SMES current during voltage drop at the generator side.....	78
Figure 4-11 Load voltage with SMES-FCL in the case of a voltage drop at the generator terminals	79
Figure 4-12 Scenario 1: generated currents without using SMES or SMES-FCL	81
Figure 4-13 Scenario 1: generated currents using SMES only	81
Figure 4-14 Scenario 1: generated currents using SMES-FCL	82
Figure 4-15 Scenario 1: RMS voltages at the generator terminals	82
Figure 4-16 Scenario 1: active power generated.....	82
Figure 4-17 Scenario 1: currents in SMES-FCL coils SC1 and SC2	83
Figure 4-18 Scenario 2: generated currents without SMES or SMES-FCL.....	84
Figure 4-19 Scenario 2: generated currents using SMES only	84
Figure 4-20 Scenario 2: generated currents using SMES-FCL	84
Figure 4-21 Scenario 2: RMS voltages at the generator terminals	85
Figure 4-22 Scenario 2: active power generated.....	85
Figure 4-23 Scenario 3: generated currents without SMES or SMES-FCL.....	86
Figure 4-24 Scenario 3: generated currents using SMES only	86
Figure 4-25 Scenario 3: generated currents using SMES-FCL	87
Figure 4-26 Scenario 3: RMS voltages at the generator terminals	87
Figure 4-27 Scenario 3: active power generated.....	87
Figure 4-28 Scenario 4: generated currents without SMES-FCL.....	88
Figure 4-29 Scenario 4: generated currents with SMES-FCL.....	88
Figure 5-1 Circuit configuration of the DC SMES-FCL	95
Figure 5-2 DC SMES-FCL modes of operation	97
Figure 5-3 Load voltage with increase and decrease in the source-voltage value	98
Figure 5-4 Source currents during the DC fault for different coil resistances	99
Figure 5-5 Connection diagram for the DC quench test	100
Figure 5-6 E-J c/cs of the superconducting coil at different locations along the coil	101
Figure 5-7 Current pulse I1 (120 A) and voltage on the tape for the DC quench test.....	101
Figure 5-8 Current pulse I2 (130 A) and voltage on the tape for the DC quench test.....	102
Figure 5-9 Current pulse I3 (140 A) and voltage on the tape for the DC quench test.....	102
Figure 5-10 Experimental set-up (LN = liquid nitrogen).....	104
Figure 5-11 Connection-point voltage with and without SMES-FCL during an increase in the source current.....	105
Figure 5-12 Currents in the connection point and the load during an increase in the source current	105
Figure 5-13 SMES-coil current during an increase in the source current	106
Figure 5-14 Connection-point voltage with and without SMES-FCL during an increase in the source voltage.....	106

Figure 5-15 Currents in the connection point and the load during an increase in the source voltage.....	107
Figure 5-16 SMES-coil current during an increase in the source current	107
Figure 5-17 DC-line current during the current-limitation test	109
Figure 5-18 Connection-point voltage during the current-limitation test.....	110
Figure 5-19 Conventional connection of a DFIG to an AC system	111
Figure 5-20 System configuration for SMES-FCL connection to a DFIG-DC system.....	113
Figure 5-21 Control of the VSC in a DFIG-DC system	115
Figure 5-22 Load power with and without SMES-FCL with variable-speed operation	116
Figure 5-23 SMES current with variable wind-speed operation	117
Figure 5-24 Load voltage with and without SMES-FCL during voltage-drop scenario.....	118
Figure 5-25 Load current with and without SMES-FCL during voltage-drop scenario.....	118
Figure 5-26 SMES current during voltage-drop scenario	119
Figure 5-27 DC current with and without SMES-FCL and with SMES only in stand-alone mode during DC fault (the lower figure represents a detailed inset of the upper figure)	120
Figure 5-28 DC voltage with and without SMES-FCL and with SMES only during DC fault in stand-alone mode	121
Figure 5-29 DC currents with and without SMES-FCL in case of DC fault in grid-connected mode	123
Figure 5-30 Generator-side DC voltage with and without SMES-FCL in case of DC fault in grid-connected mode	123

List of Tables

Table 1-1 Renewable power capacities in 2017 and 2018	1
Table 2-1 Critical temperature and magnetic field values of some LTS materials	12
Table 2-2 Critical temperature and magnetic field values of some HTS materials.....	13
Table 2-3 Summary of some SFCL projects [45] [54]	22
Table 2-4 LTS transformer projects.....	25
Table 2-5 HTS transformer projects.....	26
Table 2-6 Some SMES projects.....	31
Table 3-1 Conceptual SCT schemes	35
Table 3-2 100 MVA transformer design data.....	38
Table 3-3 100 MVA HTS winding parameters	40
Table 3-4 Densities of the tape materials.....	45
Table 4-1 Estimated SMES component cost proportions [111].....	67
Table 4-2 Cost and characteristics of the refrigeration system [107]	69
Table 5-1 Components used in the experimental test.....	103

List of Abbreviations

CSC	Current-source converter
DFIG	Doubly-fed induction generator
DVR	Dynamic voltage restorer
FCL	Fault-current limiter
HTS	High-temperature superconductors
HVDC	High-voltage direct current
LTS	Low-temperature superconductors
LVRT	Low-voltage ride-through capability
PCS	Power-conditioning system
PLL	Phase-locked loop
PMS	Permanent-magnet synchronous
PV	Photovoltaic
PWM	Pulse-width modulation
RSFCL	Resistive-type superconducting fault-current limiter
SC	Superconducting coil
SCM	Superconducting machines
SCT	Superconducting transformer
SFCL	Superconducting fault-current limiter
SFCLT	Superconducting fault-current-limiting transformer
SMES	Superconducting magnetic energy storage
STATCOMs	Static compensators
SVC	Static VAR compensator
SVPWM	Space-vector pulse-width modulation
THD	Total harmonic distortion
VSC	Voltage-source converter
WPP	Wind power plants

Chapter 1

Introduction

The energy plans for many countries for the coming years include a large increase in the share of renewable power generation relative to the total. In 2016, renewable energy accounted for about 18.2% of total global energy consumption and 70% of net additions to global power capacity [1]. During 2017, the world broke a record for the increase in renewable power capacity and also the reduction in its costs. The lead renewable source increase in 2017 was photovoltaic (PV), followed by wind energy. Other types of renewable power generation include hydropower, geothermal, ocean energy and bioenergy. In 2018, 181 GW of power was added to the global market in renewable-energy technologies. Many countries continue to integrate a variety of renewable energy sources. At the end of 2018, more than 26% of global electricity generation was provided by renewable energy sources [1]. Table 1-1 describes renewable-energy power capacities in 2017 and 2018.

Table 1-1 Renewable power capacities in 2017 and 2018

Power	2017 Capacity (GW)	2018 Capacity (GW)
Total renewables	2,197	2,378
- Hydropower	1,112	1,132
- Wind power	540	591
- Solar PV	405	505
- Bio-power	121	130
- Others	18.2	19.3

1.1 Introduction to wind energy

Among the various types of renewable energy sources, wind energy has been the fastest-growing since 1990 [2]. According to the global status report of 2015, wind energy capacity placed second among renewable energy sources, behind hydropower generation, with 370 GW of global capacity in 2014. By 2030, the UK plans to increase the share of

wind energy support to the grid to 20% of the total capacity. In 2014/2015, the total wind power share in the UK electrical grid was 10% of total generation [3]. The UK is now the sixth-largest country for power generated from the wind, after China, the US, Germany, Spain, and India. The total power generated from the wind in the UK in 2014/2015 was 130.313 MW, with a further 20.042 MW in construction and plans in place to add another 12.013 MW.

In cost terms, wind energy is one of the most competitive renewable sources in comparison to fossil fuel energy generation. Indeed, if fuel costs are included as running costs, onshore wind farms will deliver a reduced money-payback period compared to conventional power plants.

In addition, turbine technology has improved during the past decade and high standards have been achieved in their manufacture. In the past, most wind turbines operated as fixed-speed turbines, which caused instability in the grid with very high fluctuations. However, there are now many variable-speed wind turbine types that can be operated with advanced control techniques to reduce the variability in output power and increase system stability.

In addition, in the case of onshore wind farms, they can be built in remote areas or in lands with no need for additional large space. Moreover, offshore wind farms made a great investment from the large water areas with larger efficiency. Despite having higher wind speeds and greater output power than onshore wind farms, offshore farms still have a large capital cost compared to conventional generators. The major cost comes from the cables that connect the wind turbines to the land; transfer of the components and maintenance at sea are other significant extra costs. Therefore, onshore wind farms are more competitive with conventional power generation units from a cost point of view.

1.2 Types of wind turbine generators

Wind farms are divided into several types according to the operational speed of the generator. The two major categories are fixed- and variable-speed wind farms. Fixed-speed wind turbine generators still constitute the majority of the installed base [4]. The generator used on these turbines is the squirrel-cage induction generator. This type of wind turbine operates in a narrow speed range [5]. It also consumes reactive power from

the grid and cannot support the grid during faults. However, fixed-speed wind turbines are cheap, robust, and simple in construction and their principle of operation. The second category is the variable-speed wind turbine generator. This category includes several subtypes, starting with limited-range variable-speed turbines. A wound-rotor induction generator can be used as a variable-speed wind turbine generator by connecting its rotor with a variable resistor and connecting the stator to the main grid. By controlling the energy of the rotor through changes to the resistance value, the generator can operate in a limited speed range about 10% from synchronous speed [6]. In addition to its limited speed range, a drawback of this type is the dissipated heat in the external resistor, which reduces the overall efficiency. The other way to use the induction generator utilises the doubly-fed induction generator (DFIG) concept. In this scenario, the stator is connected directly to the main line and the rotor is connected to a power converter. The speed is controlled by applying suitable voltages to the rotor circuit to obtain a wide-ranging variable-speed operation. The major advantages of this type are that the active and reactive power can be controlled independently, and the rating of the converter is about 20–30% of the stator's rated power. Other variable-speed wind turbines include normal synchronous generators and permanent-magnet synchronous generators. Both of these operate over a wide range of speeds and require a fully rated converter to be connected to the grid. The major advantage of this type is the elimination of a gearbox because the generator is connected directly to the turbine. However, the converter causes increased losses and the generators are large in size [7] [8]. In this thesis, two types of variable-speed wind turbine generators will be used, the squirrel-cage induction generator and the DFIG.

1.3 Challenges of integrating wind energy into power grids

With increasing wind energy integration into power grids, several concerns arose regarding the dynamic and steady-state stability of the grids. The generation of electrical power from wind farms is intermittent in nature because it depends directly on the variable wind speed. With large wind farm installations, this variability in output power could be in the order of gigawatts [9].

Moreover, most wind farms are situated remotely from the principal loads and are often connected to weak grids. The constraints associated with connecting wind farms to weak

grids may include limited thermal capacity in some parts of the grid. In some cases, the development or upgrading of existing transmission systems may be required.

Voltage stability problems appear in any system when the generators cannot meet the demand for reactive power. With a large number of wind turbines still using normal induction generators, voltage stability problems arise because these types of generators cannot support the system with reactive power during grid disturbances, which then affects voltage stability.

Because voltage control is a major requirement in electrical grids, many countries establish a grid code, which defines the constraints required to keep renewable energy sources connected to the grid to support the system during faults [10]. The ability of a system to ‘ride through’ low voltages is called low-voltage ride-through (LVRT) capability. Keeping the generating units connected to the grid during faults or grid disturbances helps the system to restore stability more quickly following the disturbance. The grid codes vary from country to country, and even from operator to operator, depending on the structure and characteristics of the system. Wind power plants (WPPs) must remain connected to the grid during low voltages up to a certain limit defined in the operator grid code [11]. Rapid compensation for the active and reactive power is required in a short period after the fault has been cleared. Examples of some countries’ grid codes are shown in Figure 1-1 [12]. The turbines must remain connected to the grid as the voltage drops at the point of common coupling is above the lines on the figure. They are allowed to disconnect from the grid when the voltage is lower than the relevant line shown in the figure.

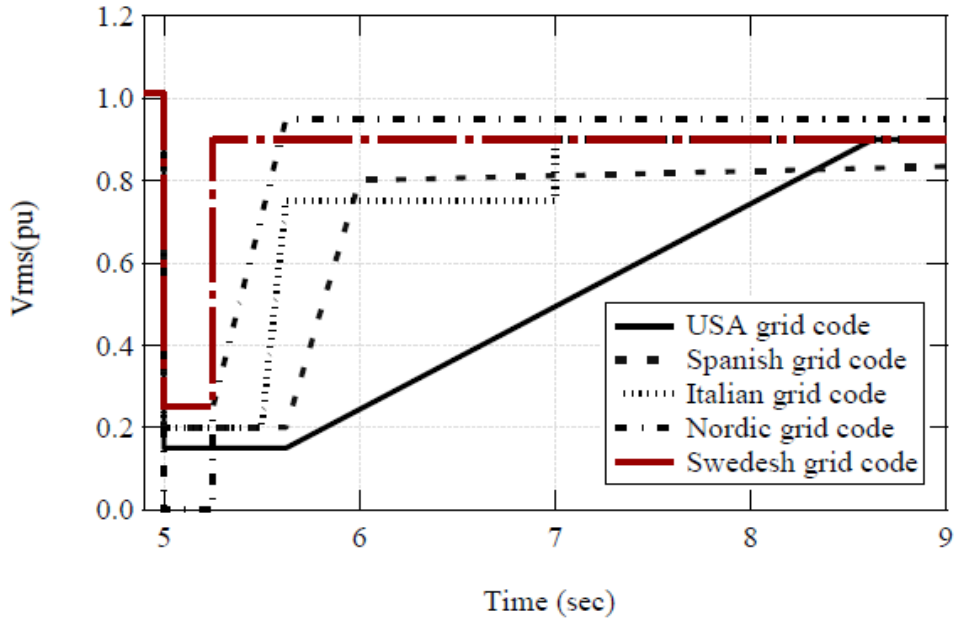


Figure 1-1 Some voltage grid code examples

One of the solutions used to support a system with reactive power is the static VAR compensator (SVC) [13], or static compensators (STATCOMs), which are connected to the point of connection with the grid to control the voltage [14] [15].

Other methods have been used recently to improve the LVRT capability of WPPs and improve system stability. Pitch-angle controllers can be used in the LVRT function of the WPPs. Thus, the wind turbine blades have a pitch-angle controller that increases the blade angle in low-voltage situations, which helps restore the system energy balance [16]. However, the mechanical time delay may cause problems in this method. Another way to ride through the fault in variable-speed wind turbines is the crowbar method. The crowbar is a set of resistors connected by a converter to the rotor side of the wind turbine generator. When a voltage dip occurs, the resistors are inserted into the rotor circuit to prevent high current from passing through the rotor [17] [18]. However, the resistance must be chosen carefully so as to limit the high transient currents without causing high voltages in the rotor circuit. In addition, this method isolates the rotor side of the generator and makes it behave like a squirrel-cage induction generator. The dynamic voltage restorer (DVR) consists of a voltage-source converter connected to the stator of the wind turbine generator and it is used to compensate for the voltage during voltage dips [19]. One of the drawbacks of this method is that the converter has to compensate for the entire stator

voltage in some cases, which increases the rating of the converter and the cost of the system. Adding some control features to the grid-side and rotor-side converters is also used to improve system stability after disturbances [20] [21]. However, this increases the system complexity and is not always able to achieve good performance and protection for the generator at the same time. Another way to improve the LVRT of the WPPs is to use energy storage devices, which will be discussed in the next chapter.

1.4 Aims and goals of the thesis

This thesis proposes the idea of multifunctional superconducting devices to mitigate the disadvantage of the high materials costs and to benefit from the advantages offered by the superconducting materials. These multifunctional superconducting devices are used to limit fault currents in power systems containing wind energy generation units, thus helping to protect the system and reduce the fault-current levels without the need to connect fault-current limiters to the system.

The first part of the thesis involves the development of a detailed model and design for a fully superconducting transformer with a current-limiting function. Both primary and secondary windings are assumed to be superconducting materials and the rating of the transformer is 100 MVA. The transformer model is developed using power system computer-aided design (PSCAD) simulation software and it is applied to limit the fault currents of a wind-farm-based power system.

Then, another multifunctional device is proposed to limit fault currents in addition to storing energy. A superconducting magnetic energy storage fault-current limiter (SMES-FCL) is introduced and tested in AC and DC systems. A new connection and control scheme are proposed to connect the SMES system to a wind-generation system via a three-winding transformer. The new circuit is used to smooth the output power from the wind turbine generator and support the load during disturbances on the generator side. Using this technique eliminates the need for a fault-current limiter in the system, which saves the cost and space required for this additional device.

An SMES-FCL is also designed for DC systems by modifying an H-bridge DC controller by adding electronic switches and developing a new control method. The proposed circuit is used to support the DC load during drops on the generator side and also to limit the

fault currents in the DC side. Using the SMES-FCL in the DC circuit improves the stability of normal operation by smoothing the wind energy output power and supporting the load during voltage drops on the generator side. It also limits fault currents effectively, which protects the system and improves transient stability after fault periods.

1.5 Thesis organization

The remainder of this thesis is organized as follows:

Chapter 2 starts with an introduction to superconductivity. The types of superconducting materials and their characteristics are described. In addition, a brief discussion of the application of superconductivity to electrical power systems is included. A quick literature review of superconducting fault-current limiters, superconducting transformers, cables, generators and magnetic energy storage is presented. After this, a literature review of the use of superconducting devices to solve problems associated with renewable power generation is conducted.

Chapter 3 introduces a modelling and investigation study for a 100 MVA superconducting fault-current-limiting transformer. The chapter's introduction is followed by a literature review of superconducting transformers and their use with the fault-current-limitation function. After that, the design of the transformer is discussed, followed by a detailed description of the model developed with the PSCAD/ Electromagnetic Transients with DC Analysis (EMTDC) software, taking into consideration the thermal and electrical behaviour of the superconducting materials.

This model development is done by integrating the transformer into a simple simulated power system with a generator and a load in series with the transformer. To further investigate the performance of the transformer, the model replaces a normal 100 MVA transformer in a simulated power system incorporating wind power generation. Different fault scenarios are studied and conclusions are drawn accordingly.

Chapter 4 introduces a new scheme for using an SMES system to limit fault currents in AC systems. The chapter's introduction is followed by a discussion of the design aspects and costs of SMES systems. The superconducting magnet, refrigeration system and power-conditioning system are the major elements described in this section. Following

this, the application of SMES systems to electrical power systems is briefly outlined. A literature review of the integration of the fault-current-limiting function into SMES systems is also included.

The operational principle for an SMES-FCL system is then proposed with descriptions of the control schemes for the voltage-source converter, the DC-chopper circuit and the fault-current limitation components. The system is simulated in PSCAD/EMTDC software and a wind-energy-based power system is built and connected to it. The effectiveness of the SMES-FCL system under different scenarios is tested, and the results and conclusions drawn are recorded in the final section of the chapter.

Chapter 5 introduces the idea of using SMES-FCL in DC systems, and the effectiveness of the proposed system is studied in simulated and experimental platforms. Following the introduction, the operational principle of an SMES-FCL in a DC system is described in detail. The proposed system is then tested as an energy storage device and a fault-current-limiting device using MATLAB/Simulink simulation software. A small-scale DC-based SMES-FCL is then described, together with the experimental platform and the parameters of the components used for this system. Using MATLAB simulation, this SMES-FCL is then integrated with a DC system that contains a DFIG-based wind turbine. The effectiveness of this system is evaluated and conclusions are drawn in the last section of the chapter.

Chapter 6 concludes the thesis and summarizes the results obtained. These are discussed and modifications are suggested in the context of a number of recommendations, together with suggestions for further research work to elucidate some of the points raised in this thesis.

Chapter 2

Superconductivity applications in electrical power grids

Superconductors are materials with zero electrical resistance and from which magnetic fields are largely or completely eliminated, which typically occurs at low temperatures. There are many types of superconductor and they can be used in many applications. This chapter provides a brief introduction to superconductivity and the applications of superconductivity to electrical grids.

2.1 Introduction to superconductivity

Superconductivity was first discovered in 1911 by Heike Kamerlingh Onnes, when he observed superconductivity in mercury at very low temperatures. This came three years after he had first liquefied helium, which enabled him to obtain the refrigeration necessary to reach such low temperatures. Onnes subsequently received the Nobel Prize in Physics for his great discovery, in 1913. After that came the significant discovery by Meissner in 1930 of perfect diamagnetism, termed the Meissner effect. Superconductors not only have no magnetic field losses but they also expel all magnetic fields until a critical field value, H_c , is reached. Figure 2-1 illustrates how superconducting materials expel all magnetic field flux lines below the critical value of the magnetic field, as shown in the right-hand picture, while allowing them to cross the material at higher magnetic field values, as in the left-hand picture. Superconductors lose their superconductivity if the magnetic field increases beyond the critical value (H_c) or, alternatively, if the temperature increases above the critical temperature (T_c). Above the critical conditions, the superconductors act like normal conductors, as illustrated in Figure 2-2.

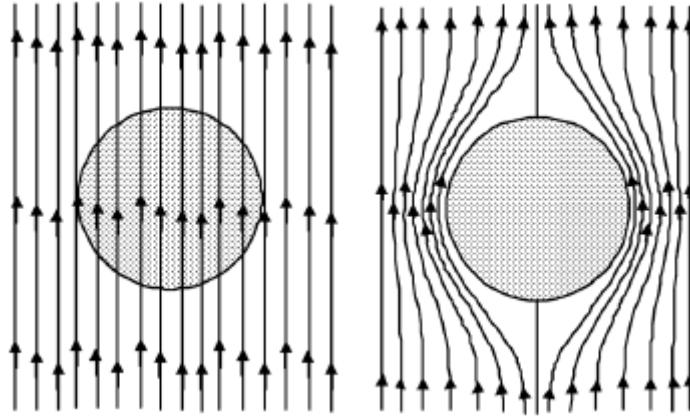


Figure 2-1 The Meissner effect [22]

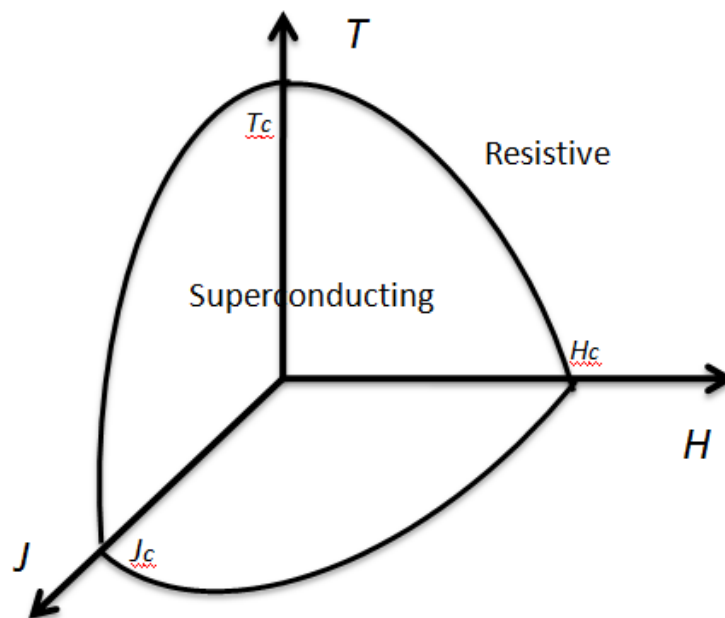


Figure 2-2 Superconductivity boundaries

Superconducting materials can be divided into two main types according to their physical characteristics. The first type (Type 1) expels all applied magnetic fields until a certain critical value (H_c) of the magnetic field. The second type (Type 2) has two critical magnetic field values. Below the first of these (H_{c1}), the material will expel all of the magnetic field. Between this and the second value (H_{c2}), the material will gradually start to lose its superconductivity. In this interval, the magnetic field starts to penetrate isolated

parts of the material (known as vortices), which will lose superconductivity first; when all parts of the material have been penetrated by the magnetic field, it will lose its superconductive state entirely and behave like a normal conductor. Figure 2-3 illustrates the magnetization behaviour of the two types. Low-temperature superconductors (LTSs), which represent the first type of superconducting materials, were discovered first. In this context, the term ‘low-temperature’ means that the material loses resistivity at very low temperatures, such as 20 K (-253 °C). In 1986, the first high-temperature superconductors (HTSs), which represent the second type, were discovered. HTS materials lose their resistivity at much higher temperatures, as high as 138 K (-135 °C) [23]. Examples of some LTS materials and their critical temperature and magnetic field values are listed in Table 2-1 [24], while examples of HTS materials and their critical temperature and magnetic field values are listed in Table 2-2 [25].

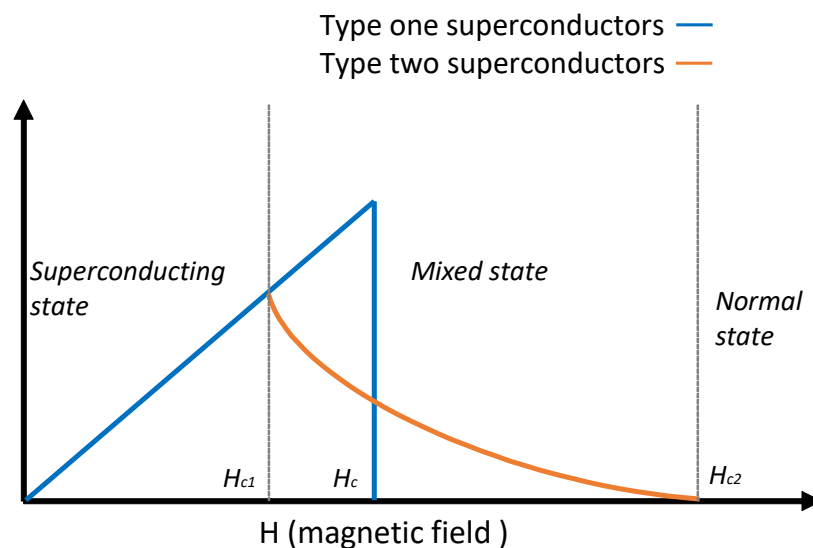


Figure 2-3 Magnetization of the types of superconducting materials

Table 2-1 Critical temperature and magnetic field values of some LTS materials

Material	Critical temperature (K)	Critical magnetic field (T)
Aluminium	1.2	10
Cadmium	0.52	2.8

Indium	3.4	28
Lead	7.2	80
Mercury	4.2	41
Tantalum	4.5	83
Thallium	2.4	18
Tin	3.7	31
Titanium	0.40	5.6
Zinc	0.85	5.4

Table 2-2 Critical temperature and magnetic field values of some HTS materials

Compound	Critical temperature (K)	Critical magnetic field (T)
NbZr	11	8.3
NbGe	23.6	37
NbAl	19.1	29.5
YBaCuO	93	140
BiSrCaCuO	92	107

Following the discovery of superconducting materials, it took some time to establish which were suitable for power applications. Such applications normally need materials that can carry high currents in high magnetic fields. Until 2015, superconducting materials were grouped into 32 classes [26], a ‘class’ being a set of materials of similar

crystal structure, physical properties and composition. In this regard, 1954 saw the discovery of Nb_3Sn , followed by its wire development in 1961 [23]. Later, in 1986, Bednorz and Müller discovered the superconductivity of the compound LaSrCuO at a temperature of 30 K [27]. The next significant milestone in superconductivity progress was the discovery of yttrium barium copper oxide (YBCO), which has a critical temperature of 93 K. Cooling of YBCO to superconductivity levels can be achieved with liquid nitrogen, which has a boiling temperature of 77 K, offering for the first time a much cheaper alternative to the liquid helium and liquid hydrogen previously required, which have boiling temperatures of 4.2 K and 20 K, respectively. HTSs are divided into first-generation and second-generation superconductors. Commercially, the most widely available superconductors are from the first generation, based on bismuth strontium calcium copper oxides (BSCCOs). However, the second-generation (2G) HTSs such as YBCO have many advantages, which increase the opportunities of getting them into the energy market. For example, YBCO tapes are dimensionally compact, with a total thickness of the tape of about 0.1 mm compared to about 0.4 mm for BSCCO-based tape. In addition, the YBCO material can transition sharply from a superconducting state to a normal state within a few milliseconds, which makes it suitable for fault-current-limitation applications. Another advantage is its ability to withstand high stresses, up to 700 Mpa, without any degradation [28]. For these reasons, the YBCO superconductor is the material assumed and used throughout this thesis.

2.2 Applications of superconductivity to electrical power systems

A variety of superconducting materials are used in power applications, including generators, transformers, energy storage, cables and fault-current limiters. Superconducting materials exhibit much larger current densities than normal conductors. This leads to a big reduction in size for devices of similar power ratings [29]. This section provides an introduction to the superconducting devices used up until now in electrical power applications.

2.2.1 Superconducting cables

Superconducting materials are used to carry currents in superconducting cables because they have both a higher capacity and are more compact [30]. Most power cables are

installed underground in special ducts for their protection and maintenance. They are designed to operate at fixed voltages, and the current in them changes according to power demands. Compared with normal cables, superconducting cables have lower resistances and lower power losses. In addition, they have no electromagnetic leakage beyond the shielding layer and pose low reactance. HTS power cables can offer three to five times the electrical power capacity of a normal power cable, with a 50% reduction in transmission losses [31]. Several superconducting cables have already been tested in real grids [32] [33] [34]. Different designs of HTS cable have been developed to minimize the capital and operating costs of the cable. One such design is shown in Figure 2-4 [35], with a configuration based on a single conductor. HTS tapes are stranded around a copper core and surrounded by liquid nitrogen as a refrigerant. At room temperature, this configuration has outer dielectric insulation, which is why it is sometimes called the warm dielectric design [36]. Compared to other designs, this one uses the lowest amount of superconducting material for the same amount of power, but it has a higher inductance. A second design is shown in Figure 2-5. This is called triaxial cable and it has two HTS layers separated by liquid nitrogen, which acts as both coolant and dielectric insulation at the same time. In consequence, it is sometimes called the cold dielectric design. This configuration uses more HTS wires, but it has lower inductance and higher current-carrying capacity. Despite their positive properties, such HTS cables still have some issues in terms of cooling, quench and recovery, and environmental impact.

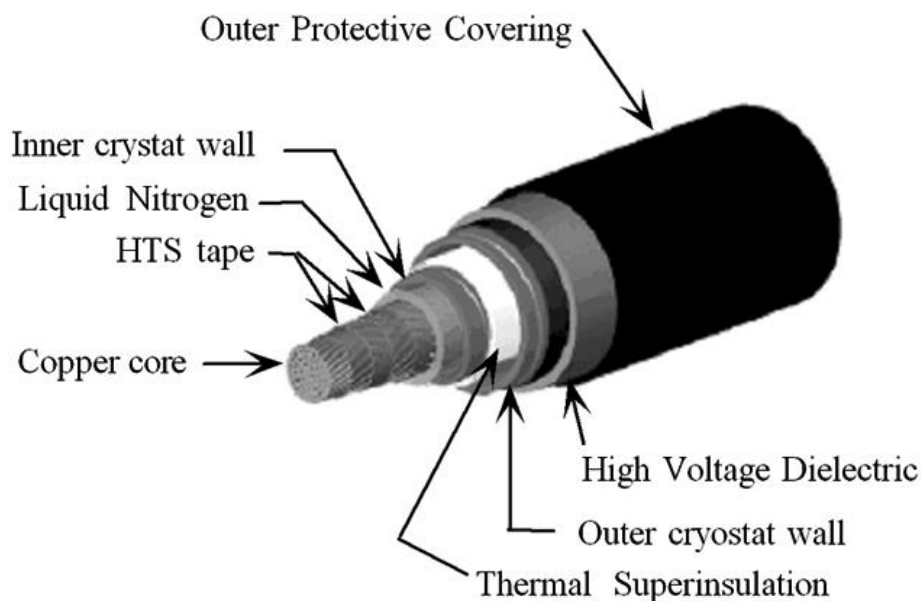


Figure 2-4 Single-phase cable [35]

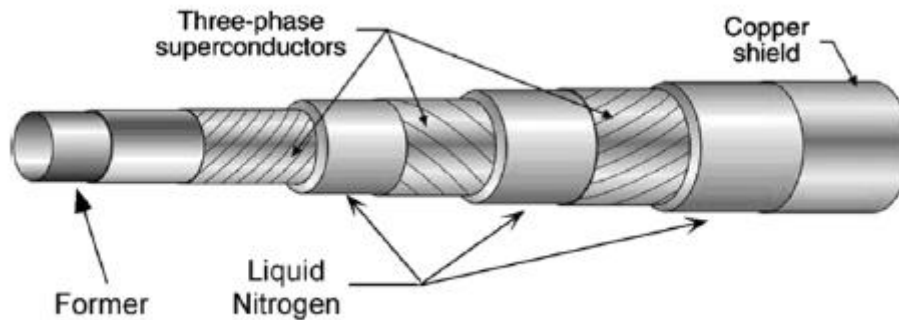


Figure 2-5 Triaxial three-phase cable [35]

2.2.2 Superconducting machines (SCM)

Superconducting generators are considered a promising solution to many issues associated with wind energy. Superconducting materials can be used in building the stators and rotors for the electrical machines. With the low resistance of the superconducting materials, superconducting machines (SCMs) will have low losses and high efficiency [37]. In addition, power manufacturers continually seek to increase the capacity of wind farms in order to maximize their benefits and reduce their costs, especially when placed offshore. The cost of offshore turbines is high, so there is a pressing need to increase the electricity generated by each one, with bigger turbines used to obtain larger ratings.

In addition, direct-drive wind turbines are preferred because of their simplicity and the redundancy of a drive train or gearbox. Such turbines are usually built with normal synchronous or permanent-magnet synchronous (PMS) generators. However, the limitation to the spread of this turbine type is its non-availability for large power ratings, at which the volume and weight of the machine become very high and expense-laden. A 10 MW PMS generator can be 300 tons in weight with a diameter greater than 10 m. However, a generator of the same power rating that uses superconducting windings, designed by American Superconductor (AMSC, Ayer, MA, USA), is only 160 tons in weight [38], and it is claimed that by increasing the rated power of the superconducting

generator wind turbine to 10 MW, the cost will be the same as a PMS wind turbine thanks to the 50% weight reduction, smaller volume and lower losses involved [39].

Many studies have been conducted in the area of superconducting generators. Design of a 15 MW wind turbine generator in Japan was performed using superconducting rare-earth barium copper oxide (REBCO) tapes for the generator windings [40]. The use of superconducting wires as a field winding for large power rating machines has also been performed, using the high flux density that they generate without iron core losses in the design of a 12 MW wind generator [41]. Different methods can be used to build superconducting materials into generators to obtain the most efficient performance [42] [43], such as a salient pole generator, non-salient pole generator, or fully superconducting generator. Further details of superconducting generator types and configurations are available [44].

2.2.3 Superconducting fault-current limiters (SFCL)

Transmission and distribution networks can experience short circuits that may increase the current to 10 to 20 times that of normal system operation. To protect system components against such high currents, several methods have been used to date, the most common being increased-impedance transformers, current-limiting reactors, high-voltage fuses and splitting busbars [45]. However, these methods have the disadvantage of increasing the total impedance of the system during normal operation, which reduces system efficiency. Some methods, such as the fuses, involve component replacement after clearance of the fault, which consumes time and affects system operation and recovery following the fault. These issues raised the need for current-limiting devices that can limit high-current faults in a short time and do not affect a system during normal operation. Superconducting fault-current limiters have been introduced to limit fault currents because they promise near-zero resistance during normal operation and can be returned to normal operational mode after fault clearance without the need for any additional actions. In general, the specifications for a good fault-current limiter are [45]:

- Effective and quick current limitation
- Fast and automatic recovery after fault clearance
- Low impedance during normal operation
- Small size and weight

- Reliable operation under different conditions

Because fault-current limitation is a major object of this thesis, a description of the five major types of SFCL and their operation follows.

2.2.3.1 Resistive-type SFCLs

The pure resistive-type SFCL (RSFCL) is the simplest type of SFCL. It depends directly on the transition from superconductivity mode to resistive mode. The current-limiting element takes the form of a superconducting wire, tape or bulk material in an appropriate quantity according to the system requirements. The superconducting element consists of several layers in parallel. One of these is the superconducting material and the others are elements used as substrate, stabilizer and buffer layer. During normal operation, in which the current passing through the SFCL is lower than the critical current, the resistance of the superconducting material is zero and most of the current passes through it. When the current increases above the critical value, the temperature of the superconducting material also increases, which causes the material to increase its resistance value within a few milliseconds and dramatically reduce the current therein. This action is called the quench. After quenching, the current will pass through the other elements too and the total resistance of the SFCL becomes equal to the equivalent parallel resistance of all the elements. RSFCLs can be divided into several types according to the configuration of the superconducting tape, the major configurations being straight line, pancake and solenoid. Figure 2-6 illustrates the concept of the resistive-type SFCL, where a superconducting material, represented by R_{sc} , is connected in parallel with a shunt resistance (R_{sh}) that represents all the other elements in the superconducting construct.

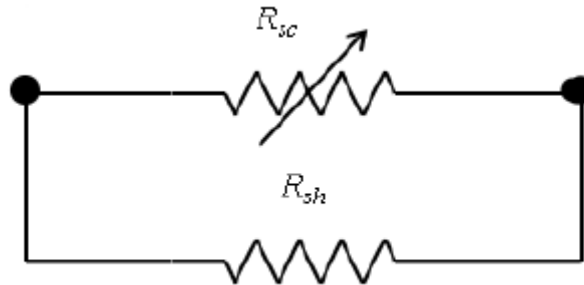


Figure 2-6 Resistive-type SFCL

2.2.3.2 Inductive-type SFCLs

The configuration of an inductive-type SFCL is referred to as a shielded core. It is similar in design to a transformer with its secondary short-circuited. It consists of a copper coil wound around an iron yoke [46]. The superconducting material, in the form of a cylinder, is placed between the coil and the iron yoke. Figure 2-7 illustrates the configuration and electrical circuit of this type of SFCL [45]. When the induced current in the superconducting cylinder is less than the critical current, it acts as a magnetic shielding for the primary winding. In this case, the flux in the iron core is negligible. When the induced current in the superconducting cylinder increases beyond the critical value, the cylinder starts to increase its resistivity. The flux starts to penetrate the iron core and impedance is developed on the primary side, which helps to reduce the high current in the main system. This SFCL type has the disadvantage of bulk, being of a size similar to a transformer, as well as requiring recovery time as the superconducting material inhibits the quench process. However, it has the advantage that there is no need for the current leads and it depends on the magnetic connection only between the superconductor element and the main system.

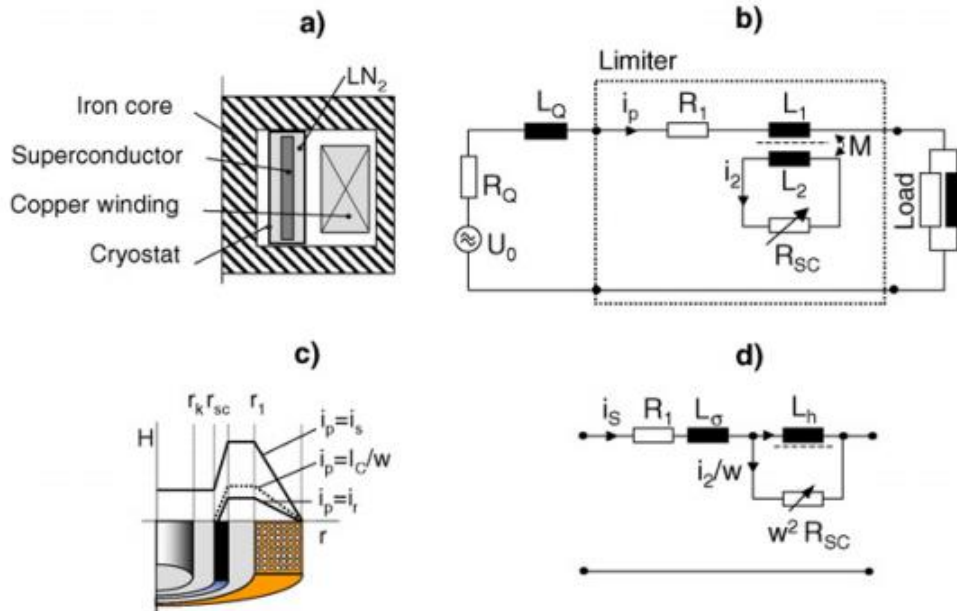


Figure 2-7 Shielded-core-type SFCL: (a) set-up scheme; (b) equivalent electrical circuit; (c) magnetic field; (d) electrical circuit [45]

2.2.3.3 Bridge-type SFCLs

As implied by its name, this type of SFCL uses a bridge from diodes or thyristors beside the superconducting coil and a voltage source. As illustrated in Figure 2-8 [35], the current passing through the limiting inductor (L) must be lower than that in the main circuit (i_{ac}), so the diodes are in an ON state. When the current (i_{ac}) increases above i_o , one pair of the diodes (D_1 and D_2) (or D_3 and D_4) will be turned to the OFF state and the current will be limited by the superconducting inductance.

The advantage of this type of SFCL is the avoidance of a superconducting quench, which means there is no recovery time requirement following fault clearance. In addition, if thyristors are used instead of diodes, the fault current will be limited within the first half-cycle of the fault. The drawback of this SFCL type is that it depends on power electronic switches, so it is not fail-safe.

2.2.3.4 Saturated iron core SFCLs

The saturated iron core type is considered a non-quenching SFCL; it does not need a quenching process to limit the fault current. Two magnetic cores are required, as shown in Figure 2-9. Each one is responsible for a half-cycle of the fault current in an AC circuit. Two coils are wound around the two cores to carry the AC current. A superconducting coil is also wound around the two cores, as shown in Figure 2-9, to carry a DC bias current (I_{dc}). During normal operation, the DC bias current saturates the two iron cores such that the inductance seen on the AC side is negligible [47]. During fault operation, the AC current increases and can force the iron cores out of the saturation state, which leads to an increase of the impedance seen on the AC side and the limitation of the high fault current [48]. Similarly to the shielded-core-type SFCL, the major disadvantage of this type is the need for bulky iron cores. In addition, during fault conditions, an overvoltage could be induced in the DC coil that might damage the DC circuit.

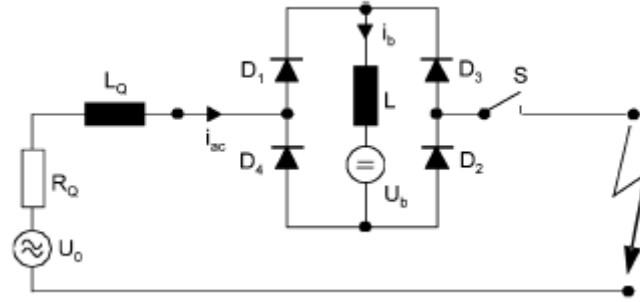


Figure 2-8 Bridge-type SFCL [35]

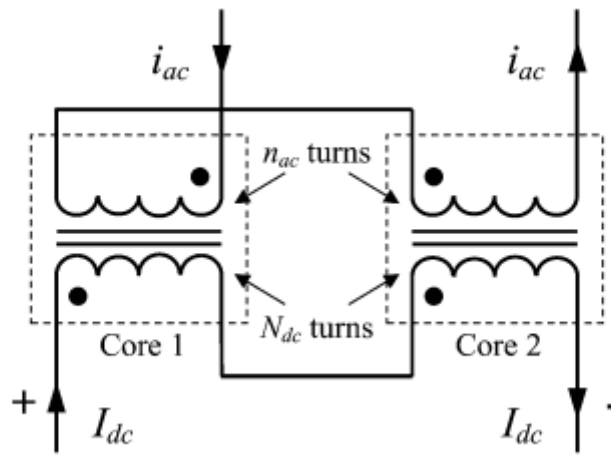


Figure 2-9 Saturated-core-type SFCL [47]

2.2.3.5 Hybrid-type SFCLs

The hybrid-type SFCL is considered a solid-state type because it uses switches in addition to the superconducting material. This hybrid has been proposed to incorporate the advantages of more than one type and avoid their disadvantages. It uses power electronic switches to provide the offline recovery for the superconducting material. A number of designs have been proposed on the basis of this idea [49] [50]. The disadvantage of this type is its use of semiconductor devices, which increases the losses and the cost of the system.

2.2.3.6 Application of SFCLs to power systems

Fault-current limiters (FCLs) can be connected in any part of the electrical power system. They can limit high currents in the transmission, distribution and even the generation parts. Medium-voltage FCLs are required for generation and distribution, while transmission requires high and very high voltage ratings. They can also be applied in isolated grids, such as those on electric ships or electric aircraft. In distribution networks, the SFCL can be used in busbar coupling, generator feeders or the coupling of dispersed generation [45]. Using an SFCL in busbar coupling enables the use of two transformers in parallel, which doubles the short-circuit capacity and enhances system stability [51]. With dispersed generation, instead of the use of additional transformer units to reduce the current level for connection to the transmission system, an SFCL can be used to connect to the distribution grid [51]. Similarly, with added generation units too, instead of upgrading the circuit breakers to cope with the increased short-circuit level, an SFCL can be used to reduce the short-circuit level to comply with the rating of the existing circuit breakers [52]. At transmission voltage levels, SFCLs can also be used in busbar coupling [53] and subgrid coupling [45]. Some projects that have used different types of SFCL and their specifications are listed in Table 2-3 [45] [54].

Table 2-3 Summary of some SFCL projects [45] [54]

Lead company	Country/Year	SFCL type	Data	Superconducting material
ABB	Switzerland/2001	Resistive	8 kV / 800 A	BSCCO 2212 bulk
ACCEL/Nexans SC	Germany/2004	Resistive	6.9 kV / 600 A	BSCCO 2212 bulk
Nexans	Germany/2008	Resistive-inductive	63.5 kV / 1.8 kA	BSCCO 2212 bulk

KEPR	Korea/2007	Resistive	13.2 kV / 630 A	BSCCO 2212 bulk
RSE	Italy/2012	Resistive	9 kV / 3.4 MVA	BSCCO
Zenergy	USA/2009	Saturated core	15 kV / 1.2 kA	BSCCO
Innower	China/2007	Saturated iron core	35 kV / 90 MVA	BSCCO
Innower	China/2012	Saturated iron core	220 kV / 300 MVA	BSCCO
Nexans/ENSYSTROB	Germany/2011	Resistive	12 kV / 533 A	YBCO
Nexans/ECCOFLOW	Spain/2013	Resistive	24 kV / 1005 A	YBCO
Nexans/ECCOFLOW	Slovakia/2013	Resistive	24 kV / 1005 A	YBCO
Nexans	UK/2012	Resistive	12 kV	BSCCO-2212
Shanghai Jiaotong University	China/2012	Resistive	10 kV / 200 A	YBCO
Toshiba/METI	Japan/2009	Resistive	6.6 kV / 600 A	REBCO
LSIS	Korea/2012	Hybrid	22.9 kV / 630 A	YBCO
Chinese Academy of Sciences	China/2004	Rectifier	10.5 kV / 1.5 kA	Bi-2223

2.2.4 Superconducting transformers (SCT)

The introduction of superconducting transformers (SCT) is considered a good solution for reducing total transformer losses. The SCT's windings introduce zero resistance below its critical current. Reducing losses in the transformer leads to reduced operating costs for the transformer and increases its lifetime. It also confers a higher ability to run in an overload condition without affecting the insulation lifetime. In addition, the oil in normal transformers is replaced in SCTs by liquid nitrogen, which makes the SCTs safer when installed in urban areas. The high density of the superconducting wires enables a

reduction in the weight and size of about 40% when compared with normal power transformers of the same power rating [55].

As stated previously, the superconducting materials can be low-temperature ones, which must be operated at temperatures below 10 K, or high-temperature ones, which can operate at temperatures of about 77 K. Although LTSs have low resistance in normal operation, the need to cool them to such low temperatures has so far proved uneconomic. However, the rapid development of second-generation HTS materials has led to encouraging superconducting transformer developments.

One of the most important parameters in developing HTS transformers is the impedance they present to the system in comparison to a conventional transformer. Various projects have recently developed SCTs using high-temperature superconducting materials, and a summary of some of these HTS projects and their associated transformer parameters follows:

- A single-phase HTS transformer is designed with 400 kVA capacity and ratings of 6.3/2.3 kV and 58/174 A for the primary and secondary windings. Two types of transformer were developed by varying the thickness of the stabilizing layer of the YBCO tapes, achieving transformer impedance values of about 15% for the resistive R-type (Ag: 8 μm ; Cu: 300 μm) and 10% for the inductive L-type (Ag: 18 μm ; Cu: 50 μm). Under short-circuit tests, the R-type did not show any decline in fault current over the test period, while the L-type showed a gradual decline in fault current over the test period of 0.2–0.25 seconds [56].
- A three-phase transformer rated at 2 MVA was developed. The windings ratings were 66/6.9 kV and 17.5/167 A. For the stabilizing layer, a GdBCO tape was used with a thickness of 8 μm , comprising only Ag. The impedance of the transformer was 3% and the superconducting tape did not quench immediately even when the applied current increased above the critical value. The quench occurred gradually due to the heat generated by the flux-flow losses [57].
- A single-phase HTS transformer was developed with a power capacity of 1 MVA and winding ratings of 22.9/6.6 kV and 44/152 A. Bi-2223 HTS tape was used for the windings and open- and short-circuit tests were performed on the transformer. The primary and secondary winding resistances were determined to be 2.8 m Ω

and 1.6 m Ω , respectively, and the short-circuit transformer impedance was measured as 4.67% [58].

- Another three-phase transformer was developed by ABB using a Bi-2223 conductor from American Superconductor for the first time. The transformer ratings were 630 kVA, 18.72/0.42 kV and 11.2/866 A, and the impedance was measured as ~4.6%. The performance of the transformer was good up until 418 kVA but beyond this point losses increased and efficiency decreased [59].
- A single-phase 2 MVA transformer prototype was developed to validate the high-voltage terminals, cooling system and other parameters as a first step for developing a 10 MVA transformer. The transformer impedance was measured as 10.34%, and its ratings were 66/6.9 kV and 30.3/290 A.

Lists of both LTS and HTS transformer projects are provided in Tables 2-4 and 2-5, respectively.

Table 2-4 LTS transformer projects

Year	Organization	Country	Power (kVA)	Data	Superconducting material
1985	GEC-Alsthom	France	80	660V/1040V, 124A/77A	NbTi
1988	Kyushu University	Japan	72	1057V/218V, 68A/332A	NbTi
1991	Toshiba	Japan	30	100V/100V, 300A/300A	NbTi
1991	Ktio	Japan	100	6600V/210V, 15A/476A	Cu/NbTi
1992	Kyushu University	Japan	1000	3300V/220V, 303A/4545A	NbTi
1993	ABB	Switzerland	330	6000V/400V, 56A/830A	NbTi
1995	Osaka University	Japan	40	460V/150V, 50A/200A	NbTi

Table 2-5 HTS transformer projects

Country	Installer	Application	Data	Phase	Year	HTS
Switzerland	ABB	Distribution	630 kVA, 18.42 kV / 420 V	3	1997	Bi 2223
Japan	Fuji Electric	Demonstrator	500 kVA, 6.6 kV / 3.3 kV	1	1998	Bi 2223
Germany	Siemens	Demonstrator	100 kVA, 5.5 kV / 1.1 kV	1	1999	Bi 2223
USA	Waukesha	Demonstrator	1 MVA, 13.8 kV / 6.9 kV	1	-	Bi 2223
USA	Waukesha	Demonstrator	5 MVA, 24.9 kV / 4.2 kV	3	2005	Bi 2223
Japan	Fuji Electric	Demonstrator	1 MVA, 22 kV / 6.9 kV	1	2001	Bi 2223
Germany	Siemens	Railway	1 MVA, 25 kV / 1.4 kV	1	2001	Bi 2223
EU	CNRS	Demonstrator	41 kVA, 2050 V / 410 V	1	2003	P: YBCO / S: Bi 2223
Korea	Seoul National University	Demonstrator	1 MVA, 22.9 kV / 6.6 kV	1	2005	Bi 2223
Japan	Fuji Electric	Railway	4 MVA, 25 kV / 1.2 kV	1	2004	Bi 2223
China	IEE CAS	Demonstrator	630 kVA, 10.5 kV / 400 V	3	2005	Bi 2223
Japan	U Nagoya	Demonstrator	2 MVA, 22 kV / 6.6 kV	1	2009	P: Bi 2223 / S: YBCO
Japan	Kyushu Uni.	Demonstrator	400 kVA, 6.9 kV / 2.3 kV	1	2010	YBCO
Germany	KIT	Demonstrator	60 kVA, 1 kV / 600 V	1	2010	P: Cu / S: YBCO
USA	Waukesha	Prototype	28 MVA, 69 kV	3	Not completed	YBCO

Australia	Callaghan Innovation	Demonstrator	1 MVA, 11 kV / 415 V	3	2013	YBCO
China	IEE CAS	Demonstrator	1.25 MVA, 10.5 kV / 400 V	3	2014	Bi 2223
Germany	KIT/ABB	Demonstrator	577 kVA, 20 kV / 1 kV	1	2015	P: Cu / S: YBCO
Japan	Kyushu Uni.	Demonstrator	2 MVA, 66 kV / 6.9 kV	1	2015	GdBCO

2.2.5 Superconducting magnetic energy storage (SMES)

Superconducting magnetic energy storage (SMES) consists of a large coil made from a superconducting material that can absorb or release energy. It can store electrical energy in its own magnetic field generated by the DC current passing through it. It depends on the ability of the superconducting materials to carry high currents without any resistance until reaching its critical magnetic field. Thus the SMES coil provides a combination of energy storage through the inductance principle with no losses through the zero-resistance principle.

Many other devices can be used to store energy in an electrical power system. Brief summaries of energy storage systems and some of these devices are provided below to illustrate the relative advantages and disadvantages of SMES.

2.2.5.1 Energy storage systems

The idea of energy storage first appeared when power stations used to shut down in the first half of the 20th century. The first central station to store energy involved pumped hydroelectric storage and it was put to use in 1929 [60]. The simple operation of electrical systems that transmit electrical energy from the generation unit to the load in real time is no longer sufficient: the demand is not always exactly equal to what is being generated, especially in the case of generation units based on renewables. Thus, high-rating energy storage techniques must also be available. Having large-scale energy storage units

available at all times allows generation units to be built to meet the average electrical demand, not the maximum one. Thus, the benefits of energy storage systems can be following the load, peak power, and standby reserve, as well as for spinning reserve. Energy storage also plays an important role with distributed generation units. Because distributed generation units are often small generators with capacities in kW up to a few MWs, they are not as reliable as large, conventional generators. They are also more likely than conventional generators to have faults and load fluctuations [61]. Energy storage can compensate for any drop in the power, or can supply the load in cases of higher load demands. With renewable-energy supply systems, their intermittent nature and non-controllability raise the urgent need to store the energy they produce and return it to the load when there is any shortfall in generation. Energy storage has many benefits in renewable-energy-based systems, which can be summarized as [62] [60]:

- Mitigation of power delivery constraints that can appear with insufficient transmission capacity
- Time-shifting and shaping of the output energy by storing it in off-peak periods and releasing it during peak periods
- Grid frequency support during any sudden decrease in wind generation
- Reduction of output power fluctuations by charging and discharging energy over short durations.

Some types of energy storage device that are already in use in electrical grids are outlined below:

- Batteries are among the oldest energy storage devices [63]. They store energy in chemical form. Normally, a battery consists of electrochemical cells and each cell contains a liquid, paste or a solid electrolyte with a positive electrode and a negative electrode. The charge and discharge process occurs due to electrochemical reactions between the two electrodes. Batteries can be used in electrical energy storage applications because they have environmental benefits, they can respond rapidly to load changes, and accept co-generated power, which enhances system stability. They also have low standby losses and can have wide range of efficiencies as 60–95% because there are different types of batteries with different characteristics. However, the drawbacks of the battery are that they have low energy density, small power capacity, high maintenance costs, a short cycle life and a limited discharge capability

[60]. Moreover, batteries contain toxic materials that have a detrimental impact on the environment if not disposed of in proper ways.

- Fuel cells also store energy in the form of chemical energy. They need an external supply of fuel and oxidant, and react in the presence of an electrolyte. They can operate continuously if the cell is supplied with the required fuel. An example of a fuel cell is the hydrogen cell, which uses hydrogen as a reactant and oxygen as an oxidant. The major disadvantages of fuel cells are the need for the supply of fuel and their high cost [64].
- The rotating machinery of the flywheel has been used for thousands of years to store energy. These days, in the charging process, the flywheel is spun up by a motor. In the discharge process, the same machinery acts as a generator to generate electricity [65]. The total electricity that can be stored in a flywheel depends on the size and speed of the machine rotor. Flywheels offer a large number of charge and discharge cycles with high efficiency. The major disadvantages of flywheels are their relatively high capital cost, high frictional loss, and low energy density.
- Capacitors can store energy in electrical form. They can be charged very quickly and have tens of thousands of cycles. However, conventional capacitors have low energy density. For the energy density to be higher, the plates of the capacitor need to have a very large area, which makes capacitors uneconomical. However, recent developments in electrochemical capacitors enable high-energy supercapacitors to be built, although self-discharge losses remain a problem in supercapacitors as in conventional ones.

Figure 2-10 summarize some technical characteristics of such energy storage devices.

Compared with other types of energy storage systems, SMES is the only one that can store energy directly in the form of DC current. It has an unlimited number of charging and discharging cycles for a short period of time with a very high efficiency, which reaches 95%. It has a response time of a few milliseconds. These characteristics make it suitable for addressing voltage stability problems and power quality problems in large applications.

However, SMES systems also have some disadvantages, the main ones being their high cost and the negative environmental impact of their strong magnetic fields.

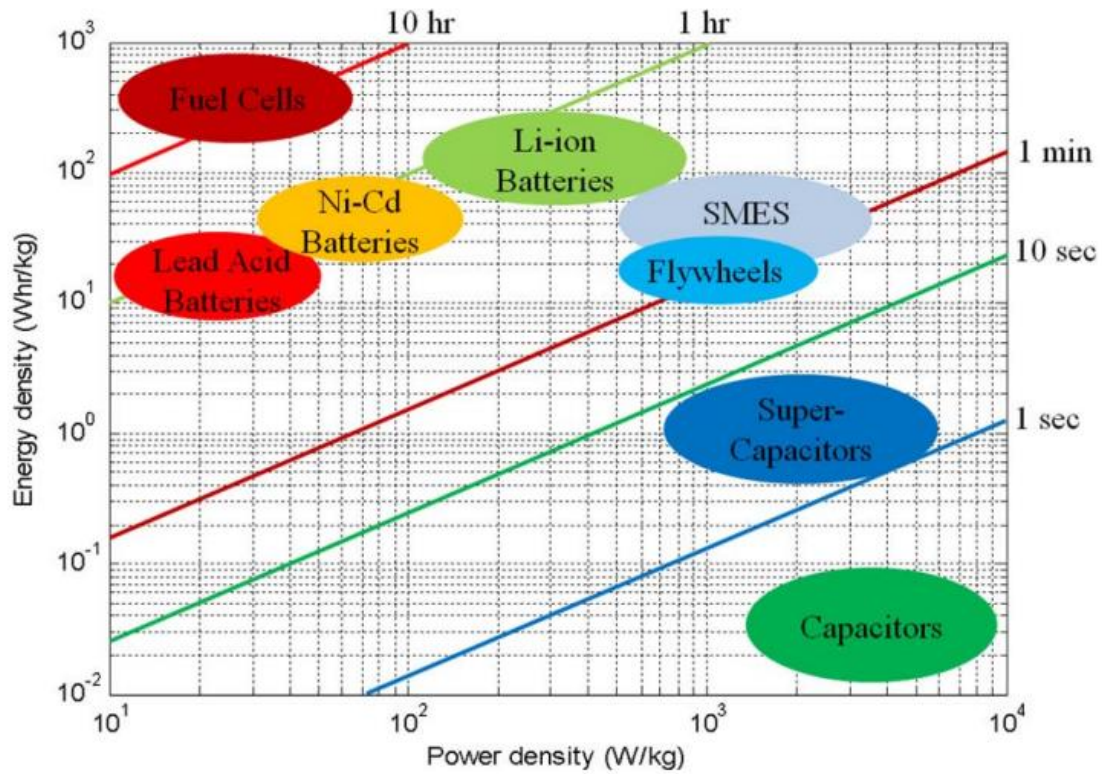


Figure 2-10 Characteristics of various energy storage devices [66]

2.2.5.2 SMES implementations

SMES was first introduced to store electrical energy in 1969 in France [35]. Since then, SMES has been proposed for many applications in electrical power systems. In weak grids, where there is frequent loss of one or more transmission lines, an energy storage device is required to improve system stability. In Wisconsin, USA, American Superconductor built a SMES unit to support its grid. This SMES system consists of seven units and each unit has about 3 MJ energy storage. The whole SMES system can provide the grid with 3 MW for about one second, and reactive power of 8 MVA continuously [35].

Another live project, ‘DRYGRID4SMES’ in Italy, researched and developed a prototype of a cryogen-free SMES system based upon magnesium diboride (MgB_2), and

demonstrated a new method of cooling via a heat exchanger, as opposed to the more common use of liquid at cryogenic temperatures [67] [68].

Japan has also made good progress in SMES projects in recent years. For lightning protection and compensation of the resulting voltage drop, a 5 MVA/5 MJ SMES was developed and its effectiveness was verified [69] [70]. As a next step, a 10 MVA/10 MJ was also developed and tested. Between 2004 and 2007, a 10 MVA/20 MJ prototype for a commercial system was also developed in Japan. This prototype was tested in a real power system to compensate for a fluctuating power load [71].

SMES has been studied in simulated systems to compensate for voltage sags and support the load at the load side [72] [73] [74], with wind energy sources to enhance their transient stability [75] [76], and to minimize the frequency fluctuations for a stand-alone wind farm [77]. It is used to improve system stability in conventional power systems [78]. A SMES system has also been used to reduce the power fluctuations of a single-phase PV system [79]. It is also used with battery energy storage to form a hybrid energy storage system. This helps to increase the lifetime of the batteries, enable a faster response in the overall energy storage system, and reduce the size of the SMES [66] [80]. Some real SMES coils and their parameters are described in Table 2-6 [81], and more projects and prototypes have been outlined elsewhere [69]. Further discussions of SMES system components and design are provided in Chapter 4.

Table 2-6 Some SMES projects

Organization	Year	Country	Data	SC	Application
				material	
Chubu	2004	Japan	1 MVA, 1 MJ	Bi-2212	Voltage stability
CAS	2007	China	0.5 MVA, 1 MJ	Bi-2223	
KEPRI	2007	Korea	0.6 MJ	Bi-2223	Power, voltage

					quality
DGA CNRS	2007	France	0.8 MJ	Bi-2212	Pulse appl.
KERI	2011	Korea	2.5 MJ	YBCO	Power quality
Chubu	2012	Japan	MJ class	YBCO	Grid stabilization
Nexans and others	2011		800 kJ	Bi-2212	High-power pulse sources
Keri	2011	Korea	2.5 MJ	YBCO	
Chubu		Japan	20 MJ	NbTi and YBCO	
ABB and others		US	2.5 MJ		Load levelling

This thesis makes use of three superconducting devices: thus, the concept of fault-current limiters will be used with SCT and SMES devices to improve power system stability and reduce fault currents.

Chapter 3

Superconducting fault-current-limiting transformers

Transformers play an essential role in electrical power grids. They are used with generation units to increase the voltage level and transmit a large amount of power to the grid. They are also used to decrease voltage levels at distribution stations in order to transmit a smaller amount of power to the load as required. Unfortunately, like most power apparatus, transformers suffer many losses, including core losses and no-load losses. This chapter presents the superconducting fault-current-limiting transformer (SFCLT) as an alternative to normal power transformers for connecting wind farms to the power grid. In addition to reducing losses, the SFCLT provides a fault-current-limiting capability to reduce high fault currents.

3.1 Introduction

Transformers are one of the most significant and important pieces of apparatus in power networks. They play a major role in transmission and distribution systems. In the last few decades, power transformers have evolved considerably, reaching efficiencies of up to 99%. However, these transformers are still very bulky, especially for high power ratings. In addition, even with such high efficiencies, in highly rated power applications and under continuous operation, a small improvement of less than 1 % in the efficiency, can reduce the operational cost of the transformers significantly [82].

Another drawback of normal transformers is their use of oil as a coolant. This presents a fire hazard and can also have a negative impact on the environment. In addition, the high weight of such transformers is an important issue when it comes to transportation costs.

With the rapid development of superconducting materials and their unique properties, SCTs are emerging as an alternative to normal transformers. They are lighter in weight and smaller. They also provide higher efficiency, which will, in turn, reduce their running costs. Moreover, they do not use oil for cooling, which enhances their overall safety and environmental impact.

To summarize, the advantages of SCTs can be listed as follows:

- Reduced weight
- Reduced footprint
- Higher efficiency
- Safer because there is no use of oil
- No electrical resistance during normal operation.

With increasing power demands and insufficient space to install additional transformers or upscale existing ones in urban areas, power density must be increased. This could be achieved by connecting transformers in parallel. However, replacing existing transformers with SCTs with smaller footprints and higher power densities would address such increasing capacity issues as SCTs have higher power density compared to normal power transformers.

In addition, because of the increased power capacity, short-circuit levels also continue to increase to ever higher levels. In conventional power transformers, high currents are limited by the high impedance of the transformer itself, which reaches about 20% [83]. However, this leads to high total impedance during normal operation and reduced efficiency. One solution is to insert a superconducting fault-current limiter (SFCL) in series with a conventional transformer [84] [85]. This solution helps to avoid increasing losses in steady-state operation and achieves fault-tolerant performance in a self-operating device. However, this will necessitate the use of two devices, which then does not alleviate the disadvantage of using bulky conventional transformers and incurs additional costs too.

With proper design and a suitable cooling method, the fault-current-limiting function can be added to the SCT to limit high currents, which will reduce the thermal stress on the insulation and avoids the need to upgrade the existing switchgear.

High-temperature superconductor transformers have been proposed to deal with high power densities by lowering the losses in the transmission system and using a more compact design than normal power transformers with a similar rating [58] [86]. However, HTS transformers could offer a reduced impedance compared to conventional transformers, but also have the advantage of a much smaller footprint and a fault-current-

limiting function, that is, a superconducting fault-current-limiting transformer (SFCLT) [56] [57].

The installation of SFCLTs could provide low impedance during steady-state operation in addition to suppressing fault currents to a much lower level, protecting the system and achieving more stable operation during and after faults. SFCLTs are much like normal transformers in construction but have superconducting windings in place of copper ones. During fault conditions, the superconducting windings quench, and the resulting high-resistance path helps to reduce the fault-current magnitude. Table 1 summarizes the available superconductivity schemes for the transformer and the circuit breaker (CB) and the behaviour of the transformer and circuit breaker in each such scheme [83].

Table 3-1 Conceptual SCT schemes

Scheme	Transformer	CB	System
Conventional transformer with CB	High impedance	High duty	Low stability
SCT with CB	Low impedance High efficiency	High duty	Low stability
SCT with CB and SFCL in series	Low impedance High efficiency	Low duty and cost	High stability High cost
SFCLT with CB	Low impedance High efficiency	Low duty and cost	High stability Lower cost

In this chapter, a detailed modelling of a 100 MVA SCT is introduced, together with a study of its effectiveness in limiting fault currents in a power grid containing wind power generation.

The model is developed using PSCAD software, which enables investigation of its behaviour in different power system structures. In section II of the chapter, a literature review summarizes recent research and development in SCTs, including recent projects already carried out. Section III provides a full description of the electrical design of the proposed transformer and its parameters, and section IV briefly considers potential costs. After that, section IV documents the modelling process, with detailed equations

describing the electrical and thermal behaviour of the superconducting windings. The model is first tested, in section VI, in a simple power system where the effects of limits and temperature are investigated and then, in section VII, the SFCLT is modelled as a replacement for a normal 100 MVA transformer in a wind farm-based power system. Finally, section VIII summarizes the chapter.

3.2 Literature review of fault-current-limiting HTS transformers

A review of the literature in relation to fault-current-limiting HTS transformers shows that few studies and prototypes have been conducted as yet. Some that have are summarized below:

- A transformer made from bulk coils as the low-voltage windings was developed and its recovery characteristics were tested [87]. The transformer had copper in the high-voltage windings and the power rating was 2.08 KVA. The rated voltage was 159 V/61 V and the leakage impedance was 4.98%. This transformer used an iron core and it was immersed with the two windings in liquid nitrogen. The cross-sectional area of the iron core was 8.88 cm². When tested, the HTS windings successfully recovered into the superconductivity state following fault clearance. However, with fault currents higher than 14 times the load current on this study, the transformer windings failed to return to superconductivity state after the fault clearance.
- Researchers discussed the steps to develop an SFCLT with a superconducting material used in the low-voltage windings and copper in the high-voltage windings [83]. The steps required to develop a prototype SFCLT using a YBCO HTS were summarized.
- An HTS SFCLT was developed and tested as a 33.3 KVA single-phase transformer [88]. The transformer had ratings of 3810 V/210 V and 8.7 A/159 A (Y- Δ). Only the low-voltage coils were made from HTS tapes, while the high-voltage windings were made from copper wire. Both windings were immersed in liquid nitrogen along with the iron core. In addition, the low-voltage windings were divided into two parts, the first for the transformer function only and the second for the fault-current-limiting function.

- A 2 MVA SFCLT was developed with voltage ratings of 22 kV/ 6.6 kV [89]. The current-limiting ability and recovery characteristics were investigated. The windings of the transformer were made from YBCO HTS material and only a one-phase transformer was fabricated and tested. This transformer had two legs and the windings and the iron core were immersed in liquid nitrogen. The SFCLT exhibited good limitation of the fault current. However, it was concluded that in some cases the HTS windings may continue in normal resistance state and could not return to the superconducting state.
- An SFCLT laboratory demonstrator was tested [90]. The parameters of the transformer were 60 KVA and 1000 V/600 V. The primary windings were made from copper while the secondary windings were made from a YBCO-coated conductor. Both the windings were inserted in a shell-type iron core. The transformer took around 2.3 s to recover its superconducting state.

On the basis of this literature review, it seems that no previous research has been done on configuring both windings as superconducting. Furthermore, the ratings of the transformers studied thus far have not exceeded 2 MVA.

3.3 Transformer design

Power transformers exhibit various types of losses depending on their design and mode of operation [91]. The major cause of loss in transformers are the resistance-related losses in the copper windings (copper losses) during loading periods. The second type of loss is associated with the core and can be divided into hysteresis and eddy current losses. There is also dielectric loss, which comes from the insulation of the transformer, and proximity losses, which derive from the magnetic coupling between the transformer and other metallic objects. These last two are ignored in most studies.

In general, a power transformer can be full-core or partial-core according to the core's size and configuration [92]. The magnetic circuit of a partial-core transformer consists of only the core and air, while that of the full-core transformer consists of the full core with limbs and yokes (see Figure 3-1). A full-core transformer has lower magnetising reluctance because the core surrounds the windings. However, it has more eddy current losses and the overall weight is increased. A partial-core transformer has the advantage of lighter weight and lower eddy current losses, but its magnetizing reluctance is higher.

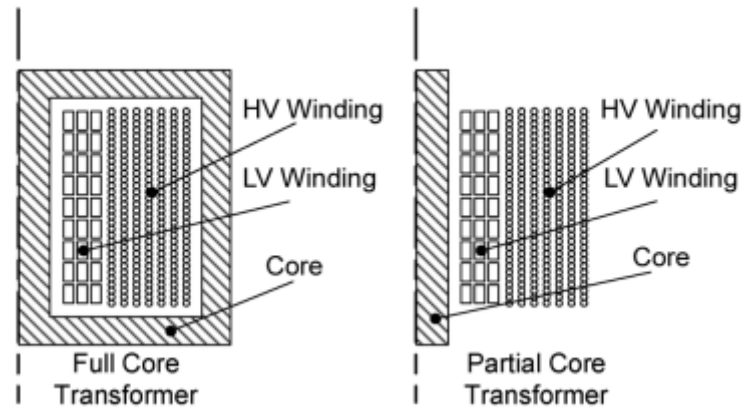


Figure 3-1 Full-core and partial-core transformers [92]

Using SCT to replace conventional power transformers directly reduces the copper or windings losses. SCT transformer designs can be based on hybrid approaches with low-voltage windings being high-temperature superconducting, and high-voltage windings either being copper or fully superconducting, making both windings HTS. For the work of this thesis, fully (HTS) superconducting windings are assumed, to minimize losses therein.

To reduce core losses, the best solution is to reduce the core size, so a partial-core design is assumed here given the advantage of the superconducting winding in having a higher magnetisation effect than the same number of turns of copper, which means compensating the magnetisation reduction by replacing a full core with a partial one.

Table 3-2 provides the design target and general parameters for an HTS transformer as estimated on the basis of an existing 100 MVA transformer [93].

Table 3-2 100 MVA transformer design data

Rating	100 MVA
Type	3-phase
Rated voltage	154 / 22.9 kV
Current	0.37 / 2.5 kA
Iron core	1.4 T

Frequency	50 Hz
Cooling	LN2
Impedance	10–15%
Estimated dimensions	7.6 m × 5 m × 2.5 m
Weight	< 35 ton

For the design of the HTS transformer, the critical current density of the coated conductor is about 300 A/cm at 77 K [94] [95]. The perpendicular component of the magnetic field at the coil ends is estimated to be 0.18 T, which could reduce the critical current of a 2G HTS to 200 A/cm.

For the SFCLT design, larger operating currents are anticipated. To achieve this, several superconducting tapes must be connected in parallel. The length of the tape is determined by the maximum endurable quenching voltage. Elsewhere, several tests have been conducted to determine the maximum endurable quenching voltage in relation to tape lengths and fault durations [96]. Assuming the transformer windings must withstand a high fault current for a period of 200 ms with a peak voltage per unit length of 0.595 V/cm, the winding length can be calculated as follows:

$$\text{Total length} = \text{Rated voltage} \times \text{maximum peak voltage per unit length}$$

For the primary windings, the rated voltage is 154 kV, so the tape length can be calculated by dividing the rated voltage by the maximum endurable quenching voltage, giving a result of 2.5 km. The secondary windings can be calculated in the same way to give a result of 385 m. . While the number of tapes per each side can be calculated as follows:

$$\text{Number of tapes} \sim \text{windings rated current} / \text{critical current}$$

For a primary winding with a rated current of 370 A, eight tapes are connected in parallel based on the assumption that the maximum magnetic field to be reached is 1 T and the critical current of a single tape under 1 T is about 50 A. The same principle can be applied to the secondary winding, which requires 50 tapes in parallel to attain a rating of 2.5 kA. In the primary, each winding element has the eight tapes connected in parallel, with 215 turns in the axial direction and 15 in a radial direction. In total, there are 3,255 turns for the primary winding. The winding depth is about 1 m when assuming 1 mm between each

element. The winding thickness is 0.04 m when assuming a thickness for each tape with insulation of 0.25 mm.

For the secondary winding, there are 240 turns in the axial direction and two turns in the radial direction, giving a total of 480 turns. The winding depth is about 1.212 m, given a 1 mm gap between each element, and the winding thickness is 0.025 m, considering a thickness for each tape with insulation of 0.25 mm. The winding parameters are summarized in Table 3-3 and the winding arrangements are shown in Figure 3-2. . The price of the windings only is estimated based on the recent average tape cost of 30 \$/m.

Table 3-3 100 MVA HTS winding parameters

HTS property	YBCO-coated conductor
Thickness	0.1 mm
Width	4 mm
Stabilizer	Copper, 40–100 μm
Hastelloy substrate	60 μm
Critical current	50 A
Primary winding	8 tapes in parallel, 2.6 km minimum length
Secondary winding	50 tapes in parallel, 385 m minimum length
Total HTS length for primary	20.8 km
Total HTS length for secondary	19 km
Estimated cost of HTS windings	\$1.2 million

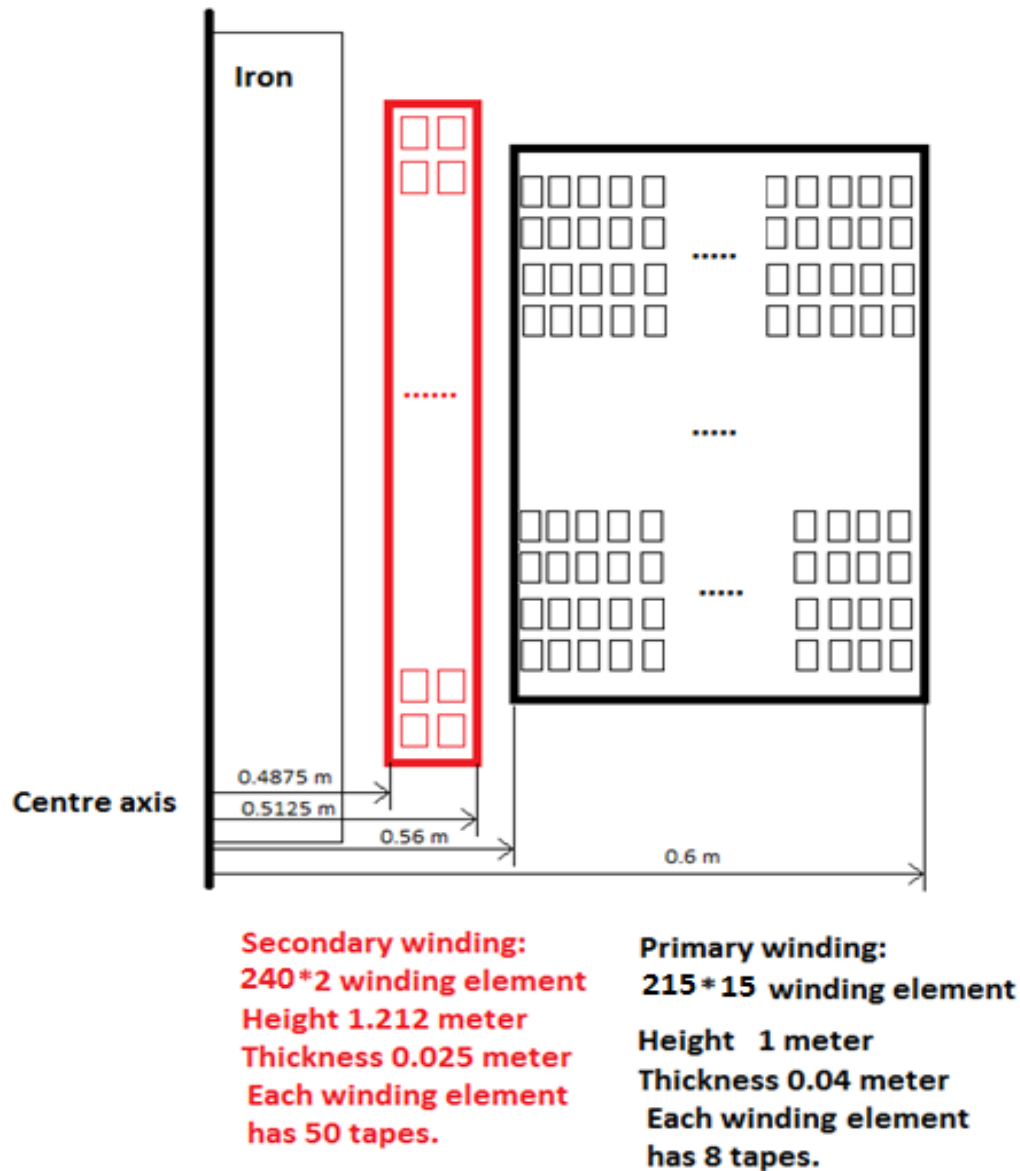


Figure 3-2 Winding arrangements for a 100 MVA HTS transformer

3.4 Transformer cost estimation

The cost of an HTS transformer is difficult to estimate because it depends on many parameters. The first such factor is the amount of HTS material. A cost comparison elsewhere concludes that for transformers of medium-MVA ratings, HTS transformers may be cost-competitive with normal power transformers [19]. The same study states that the initial cost of an 18 MVA HTS transformer is about \$621,000, while that of a 24 MVA conventional transformer is about \$550,000. The core loss and the load loss in the HTS transformer account for \$32,500 and \$32,000, respectively, while the core loss and the

load loss in a conventional transformer account for \$42,500 and \$150,000, respectively. With normal transformers, there are also costs for fire suppression and an oil containment pit, which account for \$130,000 and are unnecessary in HTS transformers. Overall, these findings indicate that the total cost of an 18 MVA HTS transformer is \$866,500 and that of the 24 MVA conventional transformer is \$872,500.

3.5 Transformer modelling

With the impedance offered by HTS transformers being less than that of conventional transformers and having the added advantage of a much smaller footprint, a fault-current-limiting function incorporated into the transformer would be beneficial. Under fault conditions, in superconducting transformers using HTS tape with a stabilizing layer, the resistance of the windings will be defined by the resistance offered by the stabilizing layer as the superconducting layer gets quenched. Hence the impedance value will increase significantly and in turn decrease the amplitude of the fault current. The amplitude at which the fault current is stabilized can be calculated through the resistance offered by the stabilizing layer.

The model is based on a standard transformer with the primary and secondary windings represented by series-connected impedances. Both sides are assumed to be superconducting windings. The stabilizer is a copper stabilizer and tapes are connected in parallel according to the critical current of the superconducting material. The equivalent circuit of the transformer is represented in Figure 3-3.

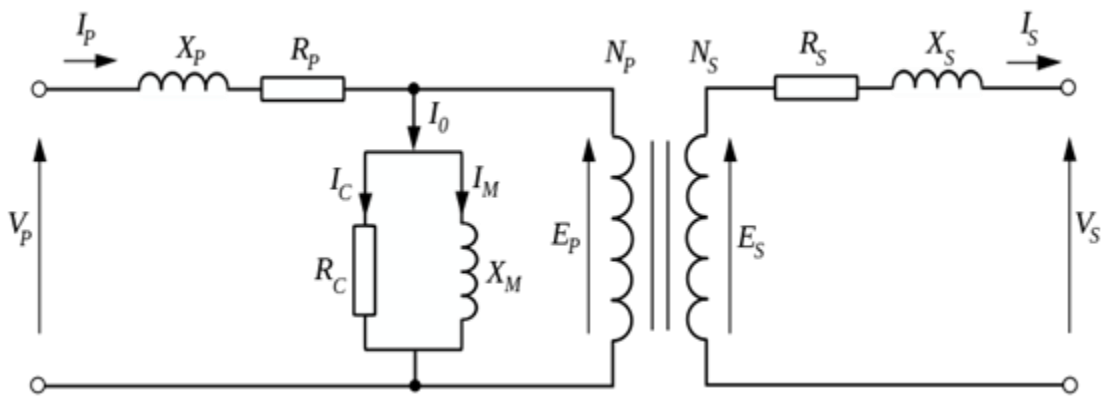


Figure 3-3 Transformer-equivalent circuit

The series impedances consist of windings resistances (R_p and R_s) and windings leakage reactances (X_p and X_s). Whereas the resistance value depends on the type of material used, the reactance value depends on the design of the transformer. In the case of

superconducting materials, the winding resistance is negligible under normal operating conditions.

The operation of the SFCLT is divided into three modes according to the value of the resistance, in addition to the recovery to the superconducting state. The superconducting mode represents zero resistance and, therefore, the winding resistance can be ignored during normal operation.

The main parameters that define the resistance value during the different operational modes are the critical current density (J_c) and critical temperature (T_c) [97]. The critical current density at which quenching occurs is given by:

$$J_c(T) = J_{co} \left(\frac{(T_c - T(t))^\alpha}{(T_c - T_o)^\alpha} \right) \quad (3-1)$$

where J_{co} is the critical current density at the initial temperature T_o which equals 77 K, α is the density exponent and equal to 1.5, and T_c is the critical temperature; Equation 1 is valid for $T < T_c$.

As can be seen from Equation 1, with an increase in temperature, the value of the critical current changes accordingly. With zero resistance, the power dissipated in the windings can be ignored. As the resistance value increases, the power dissipated starts to manifest according to the following equation:

$$P_{diss}(t) = i(t)^2 R_{sc}(t) \quad (3-2)$$

where R_{sc} is the resistance of the superconducting winding, and $i(t)$ is the current passing through it.

To keep the temperature of the windings below the critical value under normal conditions and reduce the temperature rise during or after high current flow, a coolant is used. There are several cooling methods for superconducting materials, which directly affect the winding behaviour. A liquid nitrogen coolant is assumed for this design and the entire area is immersed in it. The cooling power is calculated by:

$$P_{cooling}(t) = h A(T(t) - T_o) \quad (3-3)$$

where h is the heat transfer coefficient, $T(t)$ is the temperature, and A is the surface area that is covered by the coolant. The heat transfer coefficient h changes with the change in the temperature. When the temperature equals the initial value in normal operation mode,

the cooling power equals zero. The heat transfer between the windings and the liquid nitrogen is considered to be the major factor affecting the recovery period of the windings, which means cooling them down and restoring their superconductive state. To consider the impact of the recovery period, the heat coefficient equations are taken as a function of the temperature rise, as follows [98] [99]:

$$\begin{aligned}
 h &= 125 + 0.069 * \Delta T, & 56.3 \leq \Delta T \leq 214, \\
 h &= 12292.13 - 709.32 * \Delta T + 14.735 * \Delta T^2, & 18.94 \leq \Delta T < 56.3, \\
 h &= 82.74 - 131.22 * \Delta T + 37.64 * \Delta T^2, & 4 \leq \Delta T < 18.94 \\
 h &= 21.945 * \Delta T, & 0 \leq \Delta T < 4
 \end{aligned} \tag{3-4}$$

The cooling assumption is that the entire HTS winding is fully covered by liquid nitrogen during the quenching process. The net power in the windings, P_{sc} , is:

$$P_{sc}(t) = P_{diss}(t) - P_{cooling}(t) \tag{3-5}$$

The temperature of the superconducting windings is calculated via the following equation:

$$T(t) = T_o + \frac{1}{C_p} \int_0^t P_{sc}(t) dt \tag{3-6}$$

where T_o is the initial temperature of the material, which is taken as 77 K, and C_p (J/K) is the heat capacity of the material. The heat capacity of the material represents how many Joules are generated in the winding for each one-Kelvin increase in temperature. Because the generated energy depends on the mass and the specific heat capacity of each material, the heat capacity of each material is calculated individually by multiplying its density and volume by its specific heat value [100].

In terms of the YBCO material that represents the superconductor, its heat capacity is approximated by the following linear equation:

$$C_p = 2T * d * \text{volume} \tag{3-7}$$

where T is the temperature and d is the density of the material. This equation is obtained by approximation of the actual figure of the heat capacity [100]. The Hastelloy heat capacity ($C_{p_{hts}}$) can be calculated from Equation 6. The copper heat capacity variation

with temperature is small and is ignored here. Thus, the heat capacity of the copper material is calculated directly from:

$$C_{pcu} = C_{cu} * d_{cu} * \text{volume} \quad (3-8)$$

where C_{cu} is the heat capacity of copper, taken as 368.5 J/kg.k, and d_{cu} is the density of the copper.

Table 3-4 shows the densities values for each of the tape materials. The three heat capacities are added together to determine the total value:

$$C_p = C_{phts} + C_{pcu} + C_{psub} \quad (3-9)$$

Table 3-4 Densities of the tape materials

Material	Density (kg/m³)
YBCO	5,900
Copper	8,940
Hastelloy	8,910
Kapton insulation	1,420

The volume of the superconducting windings is calculated as follows:

$$\text{volume} = \text{length} * \text{thickness} * \text{width} * \text{number of turns} \quad (3-10)$$

Again, the heat capacity variation with temperature of the copper, which represents the stabilizer layer, is small and is ignored here, while the substrate heat capacity can be calculated, as per the YBCO material, from Equation 3-6. The total heat capacity is calculated by adding together the values for the three materials.

When the current passing through the transformer windings exceeds the critical current, the winding resistivity starts to increase to very high values, according to the following equation:

$$\rho_{HTS} = \frac{E_c}{J_c(T)} \left(\frac{J}{J_c(T)} \right)^{N-1} \quad T < T_c, J > J_c \quad (3-11)$$

When the temperature reaches its critical value, it will be in the normal resistive mode. During normal mode, the value of the resistance is determined only by the value of the stabilizer resistance because the superconducting material resistance becomes very low. The resistivity of the copper changes with temperature according to:

$$\rho_{cu} = (0.0084T - 0.4603) \times 10^{-8} \quad T > T_c \quad (3-12)$$

and the total resistance can be calculated from the normal equation:

$$R_{sc} = \rho_s \frac{l}{A} \quad (3-13)$$

where l is the length and A is the area of the superconductor. To best describe the resistance of the superconducting windings, Figure 3-4 shows the four zones of resistance. Zone (a) is the superconducting mode where the resistance is close to zero; zone (b) is the flux-flow mode where the current is above its critical value, but the resistance is still below its critical value. In this mode, the resistance increases sharply, in about 2 ms. When the temperature reaches its critical value, the normal resistance of zone (c) starts, with resistance determined by temperature. Once the current decreases below the critical value, the recovery period begins, represented on the figure by zone (d), which indicates the time taken by the material to cool down again and restore superconductivity.

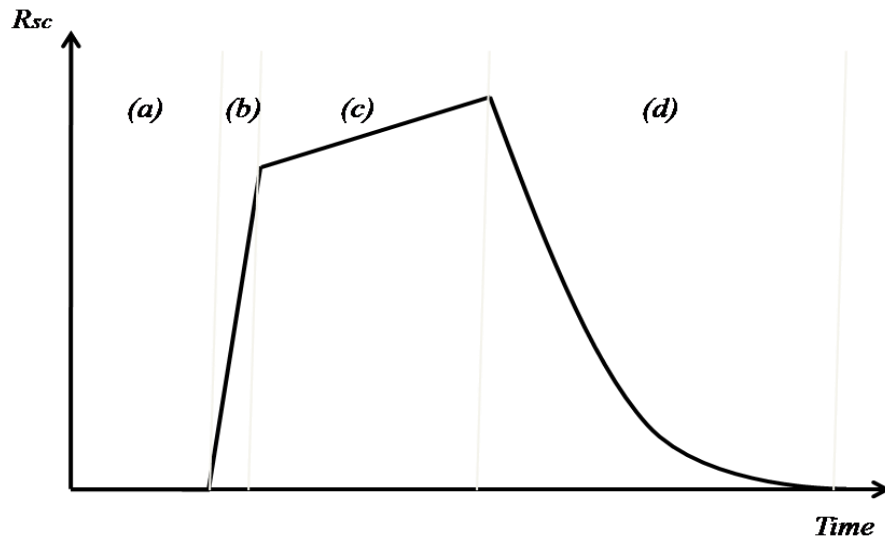


Figure 3-4 Superconductive winding modes of operation: (a) superconducting state; (b) flux-flow state; (c) normal resistance state; (d) recovery state

3.6 Model investigation

To investigate the model, a simple power system is built using the PSCAD software, as shown in Figure 3-5. It consists of a power source, transmission line resistance, and the load, which is represented by a $0.5\ \Omega$ resistor.

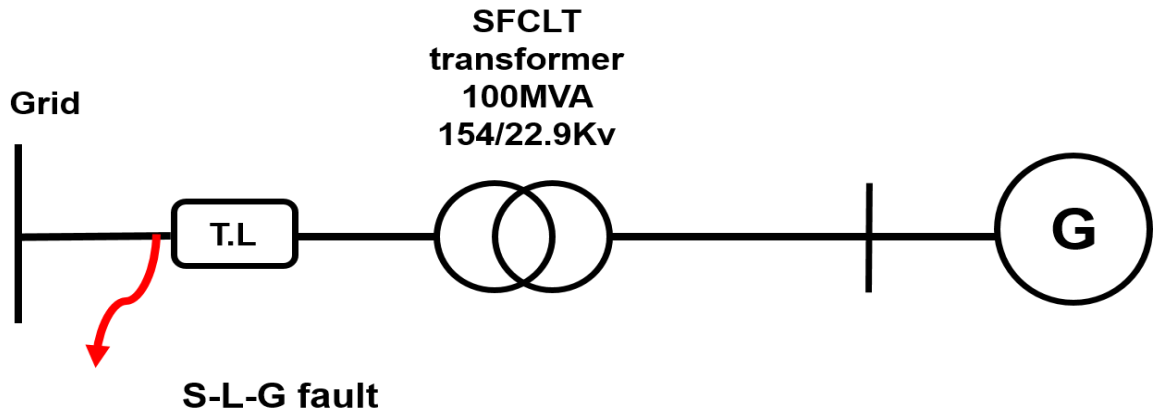


Figure 3-5 Test system for fault-current-limiting HTS transformer

A standard transformer model is used with series-connected impedances representing the primary and secondary windings. Both sides are assumed to be superconducting windings. The stabilizer is a copper stabilizer and tapes are connected in parallel according to the critical current of the superconducting material.

This section describes case studies of the SFCLT under different short-circuit periods. The cases considered are durations of one cycle and five cycles for a single-phase line-to-ground fault for phase A. The results of the SFCLT simulations are compared with the prospective current values if the limiting element were absent. Finally, the stabilizer thickness is changed from 40 to 100 μm to determine the recommended thickness value.

3.6.1 Case 1: One-cycle fault

A single line-to-ground (SLG) fault is applied on the load side for only one cycle (20 ms) duration to investigate the limitation action within a short fault period. The stabilizer thickness used in this case is 40 μm . Figure 3-6 illustrates the primary-side currents with the limitation action and the prospective current value. This figure shows that using an

SFCLT with a stabilizer thickness of 40 μm limits the current's first peak to ~ 2.4 kA from a prospective current of ~ 3.8 kA on the primary side, meaning that it is limited to 62% of the prospective value. Moreover, after the first peak, the percentage limitation increases and the current only reaches about 30% of the prospective value during the remainder of the fault period.

In addition, the secondary-side currents are limited effectively by the SFCLT. As visible in Figure 3-7, the first peak current is reduced from a prospective value of 25 kA to 16 kA. The increase in the winding temperature is a very important parameter in the transformer design. Figure 3-8 shows the temperature of the primary and secondary windings. The temperature rise in the secondary side is greater than in the primary, reaching about 300 K in this case, while the maximum temperature for the primary side during the fault is 250 K. The windings take about 200 ms to cool down and return to the initial temperature, which is 77 K. The resistances of the primary and secondary windings are shown in Figure 3-9 and Figure 3-10, respectively. The operational modes of the superconducting materials discussed in section III of this chapter are clearly visible in these figures. Before the fault instance (at 2.5 s) the resistance can be neglected. After the fault starts, the resistance begins to increase rapidly to reach more than 30 Ω in the primary and about 1 Ω in the secondary. These values correspond to the flux-flow mode in which the resistance increases to its normal value within a few milliseconds.

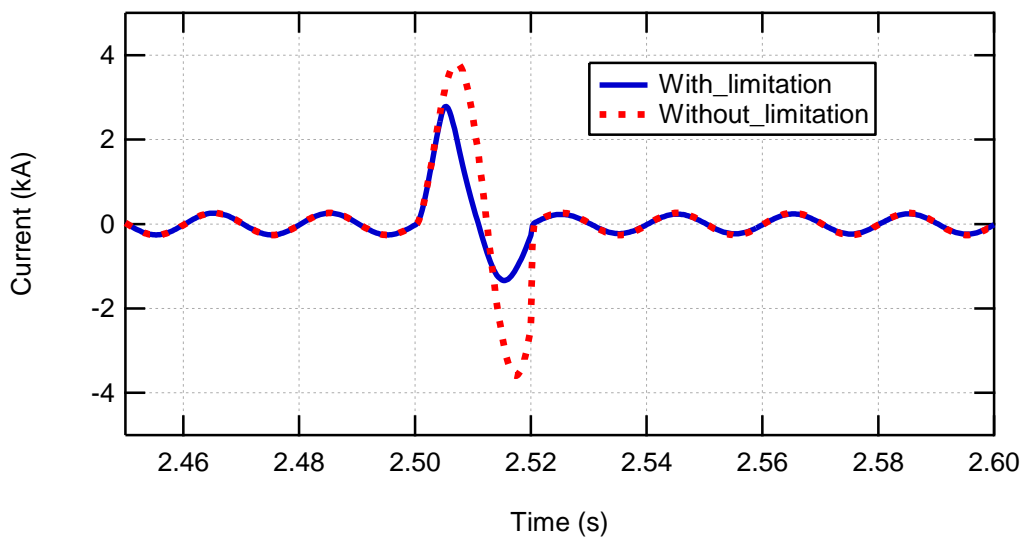


Figure 3-6 Case 1: Current at primary of SFCLT

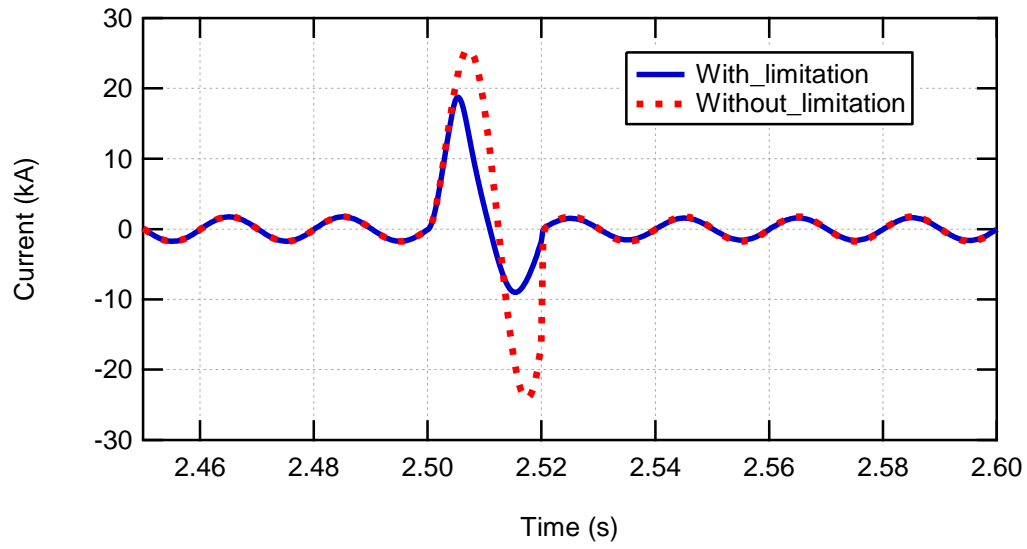


Figure 3-7 Case 1: Current at secondary of SFCLT

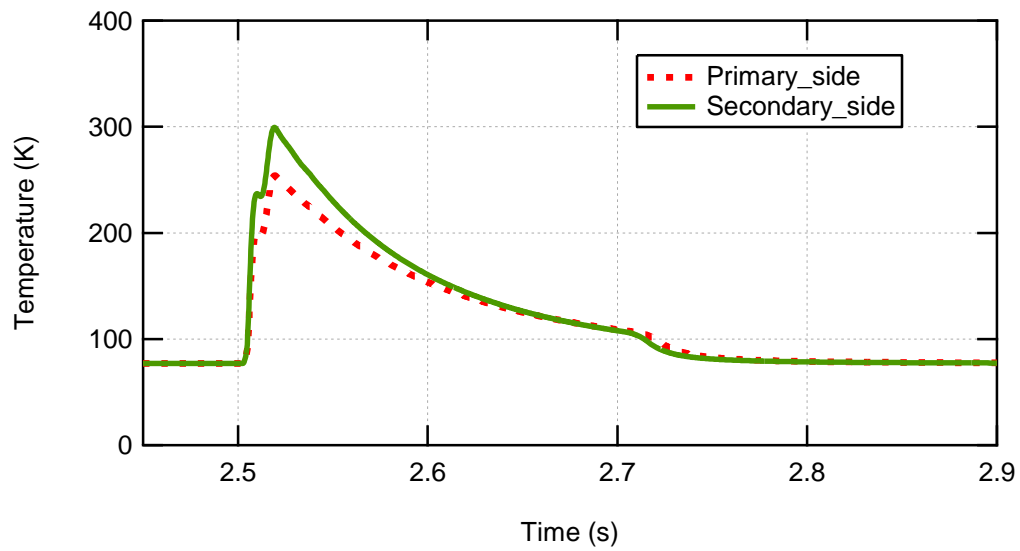


Figure 3-8 Case 1: Primary and secondary windings temperatures

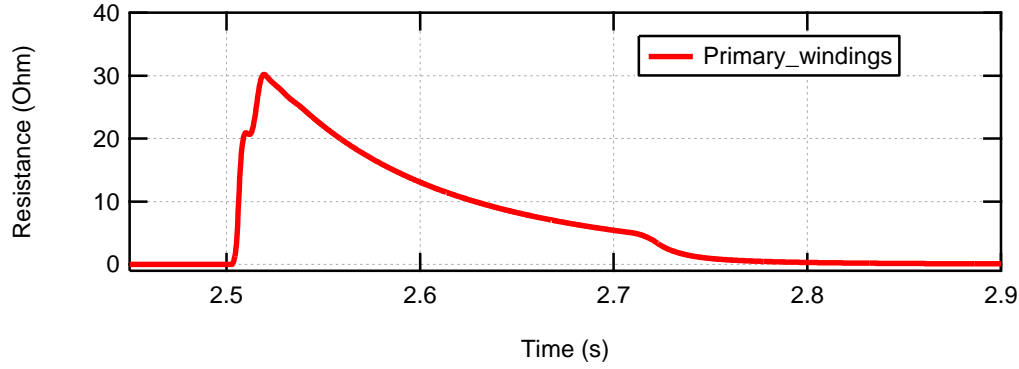


Figure 3-9 Case 1: Primary windings resistance

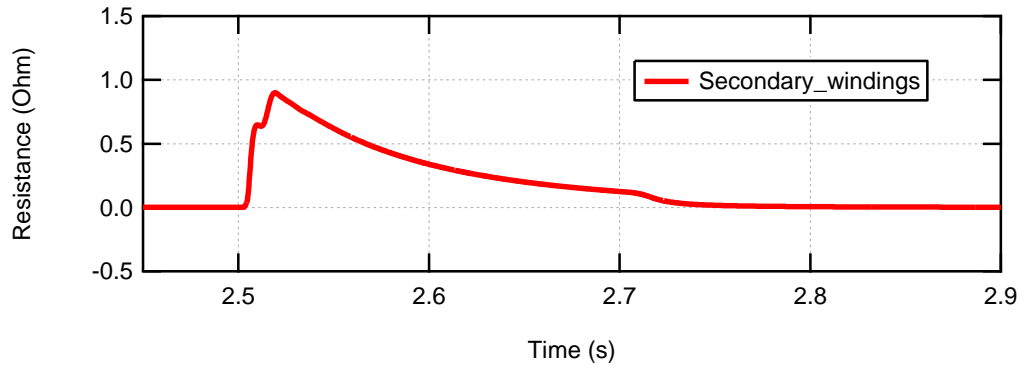


Figure 3-10 Case 1: Secondary windings resistance

3.6.2 Case 2: Five-cycle fault

By increasing the fault-current duration from roughly one cycle to five cycles (100 ms), the effect of current limitation and temperature rise in a fault of increased duration can be analysed.

Figure 3-11 and Figure 3-12, respectively, show the currents in the primary and secondary windings of the SFCLT with a stabilizer thickness of 40 μm . The SFCLT was able to effectively limit the current in both sides of the transformer until the fault clearance instant, with the same percentage reductions as in Case 1. In addition, the maximum temperature rise during this fault period is 370 K in the primary side and 390 K in the secondary side, as shown in Figure 3-13. Moreover, the results show that the transformer windings could recover from the temperature rise and resume superconductivity within a very short time. In this case, the resistance represents the normal resistance mode, where the resistance values reach more than 60 Ω on the primary and retain this value until the

recovery period starts following fault clearance, as shown in Figure 3-14. Figure 3-15 shows that the secondary windings follow the same behaviour during this longer fault period.

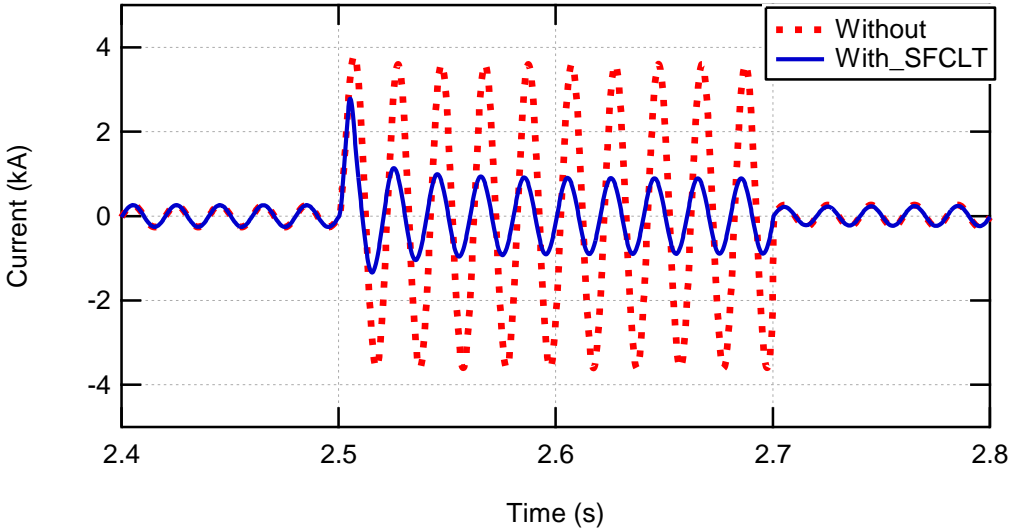


Figure 3-11 Case 2: Primary-side currents

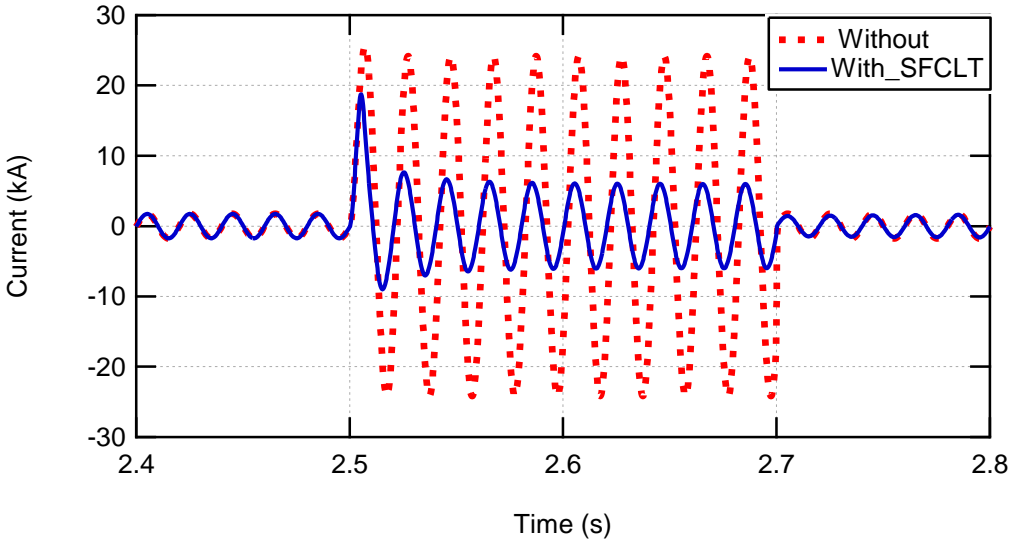


Figure 3-12 Case 2: Secondary-side currents

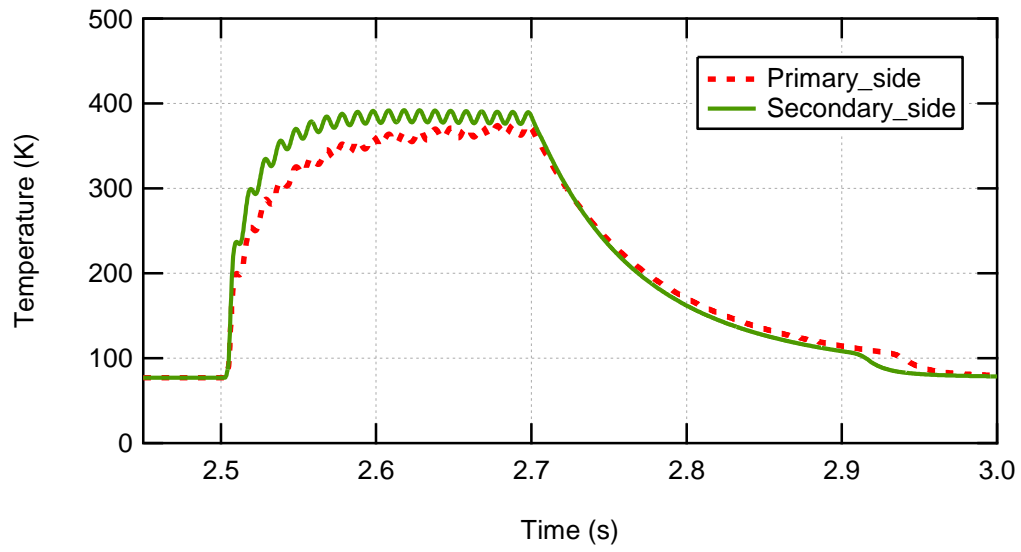


Figure 3-13 Case 2: Primary and secondary windings temperatures

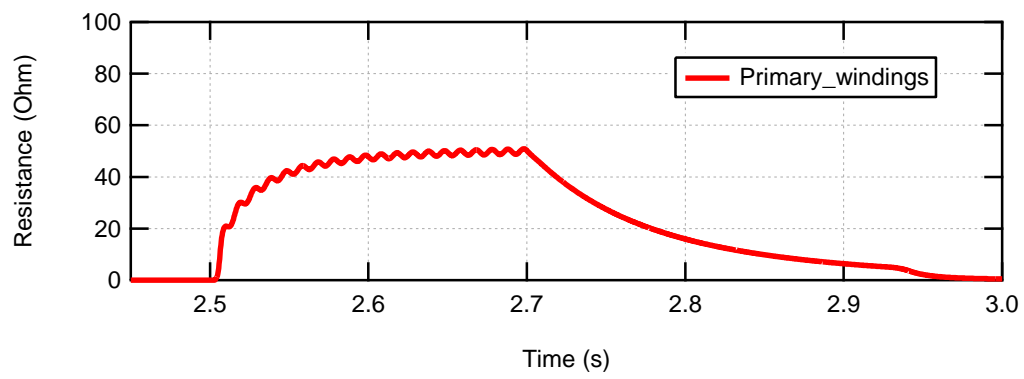


Figure 3-14 Case 2: Resistance of the primary windings

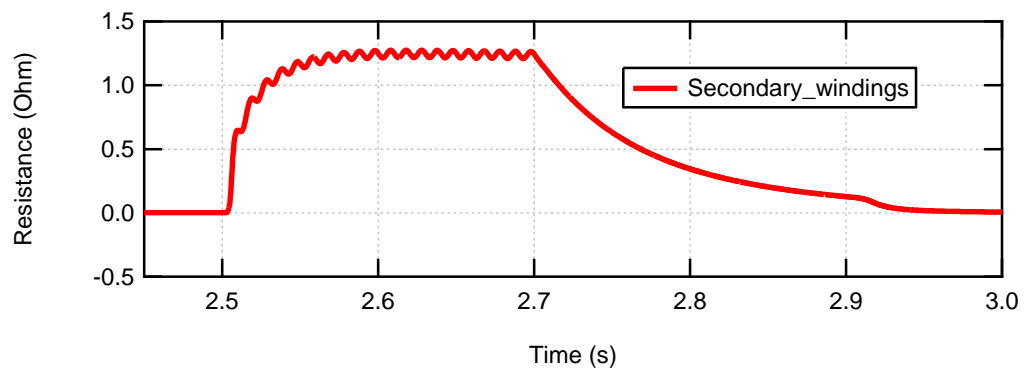


Figure 3-15 Case 2: Resistance of the secondary windings

The cases are repeated with the stabilizer thickness increased from 40 to 100 μm . The major considerations when comparing the two stabilizer thicknesses are the current limitation during the fault period and the maximum temperature rise.

Figure 3-16 summarizes the current limitation achieved when using 40 and 100 μm stabilizers with the limitation percentage calculated according to the prospective (*pro*) and actual (*SFCLT*) currents as follows:

$$\text{Current limitation} = \frac{I_{pro} - I_{SFCLT}}{I_{pro}} * 100\% \quad (3 - 14)$$

It can be seen that the limitation percentage is higher in both the primary and secondary sides when using a 40 μm stabilizer thickness. In addition, the temperature rise is smaller, indicating that the preferred stabilizer thickness is 40 μm .

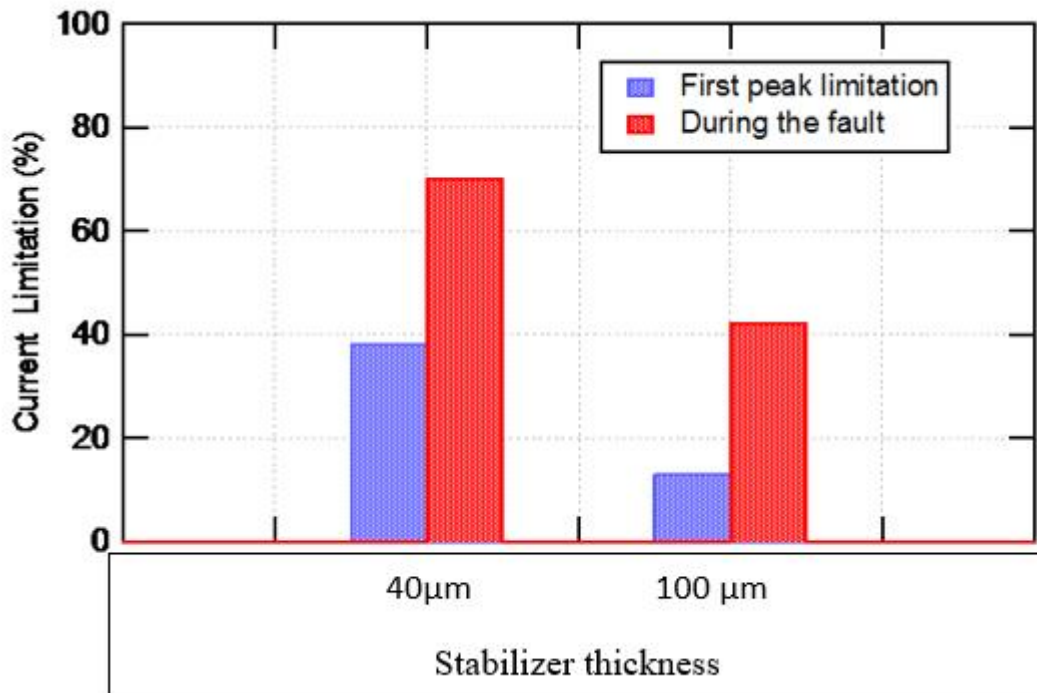


Figure 3-16 Current limitation (%) of SFCLT w.r.t. stabilizer thickness

3.7 Application of a 100 MVA SFCLT to a wind farm power grid

Following the initial investigation of the SFCLT model with a simple power system, the model is used as a replacement for a conventional 100 MVA transformer in a grid

simulation consisting of a combination of 50 kW wind farm and diesel generation, which are connected to the transmission line via the SFCLT, as shown in Figure 3-17. The design of this simulated grid is based on a real design for a power grid [101]. The system parameters and ratings are illustrated in the figure and the wind farm consists of seven induction-generator-based wind turbines. All the components are modelled using the PSCAD software. The expected function of the transformer is to protect the generation unit from high fault currents and to support system stability. Different scenarios are modelled to investigate the SFCLT and system behaviours. The focus is on the current limitation on both the primary and secondary sides of the transformer, as well as on the temperature increases during and after the fault condition. In addition, the voltage at the wind farm terminals and the active power will be focused on to determine the enhancement of the wind farm stability. The scenarios studied include three different fault locations and fault types. To clarify the effectiveness of the SFCLT on current limitation, the circuit breakers are set to trip after 200 ms. This time is chosen to allow the study of the SFCLT operation and the effect of its recovery time, in addition to considering circuit breakers' failure to trip. In all cases, the fault starts at 5 seconds and lasts for 100 ms. The results of these various simulations are discussed in the following section.

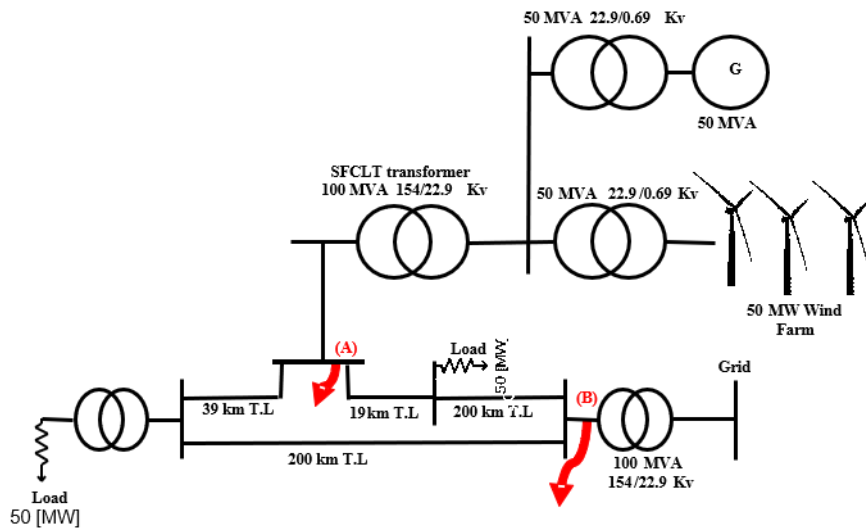


Figure 3-17 Generation integration with fault-current-limiting transformers

3.7.1 Case 1: SLG fault at location A

When a single line-to-ground fault is applied at point (A), as illustrated in the system depiction of Figure 3-17, the primary and secondary phase-*a* currents of the SFCLT windings are as shown in Figure 3-18 and Figure 3-19, respectively. Figure 3-18 shows that the use of SFCLT limits current at the first peak to ~12.7 kA from a prospective current of ~15.1 kA, that is, 85% of the prospective value. Moreover, after the first peak, the percentage limitation increases and the current only reaches 54% of the prospective value during the remainder of the fault period. As shown in Figure 3-19, the secondary-side current is also reduced significantly, reaching about 1 kA during the fault period compared with a prospective value of 2 kA, while the SFCLT limits the first peak to 86% of the prospective value. Figure 3-20 illustrates the temperature rise in both the secondary and primary windings when the SLG fault is applied at location (A). The temperature reaches a maximum value of 420 K on the primary side, while on the secondary side it reaches 350 K. These values can be manipulated with different cooling methods and designs. The temperature took about 3.5 seconds to resume its pre-fault value, meaning that the windings recovery period is 3.5 seconds. However, this recovery period has a minor effect on the transformer currents, as can be seen in Figures 3-18 and 3-19.

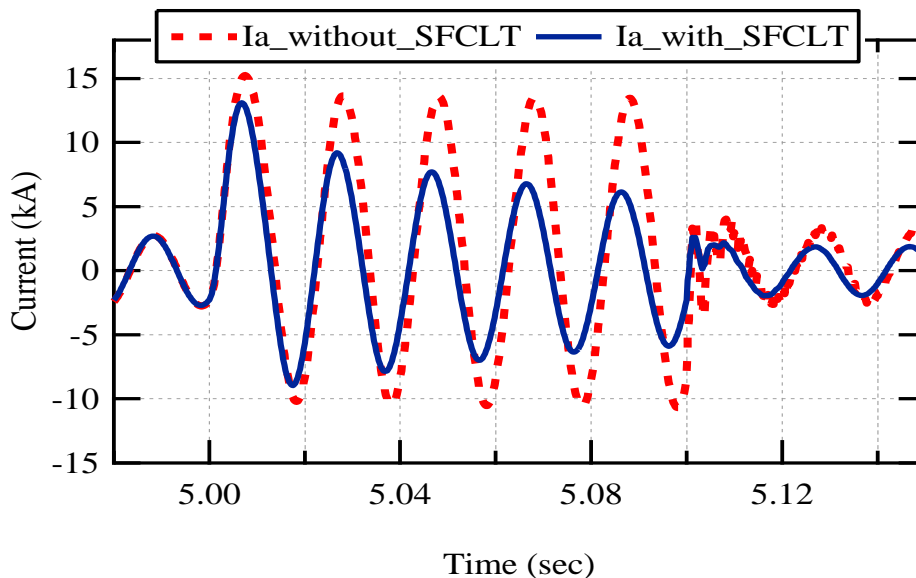


Figure 3-18 Case 1: Primary-side currents with and without the limitation effect of the SFCLT

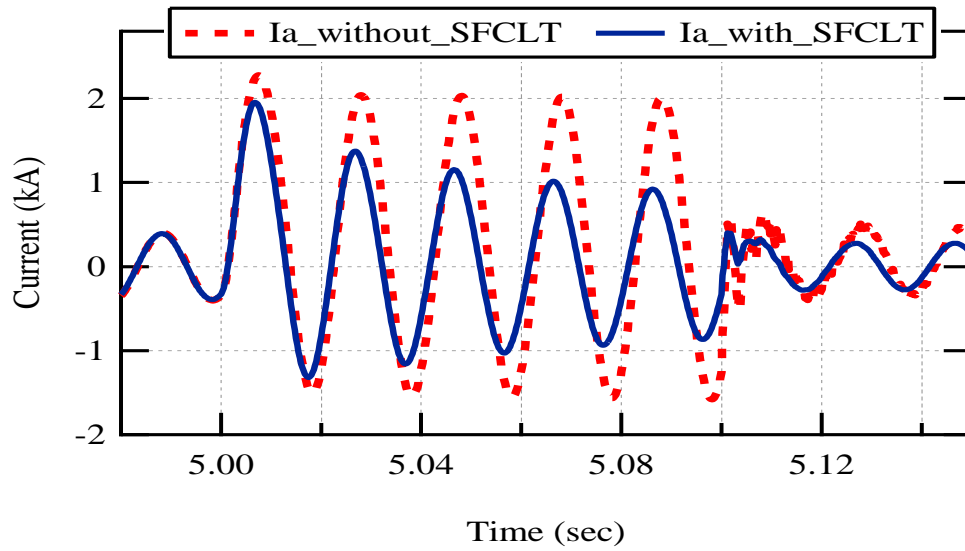


Figure 3-19 Case 1: Secondary-side currents with and without the limitation effect of the SFCLT

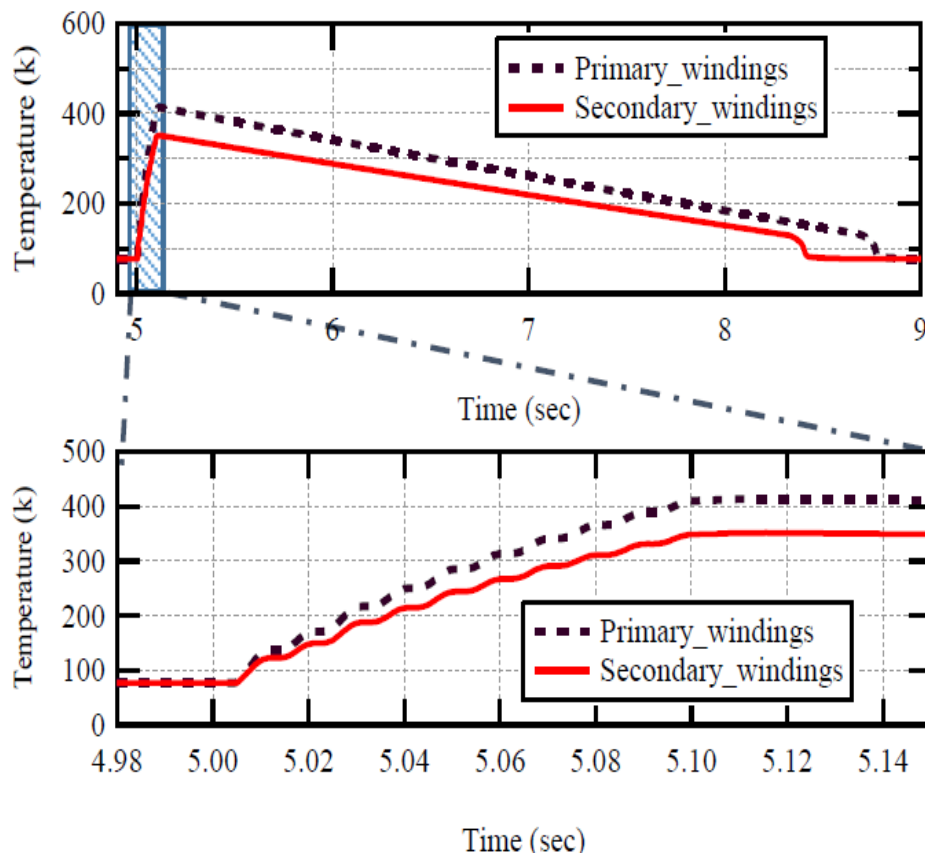


Figure 3-20 Case 1: Temperature of the primary and secondary windings of the SFCLT (the lower figure represents a detailed inset of the upper figure)

3.7.2 Case 2: SLG fault at location C

To further test the effectiveness of the SFCLT to limit fault currents, a SLG fault is applied at a location remote from the transformer, that is, location (C) at the grid terminals, as illustrated in the system depiction of Figure 3-17. Because the fault is further away from the generator, the contribution of the generation unit to the fault current is slightly lower than that for location (A). Figure 3-21 shows the limitation in the primary current during the fault period. The pre-fault value was ~ 10 kA and is reduced to an average of 7.5 kA by use of the SFCLT. The maximum temperature rise for the primary windings was about 280 K in this case, as shown in Figure 3-21.

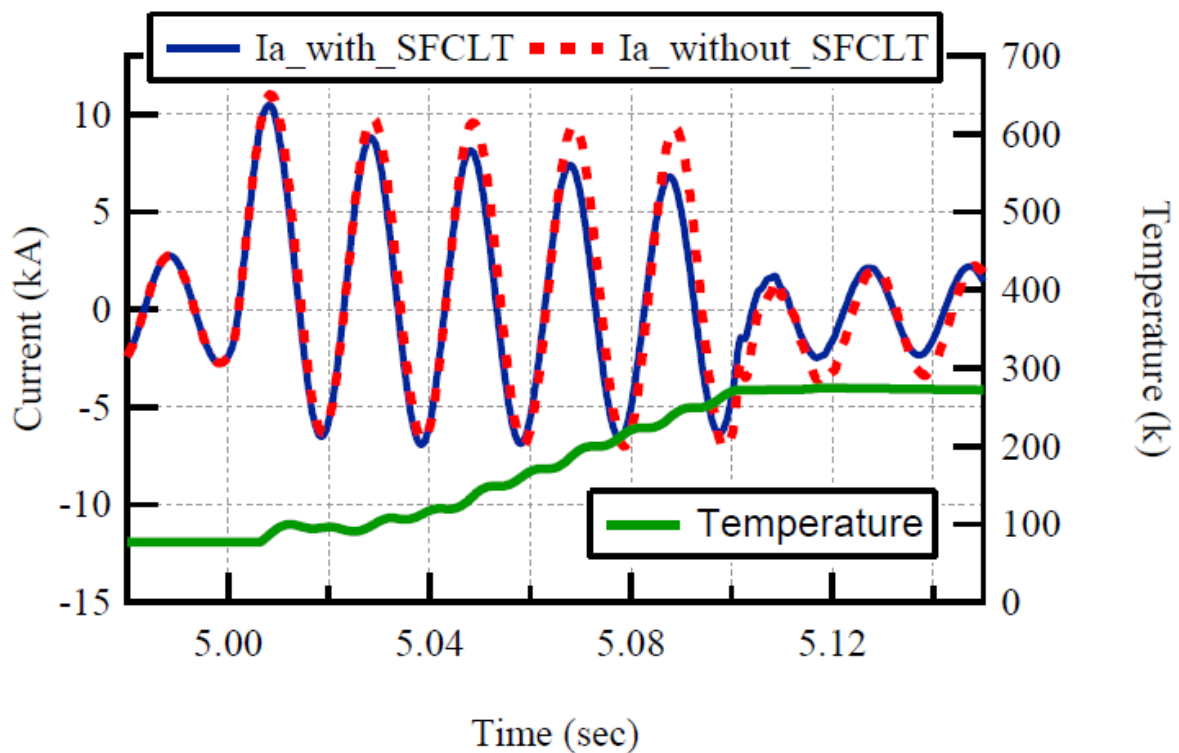


Figure 3-21 Case 2: Primary-side currents with and without the limitation effect of the SFCLT, and temperature of SFCLT primary

3.7.3 Case 3: 3PhG fault at location A

The second scenario involves application of a three-phase-to-ground (3PhG) fault at location (A). In this case, the limitation effect is studied on the three phases of the transformer. Figure 3-23 shows the primary-side currents without the use of an SFCLT, while Figure 3-23 shows the currents with an SFCLT. During the fault period, the current

limitation was ~46%, with a noticeable enhancement in the current transient period just after the fault clearance with the SFCLT. The effect of adding the SFCLT is also studied on the secondary windings, as shown in Figure 3-24 and 3-25. The SFCLT also limits the currents during the fault from a prospective value of 2 kA to less than 1 kA, and limits the first peak of phase *a* to 2 kA. The temperature increases in the primary and secondary windings in phase *a* during the fault are shown in Figure 3-26: the maximum temperature rise in the secondary is 330 K, while that in the primary is 400 K.

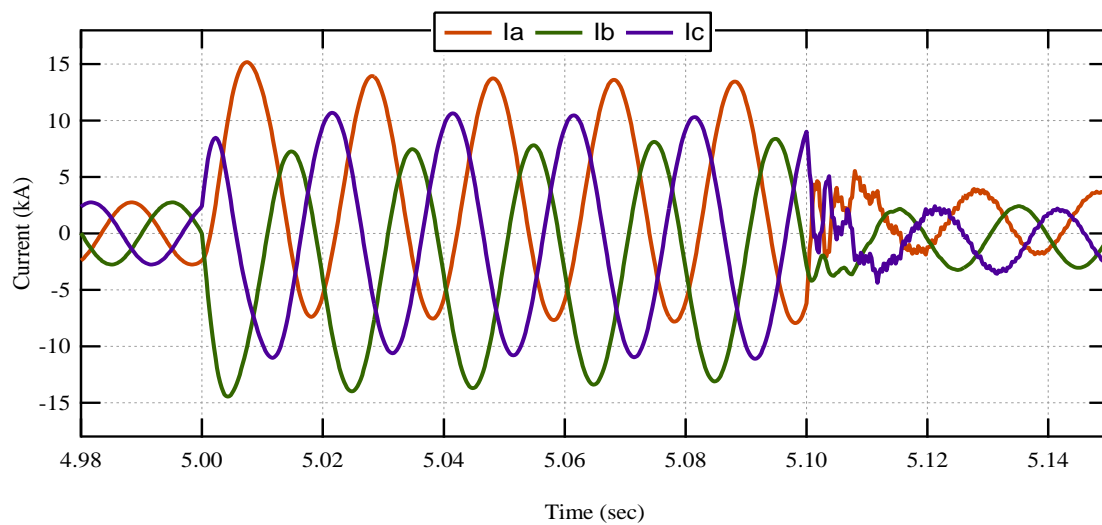


Figure 3-22 Case 3: Primary-side currents without SFCLT

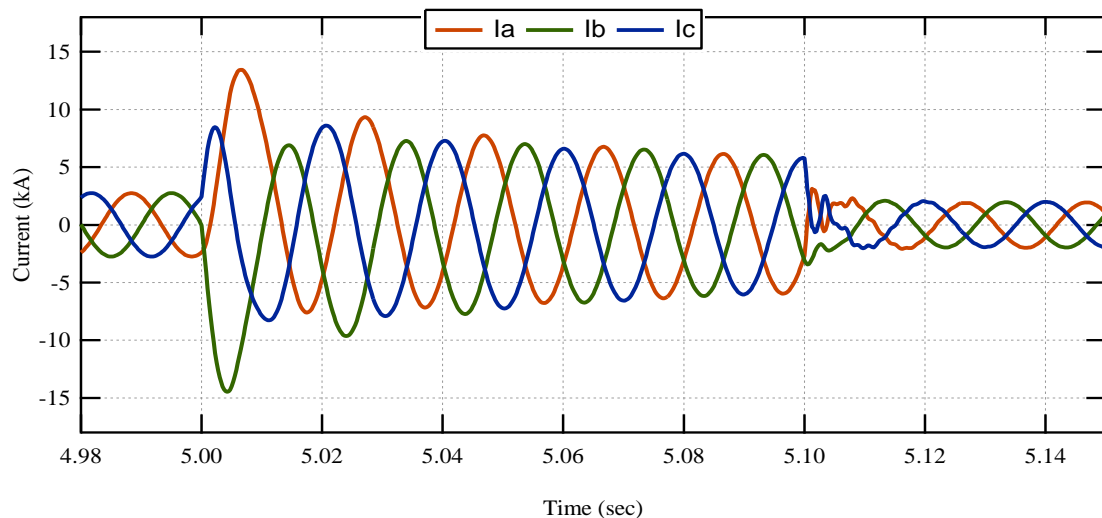


Figure 3-23 Case 3: Primary-side currents with SFCLT

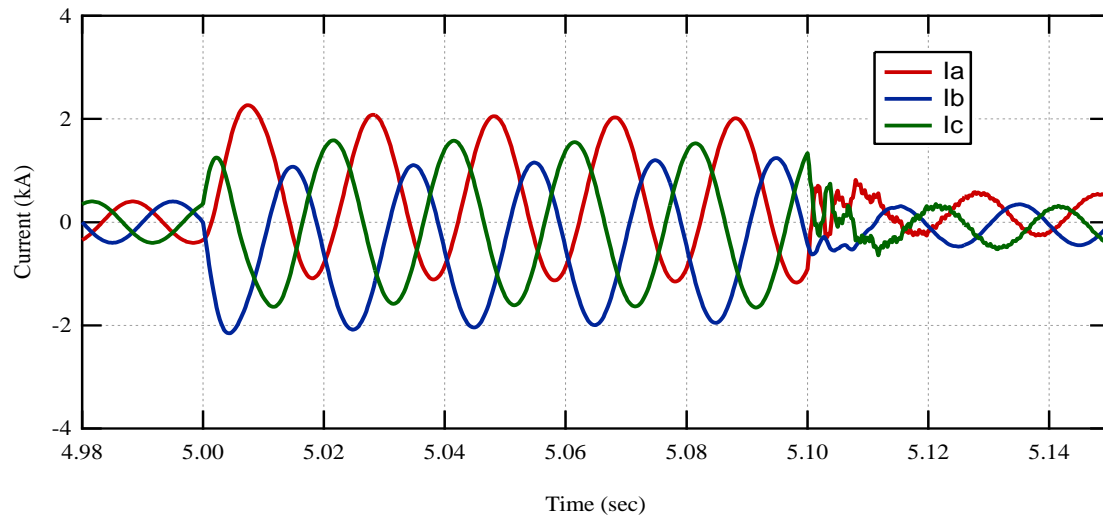


Figure 3-24 Case 3: Secondary-side currents without SFCLT

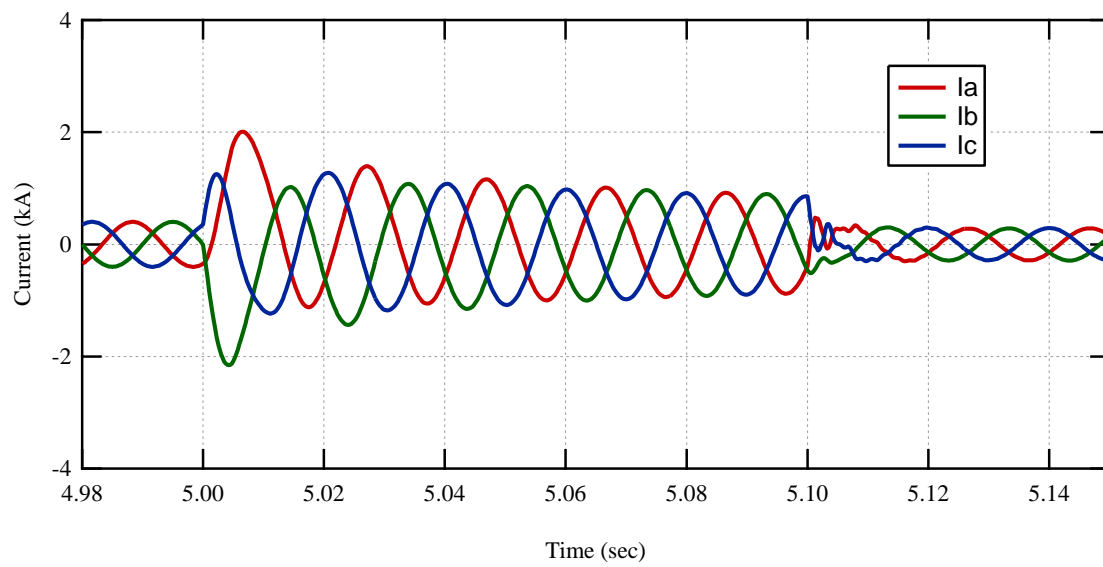


Figure 3-25 Case 3: Secondary-side currents with SFCLT

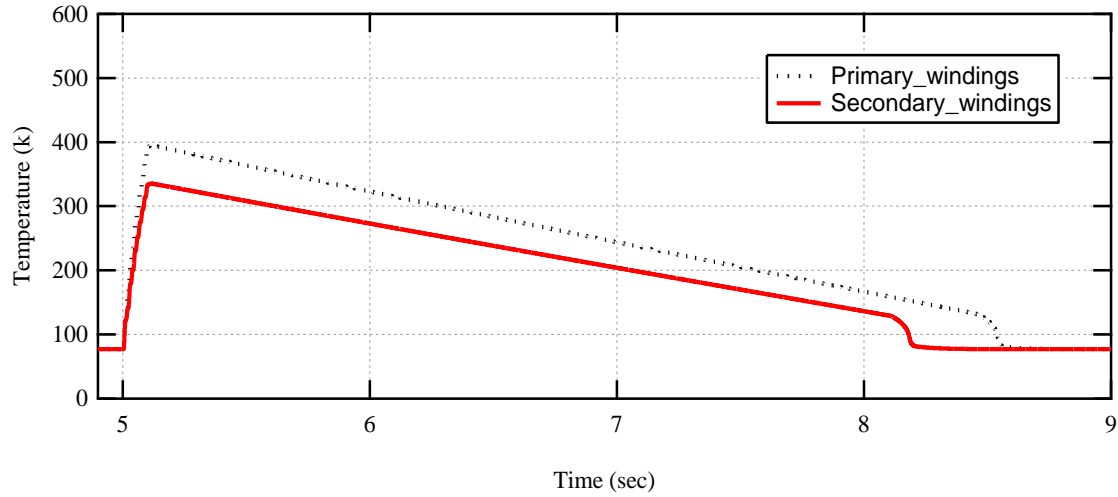


Figure 3-26 Case 3: Primary and secondary windings temperatures

3.8 Summary

This chapter documented the modelling and design of a superconducting fault-current-limiting transformer, based on the behaviour of the superconducting materials. The parameters of the model can be changed to fit with any other SFCLT design, and the model can be integrated with different power system configurations. The SFCLT proved effective in limiting fault currents in a simple power system. It also provided effective limitation of fault currents in different scenarios within a wind farm power system, which helps to protect the wind turbine generators and might represent a solution to integrating new wind farms into existing power grids without the need to upgrade the protection system to cope with increased short-circuit levels.

Chapter 4

SMES-FCL in AC power systems

Superconducting magnetic energy storage (SMES) consists of a coil made from a superconducting material and has the ability to store electrical energy in the magnetic field of the direct current. The superconducting magnetic material enables the SMES magnet to generate a strong magnetic field with negligible losses. SMES has been studied for use in energy storage applications since the 1970s [102]. Unlike inductors of copper and other materials, superconducting materials have a near-zero resistance that allows currents to circulate in a resistance-free path. The major disadvantage of SMES compared to other energy storage devices is its high cost. To mitigate this problem, this chapter proposes a new scheme in which SMES serves as a multifunctional device rather than just an energy storage device. The resulting SMES-FCL system is designed to provide energy storage as well as limiting fault currents to enhance the stability and fault ride-through capability of an AC power system containing a wind turbine generator.

4.1 Introduction

SMES can exchange its stored power with the grid via power conditioning systems for small periods of time. SMES has an unlimited number of charging and discharging cycles with a very high efficiency, as high as 95% [103]. In addition to power smoothing, SMES can perform several other functions in the power system. For example, it can be used to achieve load levelling, dynamic voltage improvement, black-start capability, transmission capability enhancement, and provision of a spinning reserve.

An SMES system consists of a large coil made from a superconducting material that can absorb or release energy. It can store the electrical energy in its own magnetic field, generated by the DC current flowing through it. When connected to AC grids, an SMES always needs an AC/DC converter or a power-conditioning system. To retain its

superconductivity state, the superconducting coil must be maintained at a very low temperature by a cryostat, which might contain liquid helium or liquid nitrogen.

Because the power-conditioning system (PCS) is the part that handles the power transfer between the AC system and the SMES, the SMES circuits can be divided into three types on the basis of the PCS [104]. These three types are the thyristor-based PCS, the current-source converter (CSC)-based PCS, and the voltage-source converter (VSC)-based PCS. Figure 4-1 presents circuit diagrams of the three types. The thyristor-based configuration has the advantage of simple construction because it has only the AC-to-DC converter element. The charging or discharging process can be controlled by varying the delay angle of the thyristors. However, it can largely only control the active power, and has little control over the reactive power. The VSC-based SMES consists of six switches, which may be insulated-gate bipolar transistors (IGBTs) or metal-oxide-semiconductor field-effect transistors (MOSFETs), controlled by a pulse-width modulation (PWM) controller and a DC-to-DC converter ('DC chopper'). The VSC is responsible for controlling the active and reactive power of the system while the DC chopper maintains the DC voltage constant. The two converters are linked by a DC-link capacitor. The reactive and active power can be controlled independently in a VSC-based SMES, and also in a CSC-based one. The CSC-based SMES needs a capacitor bank to act as a filter for the high-order harmonics of the AC-line currents. To summarize, thyristor-based SMES is used when only active power control is needed but has higher levels of total harmonic distortion (THD) and high ripples in the coil voltage; VSC- and CSC-based SMES can control the active and reactive power independently, and also benefit from lower THD. Thus, the most appropriate SMES topology can be determined according to the intended application. . More details about the control schemes of each part can be found on [104]. In terms of the rest of this chapter, section II describes the design aspects of SMES system components and includes a cost-effectiveness discussion of these different parts of the system. Section III presents a brief discussion of SMES usage in an AC power system, and section IV reviews the literature of previous research into SMES systems used to limit fault currents as well. The proposed SMES system is described in section V, and its operational principles are discussed, including control of the voltage-source converter, the DC chopper, and the incorporation of the fault-current-limitation function. A brief description of the system parameters is in section VI before the system is investigated as an energy storage device in section VII, testing its ability to smooth the power output of

a wind turbine generator and compensate for the voltage drop at the generator terminals. The ability of the SMES system to limit fault currents and enhance system stability is investigated in section VIII by testing four different fault scenarios. Finally, section IX summarizes the chapter.

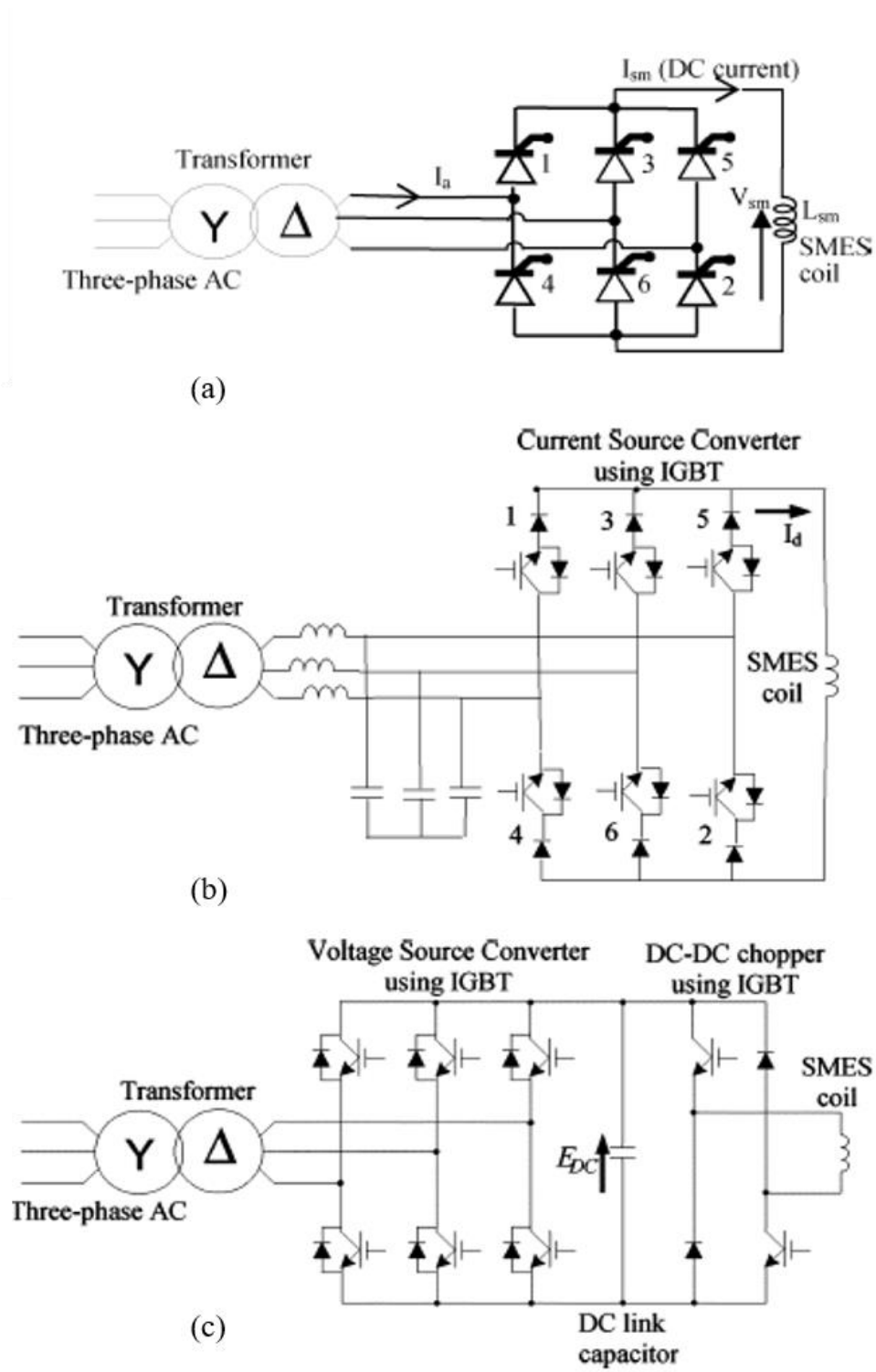


Figure 4-1 Different power-conditioning systems for SMES in AC systems: (a) thyristor-based PCS; (b) CSC-based PCS; (c) VSC-based PCS [104]

4.2 Design aspects and cost-effectiveness of SMES systems

In designing a superconducting magnet, cost will be a major factor alongside the total efficiency. Such magnets become efficient when the total lifetime cost of the device is lower than that of other types of magnet such as resistive or permanent ones. However, it may also be necessary to use superconducting magnets when they are the only device that can perform the required task.

In the early 1990s, low-temperature superconducting materials were used in the design of SMESs. However, the cost of the refrigeration system needed to keep the coil at such low temperatures increased the total cost of the SMES systems [105] [106]. With the rapid developments in high-temperature superconducting materials, many studies started to develop SMES coils from these HTS materials because their refrigeration requirements are much less demanding than those of an LTS. However, in this case, the high cost of the HTS material itself comes to dominate the cost of the SMES [107] [108]. According to [104], the cost of the storage element in an SMES system can range from \$85K to \$125K per MJ, and the cost of the power-conversion system could be between \$150 and \$250 per kW. Although these numbers are comparatively old, their wide range reflects the fact that the cost of an SMES system can be subject to many parameters.

The total lifetime cost of a device consists of its capital or equipment cost plus its operating costs [109]. The capital cost of an SMES includes the cost of all of the components of the system, which can be listed as:

- The superconducting coil
- The refrigeration system
- The power-conditioning system
- The assembly costs
- The (cryogenic storage) dewar
- The current leads.

The operating costs largely derive from the maintenance costs and the power consumption of the system. Most studies into the cost of superconducting magnets assume that the cost depends mainly on the energy stored. Figure 4-2 illustrates the cost of three different types of SMES magnets, excluding the refrigeration costs, based on the 2007 US dollar [110]. In these results, the cost proves roughly proportional to the energy stored and the

superconducting material forms about 20 per cent of the total cost. An investigation of approximate SMES component costs has been conducted elsewhere [111], and Table 4-1 summarizes the results.

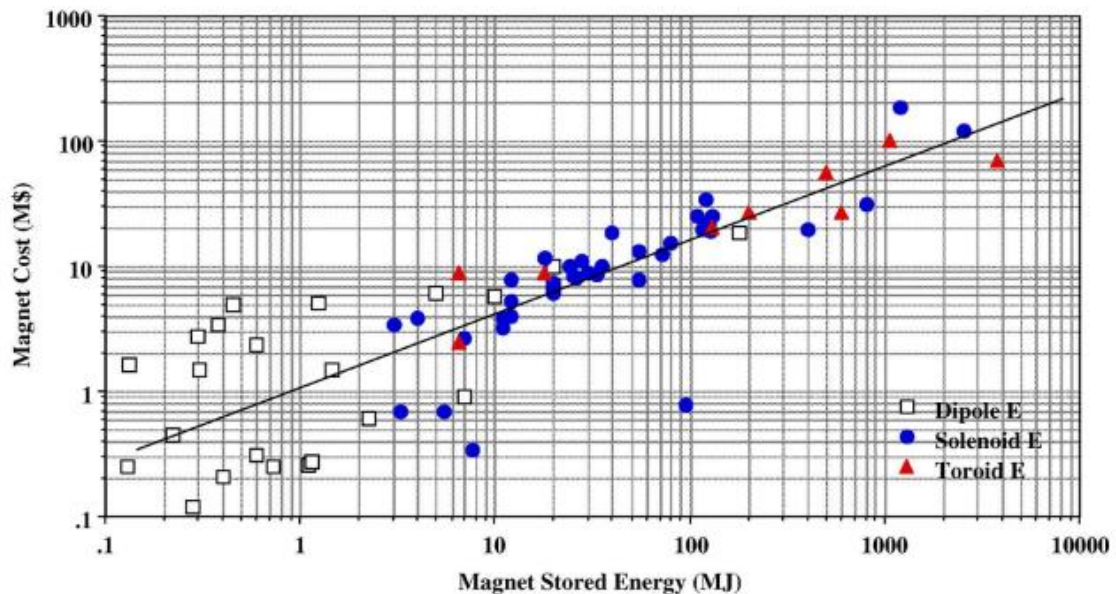


Figure 4-2 Total superconducting costs (\$M) versus stored energy (MJ) [110]

Table 4-1 Estimated SMES component cost proportions [111]

Cost component	Proportion (%)	Type of cost
Superconducting coil	21–25	Capital
Refrigeration system	5–10	Running
Power conditioning	15–30	Running
Operating costs	13–15	Running
Device assembly	8–12	Capital
Other	3–18	Capital

There follows a brief discussion of the principal parts to give an idea of how we might estimate the cost of a SMES system.

4.2.1 The superconducting magnet

The cost of the superconducting magnet changes with each tape type, and depends on the types of raw materials and production methods. Furthermore, the dimensions of the

magnet, especially its length, are considered to be the main factor affecting the cost of the magnet. The tape length, in turn, depends on the energy storage requirement and the design method of the coil. As an example, the cost of BSCCO conductors in the form of tape is 52 \$/kA.m at temperature $T = 30$ K and perpendicular $B = 2T$. Under the same conditions, the price of a REBCO tape is 140 \$/kA.m [112]. Although the latter is more expensive, it appears to be a better conductor because it endures greater stress before degrading. If more copper is needed for quench protection at energies above 50 kJ, the cost of both conductors will be higher. Although the price of HTS materials is still high, prices are showing an annual decline of about 10 per cent [109], which will increase the opportunities for the commercialization of SMES systems in the near future.

The most common configurations for an SC magnet are toroidal, single-solenoid and multiple-solenoid magnets. Figure 4-3 illustrates the configurations of these three magnet types [113].

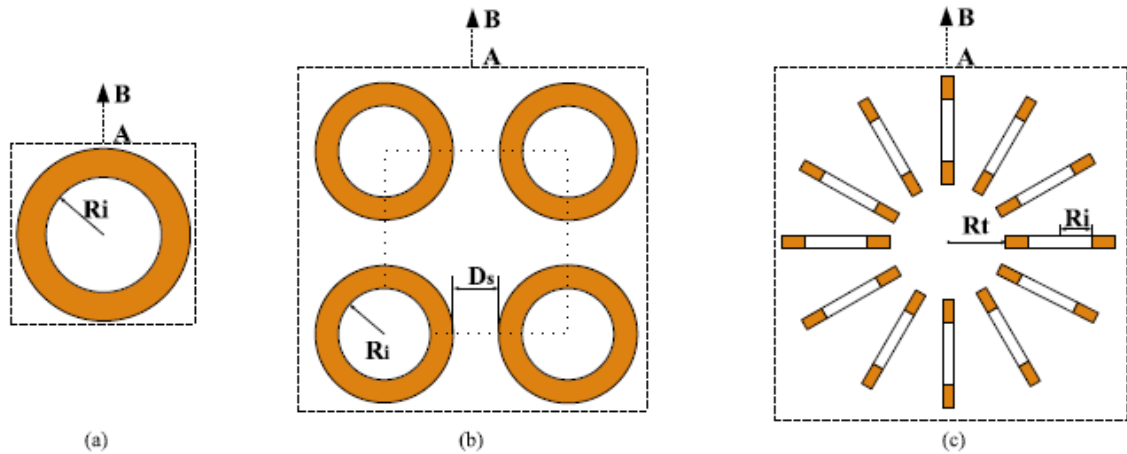


Figure 4-3 Three common types of SC magnet: (a) single-solenoid; (b) four-solenoid; (c) toroidal [113]

The mechanical and electromagnetic characteristics are different for each of these configurations. The simplest configuration is the single-solenoid one, which is why it is widely used in designing SMES magnets [114] [115]. With medium energy storage requirements (above 1 MJ), the toroidal magnet is preferred because the wire cost in this case is less than that of the solenoid type. In addition, the field leakage is lower in the toroidal configuration, which is also comparatively compact when it comes to high energy

requirements. However, in this case, the radial stress is high, which requires special arrangements to increase the magnet's mechanical strength. The multiple-solenoid configuration has the lowest radial stress, which makes the risk of mechanical damage lower for the same scenario. The single-solenoid configuration has intermediate wire cost and stress but it has greater magnetic field leakage, which may cause electromagnetic interference with other electronic devices around it.

4.2.2 The refrigeration system

The refrigeration system is a very important part of SMES system design. It is the component that is responsible for keeping the coil at a very low temperature such that it retains its superconductive state. The cost of this system appears to be proportional to the capacity of the refrigerator. The required refrigeration capacity is directly related to the cooling load for the SMES magnet. The rated power of the SMES system, the operating conditions, and the surrounding environmental parameters can all be used to determine the required cooling load [110]. To keep the coil at a low temperature the refrigeration system must be designed such that the time required for cooling is shorter than the time taken for the temperature to rise. Some researchers have proposed equations to calculate the refrigeration costs on the basis of the energy stored [110], but these equations are only applicable to LTS magnets. An estimation for the refrigeration costs based on temperature is shown in Table 4-2 [107]. It is clear from the table that the cost of the refrigeration system decreases by a significant amount with each increase in target temperature.

Table 4-2 Cost and characteristics of the refrigeration system [107]

Temperature (K)	Cost per cooling capacity
	(\$/Wt)
10	290
20	160
30	110
40	90
50	60

4.2.3 Power-conditioning system

The power-conditioning costs depend on the rated power of the SMES system as well as its configuration. This includes the converters, controllers and the monitoring system. Connecting the SMES to an AC system requires two stages of power conversion, an AC-DC converter and a DC-DC converter. Connecting the SMES only to a DC system requires only the DC-DC conversion stage, which will decrease the power-conditioning cost. Incorporating an SMES into control systems of the main systems without the need to install PCs to the SMES itself as might be the case in FACTs or renewable energy sources, may lower the total cost of the SMES system by eliminating the cost of the PCS. In essence, the cost of the PCS is proportional to the rated capacity of the SMES.

4.2.4 Operating costs

Operating costs (running costs) are the type of costs that last the lifetime of a device. For the SMES system, the first operating cost is power consumption. Although the coil itself might have zero losses, there are many other potential sources of power consumption in the system. The refrigeration system, losses on the power-conditioning system switches, and connections to the power system are the main causes of power loss. All of them depend on the power rating of the system. There is also a maintenance cost, although this represents a very small proportion of the total SMES system cost.

4.3 Applications of SMES in electrical power systems

Because superconducting coils prove to have a quick response time, they can store energy and return it to the system within a few milliseconds, making them perfect for storing energy from renewable energy sources such as wind turbines or photovoltaic systems. This can be used to smooth the output power of intermittent natural (renewable) sources.

Another very important usage of SMES is in compensating for voltage drops and supporting sensitive loads should a sudden drop occur in the generation side [73]. SMES units can be used in place of spinning reserve generators. With their fast response time and high energy capacity, they offer a competitive alternative to spinning reserve units.

Pulsed loads may lead to an increase in the rated capacity of a generator. Such highly rated generators may be problematic when size and weight are very important parameters,

as in electric ships or electric aircraft. A SMES unit could be used to help in supplying power to the pulsed load instead of increasing the generator ratings, in addition to supporting the load in the case of voltage drop [74].

4.4 Literature review of SMES-FCL in power systems

Some studies have been conducted on the coordination between a SMES system and an SFCL. Other studies have incorporated the current-limitation function into the SMES system, using a variety of methods. Thus, one study established coordination between a flux-coupling-type SFCL and a SMES in an AC microgrid system [116]. Although this coordination resulted in a smoother transition between connected and island modes and during disturbances, the flux-coupling SFCL is bulky (as previously described) and the control system becomes more complex. Another study used a SMES system on the DC-link side of a permanent-magnet synchronous generator and a resistive-type SFCL on the AC side [117]. This eliminated the AC-to-DC conversion step but used an SFCL in the AC side, which requires three SFCLs, one for each phase. In addition, the enhancement in the grid-side converter current limitation was not sufficient to justify the added cost and materials.

A number of studies employed a single SMES coil and modified the control action to use it as an FCL as well. Thus, one study connected the SMES to an AC circuit and inserted the whole SMES coil into the system during the fault period to limit the fault [118]. Another study used a different method in which the system is connected to an AC line [119]. The whole coil is also used to limit the fault currents and two transformers are used to connect the SMES system to the main system. Elsewhere, the same researcher connected the SMES in the DC side of a doubly-fed induction-generator controller [120]. The whole coil is inserted to the DC line during the fault condition, which may affect the coil and waste the energy stored in it. Similar research connected the SMES coil and its DC controller in the DC-link side of a DFIG converter [121]. The enhancement in the rotor and stator currents were small with this topology.

As is evident from this brief literature review, coordination between the SMES operation and the SFCL operation gives good results in limiting fault currents and reducing the size of the SMES coil. However, there are still cost and space issues when using two superconducting devices, especially with the three-phase system where there is a need for

three SFCLs, one for each phase. The alternative approach of using the whole SMES coil in both current limitation and energy storage saves the space and cost of using two superconducting devices. However, inserting the whole coil into a system during a fault may lead to destruction of the coil and may increase the inductance of the system during the fault period, which could have a negative impact on system stability.

On the basis of this literature review, the disadvantages highlighted by prior research are avoided, and a new technique is used in which only part of the coil is inserted into the system during fault periods using a three-windings transformer, as will be discussed in detail in the next section.

4.5 Principle of SMES-FCL operation

A wind-generation-based power system is used to investigate SMES-FCL operation. SMES plays a role in smoothing the output power from the generator. In addition, limiting fault currents is very important, especially with wind turbine generators, to protect the generators and improve their fault ride-through capability [84]. The system consists of a single induction-generator-based wind turbine connected to a resistive load, and is made simple to allow a focus on the performance of the SMES-FCL and the control actions. . The control system and configuration may be changed with different wind turbine generator types. Figure 4-4 shows the connection of the SMES-FCL to the main system. It is connected in series with the system using a three-phase three-windings transformer. The first windings are connected in series with the power line, while the second windings are connected to a voltage-source converter. The third windings are responsible for the current-limitation function and are connected to the part of the SMES coil that is used in current limitation, as will be discussed later.

The operational principle depends on using the same superconducting coil to both store energy and limit fault currents. The whole coil is used to charge, discharge and store energy, while only a part of the coil is inserted into the main system during fault periods to increase the total impedance of the system and thereby reduce high fault currents. The switches S1 and S2 illustrated in Figure 4-4 are the main controllers that switch the system from normal mode to fault mode. The following section describes in detail the control of the VSC and the control of the fault-current-limitation element.

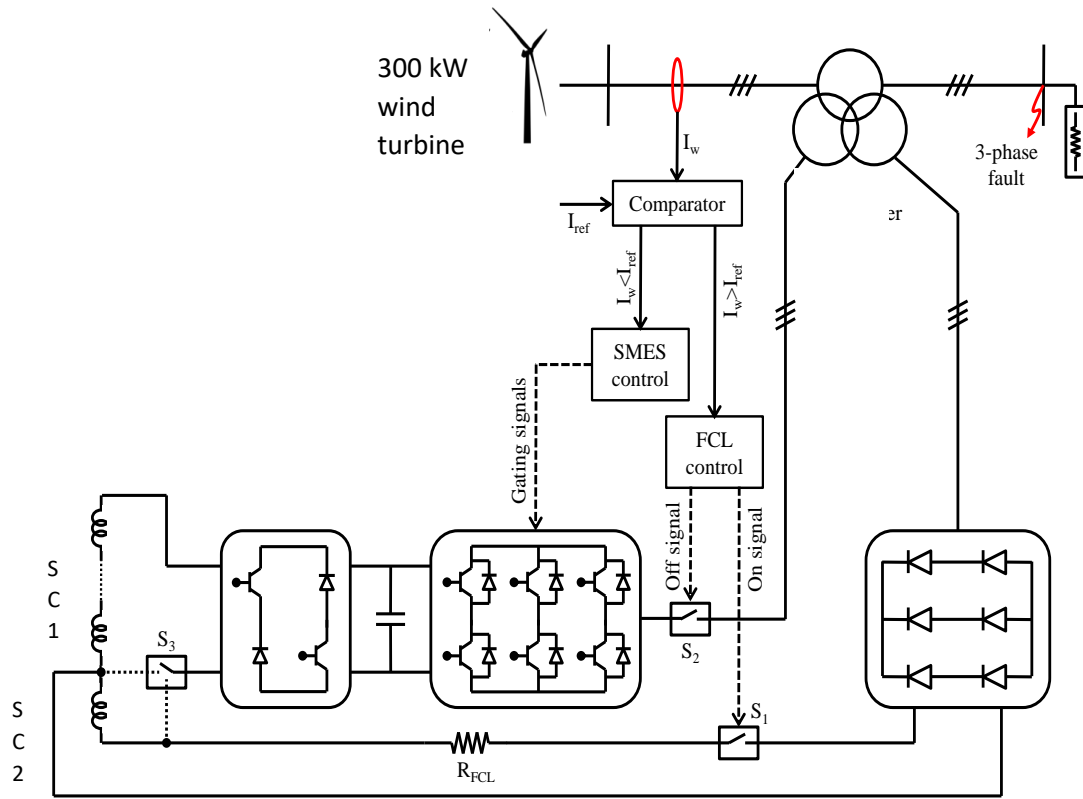


Figure 4-4 SMES-FCL system configuration

4.5.1 VSC control

The main function of the VSC is to keep the voltage and frequency constant at the connection point with the main power system [122]. It is used only on the energy storage mode to charge or discharge power from the main system. It is disconnected from the main system in case of fault detection and activation of fault current limiter mode. Direct vector control is used in the control of the VSC. The AC values of the voltages and currents at the connection point are measured and transferred to the $d-q$ reference frames [80]. To hold the phase value (θ) at each instant, a phase-locked loop technique (PLL) is used that allows the resumption of the phase value while injecting voltages into the system. The reference values for the currents are then calculated on the $d-q$ frame. After that, the corresponding voltage references in the $d-q$ frames are calculated. Finally, the injected or absorbed voltages are calculated according to the difference between the measured and calculated reference values, as illustrated in Figure 4-5.

The proportional–integral (PI) controller parameters were chosen on the basis of a trial and error method. The upper-arm parameters were set as: proportional gain (P) = 2 and integral gain (I) = 0.5, while the lower-arm parameters were P = 1.5 and I = 0.5. Finally, the VSC pulses are generated using a space-vector pulse-width modulation (SVPWM) technique.

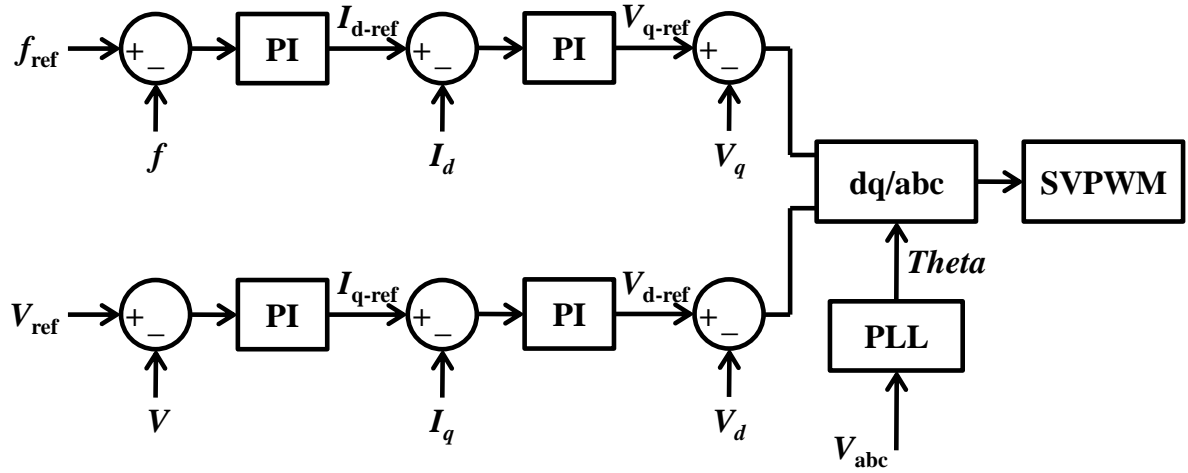


Figure 4-5 Control sequence of the VSC

4.5.2 DC-chopper control

On the other side, the main objective of the DC chopper is to keep the DC-link voltage constant. The control system of the DC chopper allows the SC coil to charge or discharge its current to or from the capacitor to achieve a constant voltage across it. The DC-chopper circuit has two IGBTs and two diodes. The operation modes of the SC coil are determined by the power rating of the main system and the DC-link voltage value. If the power at the connection point with the main system is higher than the reference value set by the operator, the SC will charge by turning the two IGBTs on or off. If the power is less than the reference value, the SC will discharge through the two diodes. If there is no power difference, the coil current is circulated on one IGBT and one diode in order to maintain coil energy without transferring power from/to the main system. The pulse generation technique used for both IGBTs of the DC chopper is illustrated in Figure 4-6. The DC-link capacitor voltage is referred herein as (V_{dc}), while its reference value is (V_{ref_dc}). D1

is the duty cycle, which determines the periods in which the IGBTs are set to be on or off. The PI parameters for the chopper controller are $P = 5$ and $I = 0.25$.

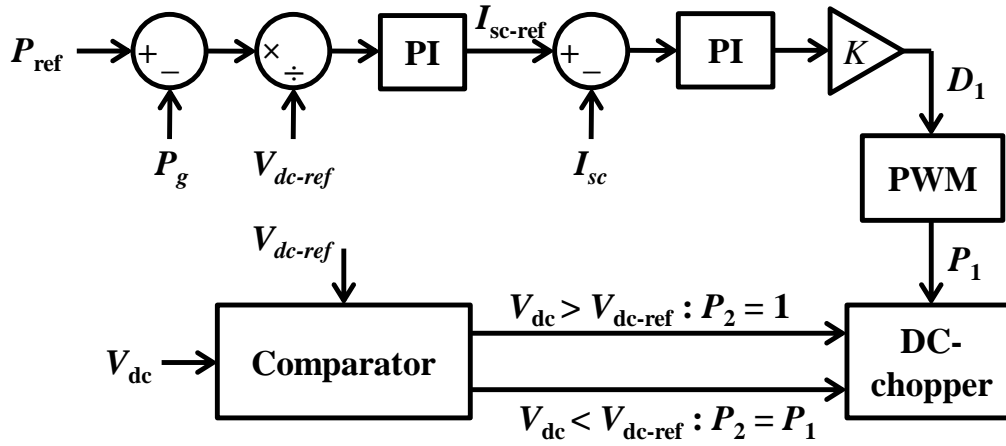


Figure 4-6 Control scheme of the DC chopper

4.5.3 Fault-current-limitation control

The fault-current-limiting element is connected to the system via the third windings of the transformer, as shown in Figure 4-4. During this mode, the VSC is disconnected from the main system and there is no charging or discharging actions between the SMES coil and the main system. The transformer windings are connected to the SC coil with a normal bridge, which consists of six diodes. The main idea in limiting the fault current is to use the resistance provided by a few coil sets (pancakes) of the SC coil after their quenching. The number of pancakes used for fault-current limitation depends on the resistance required by the system during the fault. Using a few pancakes enables limitation of the fault current by reducing the inductance inserted during the period. During the fault, the remaining pancakes of the SC coil will be isolated and switched into freewheeling mode (through switch S3) in order to maintain their stored energy and protect them from quenching.

The limiting resistance of the SC coil during quenching is represented by a constant resistance connected in series with the diode bridge through a current-controlled switch (S1) that is triggered according to the current in the main power system. The other pancakes within the whole energy storage system are isolated during the fault by turning off another current-controlled switch (S2), as shown in Figure 4-4. After fault clearance,

when the current decreases below its critical value once more, switch S1 is re-opened and switch S2 is closed again to re-establish the energy storage function.

4.6 SMES-FCL system parameters

The system consists of a single wind turbine generator of a normal induction-generator type connected with a capacitor bank to supply it with the reactive power needed for operation. The rating of the generator is 0.3 MW, with a rated voltage of 0.55 kV. The connection of the SMES-FCL is done via a three-windings transformer with 0.1 MW rated power. The load is represented by a resistance of 1 Ω . The SC coil inductance is 1 H and the operating current is 400 A, which corresponds to 80 KJ of energy storage. The coil critical current is 1 kA. The part of the coil that will be inserted as a fault-current limiter has an inductance of 0.015 H and a resistance of 0.5 Ω after quenching. The DC-link capacitor is 7 mF.

4.7 Investigation of the SMES-FCL as an energy storage device

As stated above, the main function of the SMES-FCL is to store energy and return it to the main system when needed. This investigation is done to make sure the proposed system can store energy like normal SMES systems and that adding the current limiting function did not affect the energy storage function. Given the variable nature of wind turbine generator output, a storage device is required to continuously charge and discharge according to the value of the output power, which depends on the wind speed. Based on the reference power required by the load, the SMES-FCL absorbs or injects energy from or to the system. Figure 4-7 illustrates the power delivered to the load using the SMES-FCL and the power generated: it is clear that using the SMES-FCL reduces the fluctuations in the power delivered to the load. The SMES current is shown in Figure 4-8, in which it can be seen that when the generated power is higher than the reference value, the SMES absorbs this energy by charging and increasing its current; when the generated power is lower than the reference value, the SMES starts to discharge to support the load with the required uplift. The reference value can be determined by the operator according to the system specifications and is set as 0.18 MW in this example.

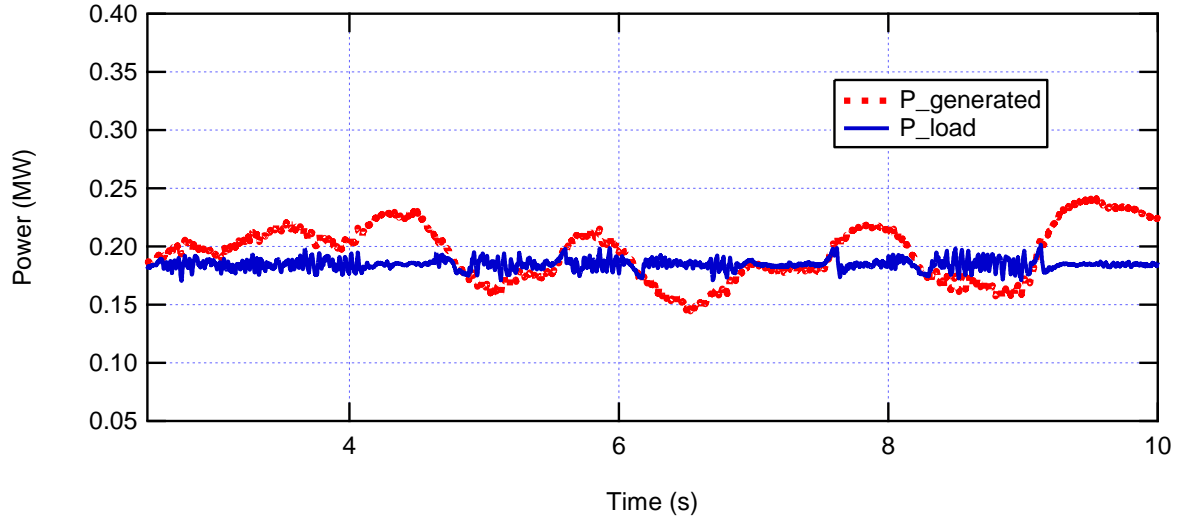


Figure 4-7 Generated power and load power

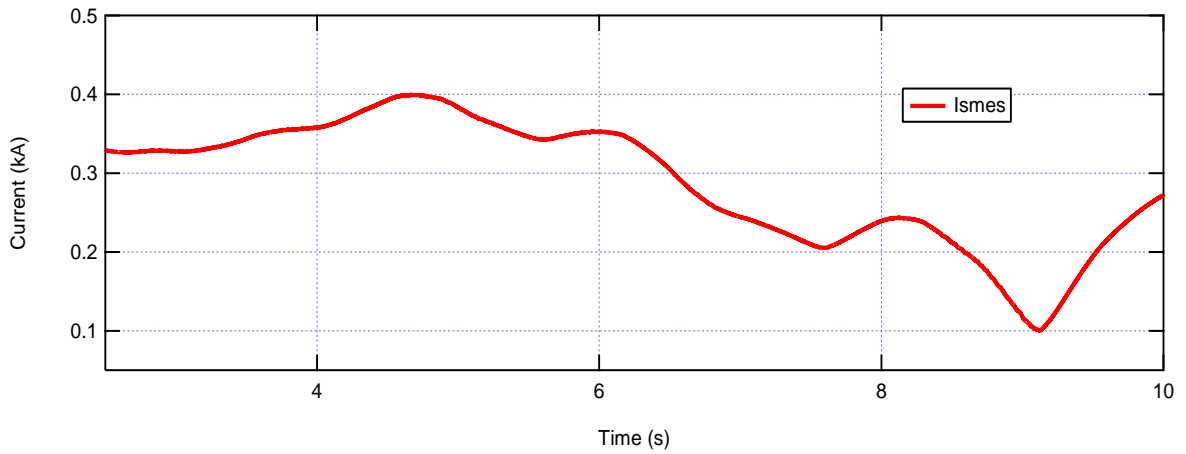


Figure 4-8 SMES current during smoothing output power operation

The second scenario to be studied relates to the energy storage function in supporting the load when a voltage drop occurs at the generator terminals. With sensitive loads, it is not acceptable to interrupt the power delivery, even if only for tens of milliseconds. In this scenario, a voltage drop is assumed to take place at the generator terminals and the consequent performance of the SMES-FCL is investigated. The drop in the voltage started after 3.5 seconds and lasts for 100 ms. Figure 4-9 illustrates the RMS voltage at the load terminals with and without the use of SMES-FCL. Although the drop only lasts for 100 ms, the voltage takes about 400 ms to return to its prospective value in the absence of the SMES-FCL. In contrast, the SMES-FCL can effectively support the system to overcome

the 0.2 kV drop in the voltage that occurs at the generator terminals and keeps the load voltage almost unaffected. The SMES current in this scenario is illustrated in Figure 4-10, where it can be seen that the SMES starts to discharge to support the load. The effect of the SMES-FCL in supporting the load is clear in the RMS value. In addition, the phase is aligned with the PLL used in the VSC, as shown in Figure 4-11 where the voltages injected at 3.5 seconds are aligned with the phase just after the drop occurs.

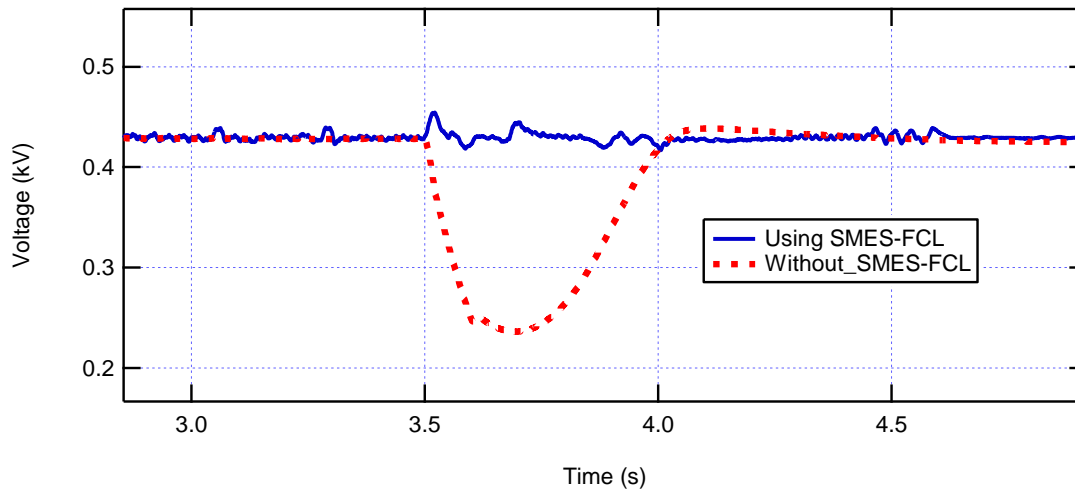


Figure 4-9 RMS voltages of the load with and without SMES-FCL following a 100 ms voltage drop at the generator terminals

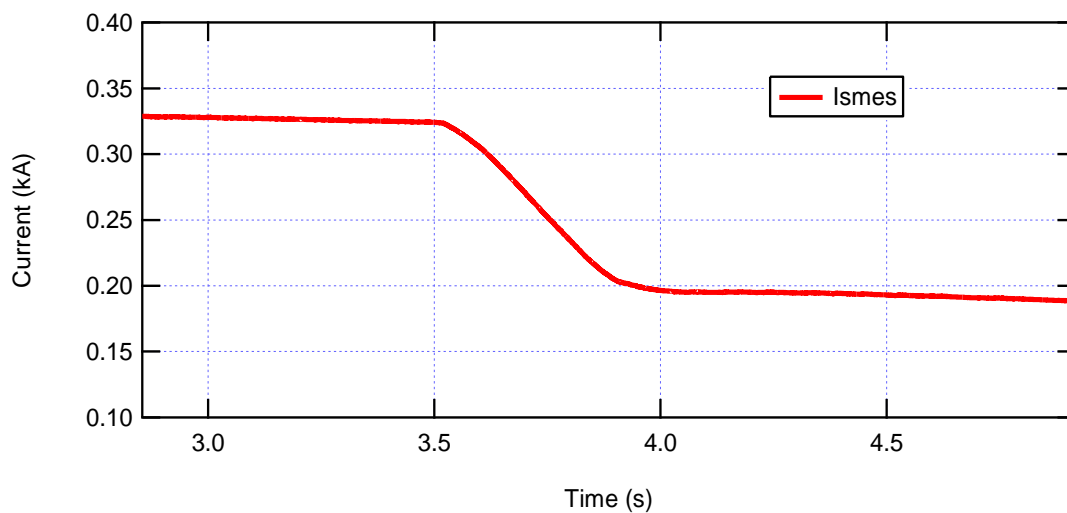


Figure 4-10 SMES current during voltage drop at the generator side

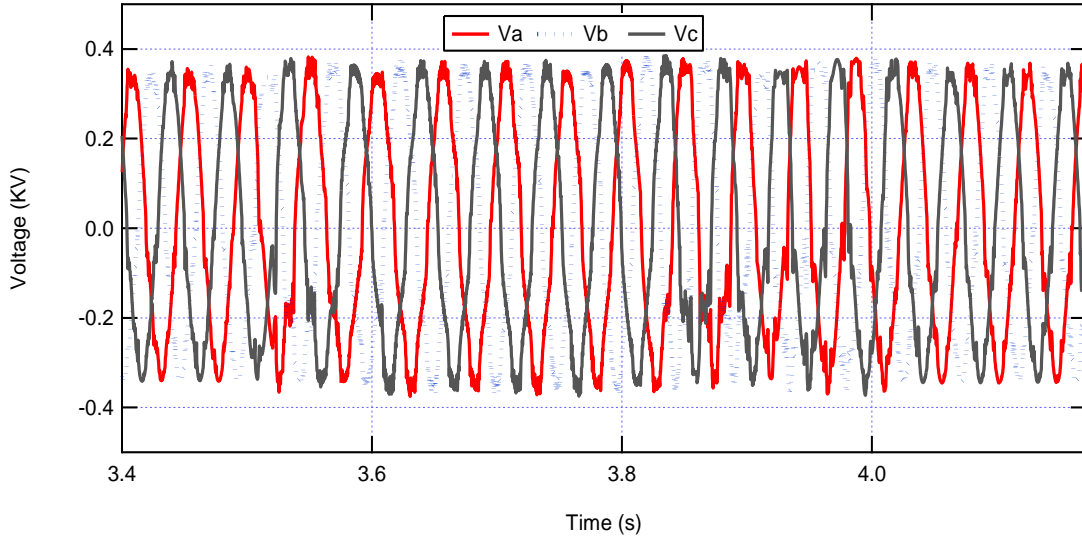


Figure 4-11 Load voltage with SMES-FCL in the case of a voltage drop at the generator terminals

4.8 Investigation of the SMES-FCL as a fault-current limiter

The effect of a fault in any power system changes according to the system itself and the parameters of the fault. In both large and small systems, the fault type and the fault resistance largely determine the magnitude of the fault current and, consequently, its effect. However, in large power systems, the distance between the fault position and the generation unit is also a major factor in the fault-current value. The fault might be three-phase-to-ground, line-to-ground or line-to-line. In this section, three scenarios will be studied. The first one is a three-phase-to-ground fault at the load terminals with a fault resistance of $0.1 \, \Omega$, while the second scenario is a three-phase-to-ground fault at the same location but with a fault resistance of $0.01 \, \Omega$. This small value is chosen to prove the effectiveness of the proposed scheme in this very small fault resistance, while the value of $0.1 \, \Omega$ is chosen to indicate the limitation effect as with higher fault resistance the prospective fault values decrease and then the limitation decrease as well. To further investigate the effectiveness of the SMES-FCL in limiting different fault types, a single line-to-ground fault is applied at the load terminals for 100 ms in a third scenario, and a fourth scenario considers a line-to-line fault. Each scenario explores the current-limitation behaviour using SMES-FCL, using SMES alone, and without either of these. To obtain

the best clarity in relation to the limitation action, the wind speed is assumed to be constant, which results in constant power output.

4.8.1 Fault scenario 1: Three-phase-to-ground fault with 0.1 Ω fault resistance

In this scenario, a three-phase-to-ground fault with a resistance of 0.1 Ω is applied at the load terminals. The fault starts after 4 seconds and lasts for 100 ms. The three-phase currents generated without using SMES or SMES-FCL are shown in Figure 4-12. The first peak of the fault reaches ~3.9 kA which is about eight times the normal current value. After the fault, the current is less than its prospective value, as is evident from the figure. As shown in Figure 4-13, using SMES alone helps to reduce the first peak and the fault currents for the entire fault period: the first peak is limited to 2.5 kA and the current value reaches 1 kA at the end of the fault period. Using SMES-FCL limits the first peak fault current to 1 kA and at the end of the fault period the current reaches ~0.75 kA, as shown in Figure 4-14, where it can be seen that the current returns to its pre-fault value just after the fault period. The effects on the voltage at the generator terminals of using SMES-FCL and SMES alone are shown in Figure 4-15. In this case, without SMES-FCL or SMES, the voltage drops to 0.15 kV (which corresponds to 0.27 pu) during the fault period because the fault resistance is not very small. Using SMES alone does not have an effect on the value of the voltage during the fault period but it helps the system to restore its pre-fault value slightly faster than without it. With SMES-FCL, the voltage drop during the fault decreased by 0.25 kV compared to the case without it; the system restores its pre-fault value smoothly in 400 ms, compared to ~1,3 without it. The active power generated, shown in Figure 4-16, also demonstrates that the SMES-FCL helps the system restore its stability faster following the fault period. During the fault period, the generated power increased to 1.3, 0.8, and 0.5 MW in the cases of not using any device, using only SMES, and using the SMES-FCL, respectively. The drop in power after the fault period is very little in the case of SMES-FCL use. Figure 4-17 illustrates the operation of the SMES-FCL coils during the fault. The current passing through the first coil (SC1), which is considered the main coil and has a larger number of turns, is constant during the fault period. This means it can retain its energy and not waste it during the fault. The other line in the figure represents the current through the smaller coil (SC2), which is responsible for the limiting action. This current was equal to that of SC1 during the normal operating mode. When the fault started, the current in this coil increased to 1.75 kA. Assuming the

critical current of these coils to be 1 kA, this means that the second coil quenched and inserted resistance to the main system, which resulted in the current-limitation action.

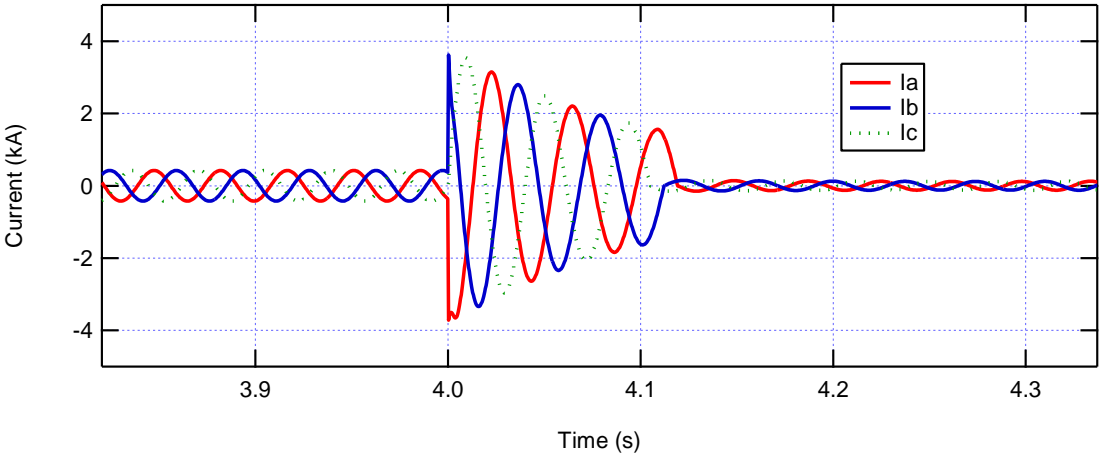


Figure 4-12 Scenario 1: generated currents without using SMES or SMES-FCL

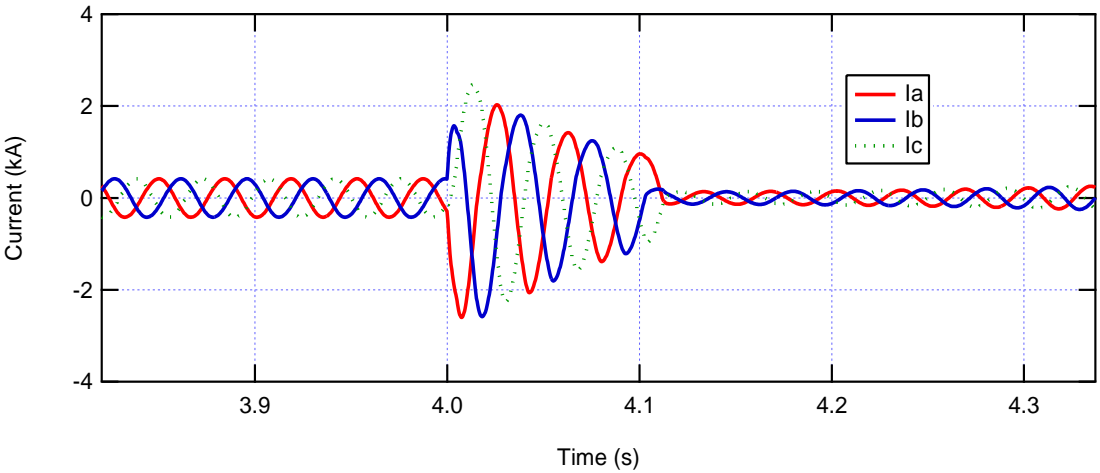


Figure 4-13 Scenario 1: generated currents using SMES only

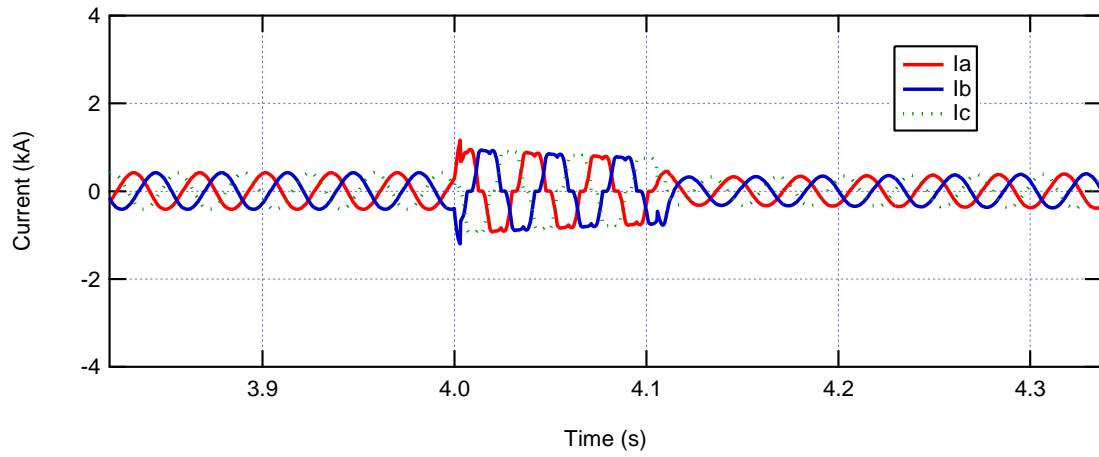


Figure 4-14 Scenario 1: generated currents using SMES-FCL

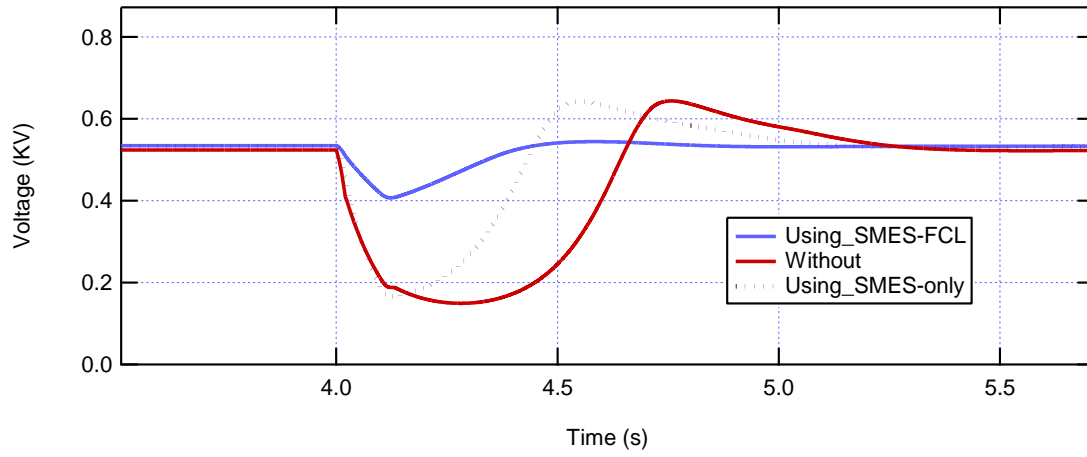


Figure 4-15 Scenario 1: RMS voltages at the generator terminals

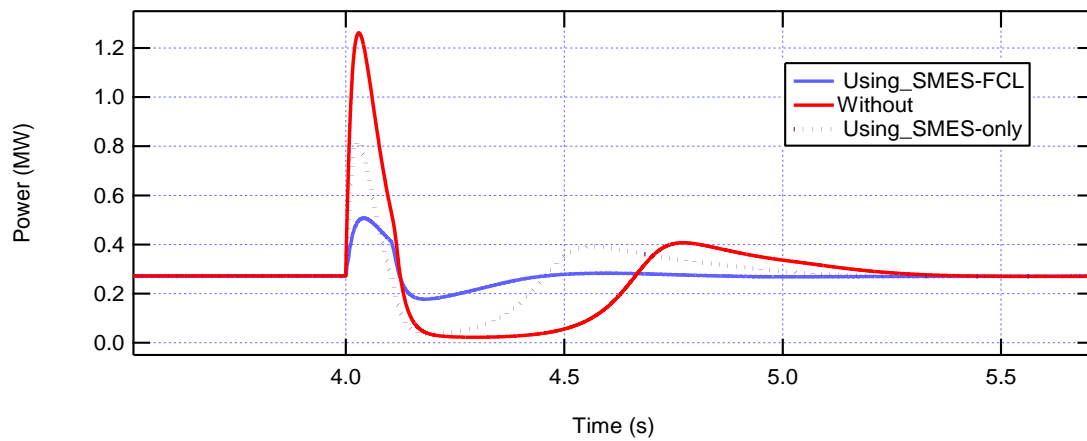


Figure 4-16 Scenario 1: active power generated

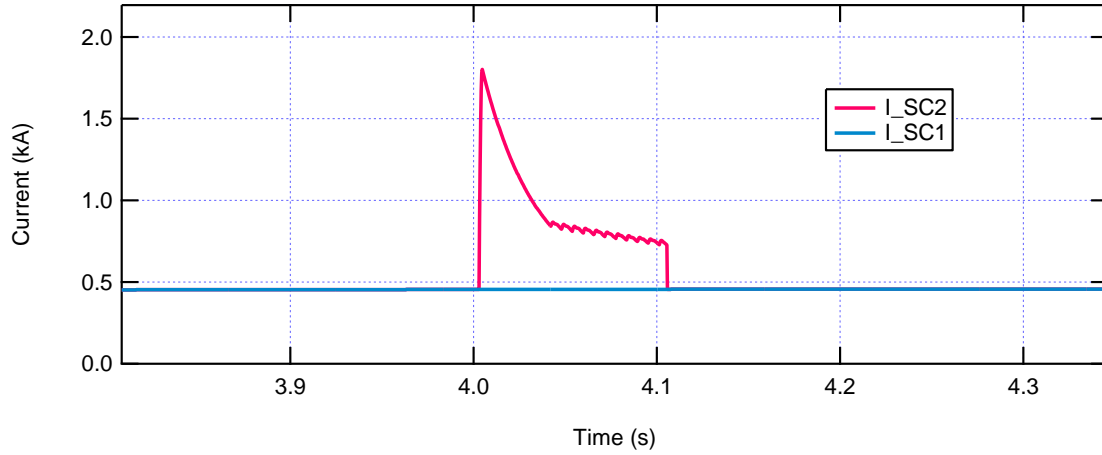


Figure 4-17 Scenario 1: currents in SMES-FCL coils SC1 and SC2

4.8.2 Fault scenario 2: Three-phase-to-ground fault with 0.01 Ω fault resistance

The same conditions and parameters of the first scenario are studied here but the fault resistance is reduced to just 0.01 Ω , which has an effect on the results. Figure 4-18 illustrates the generated currents without SMES or SMES-FCL; the first peak fault current reaches more than 15 kA and decreases to ~2 kA at the end of the fault period. Using SMES alone limits the first peak current such that it reaches only 4.3 kA and helps the current to regain its pre-fault value after 400 ms. SMES-FCL limits the first peak current to 1.1 kA, which corresponds to just 7% of its prospective value. The RMS voltage in this scenario is illustrated in Figure 4-21, and the active power generated is shown in Figure 4-22. Because the fault resistance is very low in this scenario, the voltage during the fault nearly reaches zero in the absence of SMES or SMES-FCL. Using the SMES alone quickens the return to stability after a fault by about 500 ms compared to when it is absent. In addition, the drop in the voltage with SMES lasts for just 500 ms, which compares to more than 1 s in its absence. SMES-FCL limits the drop in voltage to 0.15 kV and restores stability within 400 ms. The generated active power is shown in Figure 4-22. The spike in the generated power during the fault decreased from 1.6 MW in the case of not using any device to ~0.75 MW with SMES alone. With SMES-FCL, this value decreased further, to 0.55 MW. With SMES-FCL, the generator continues to support the system during and after the fault period, but the system's generated power falls to zero for 400 ms using SMES alone, and for about one second without either device.

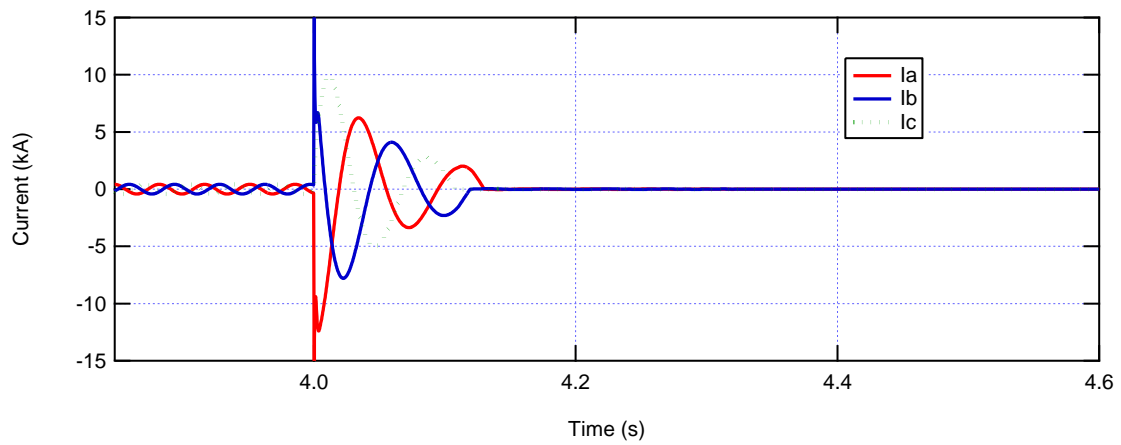


Figure 4-18 Scenario 2: generated currents without SMES or SMES-FCL

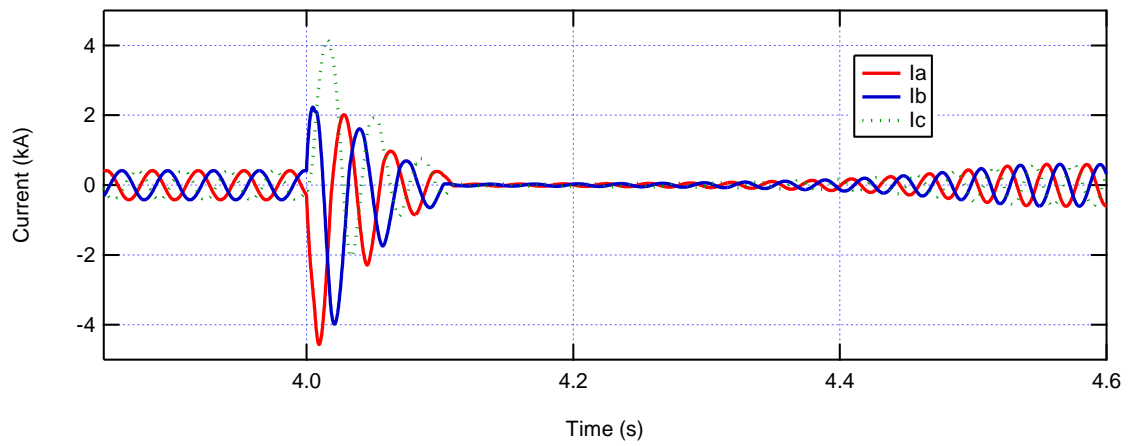


Figure 4-19 Scenario 2: generated currents using SMES only

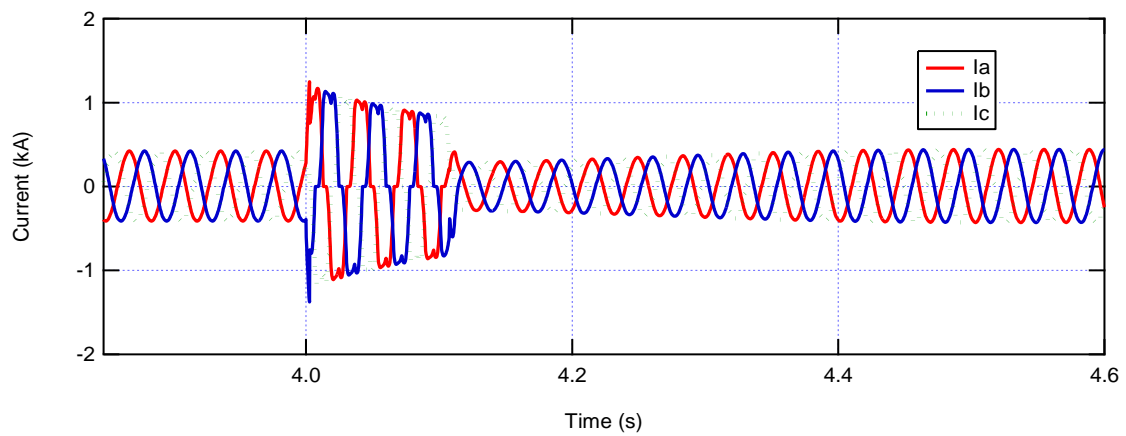


Figure 4-20 Scenario 2: generated currents using SMES-FCL

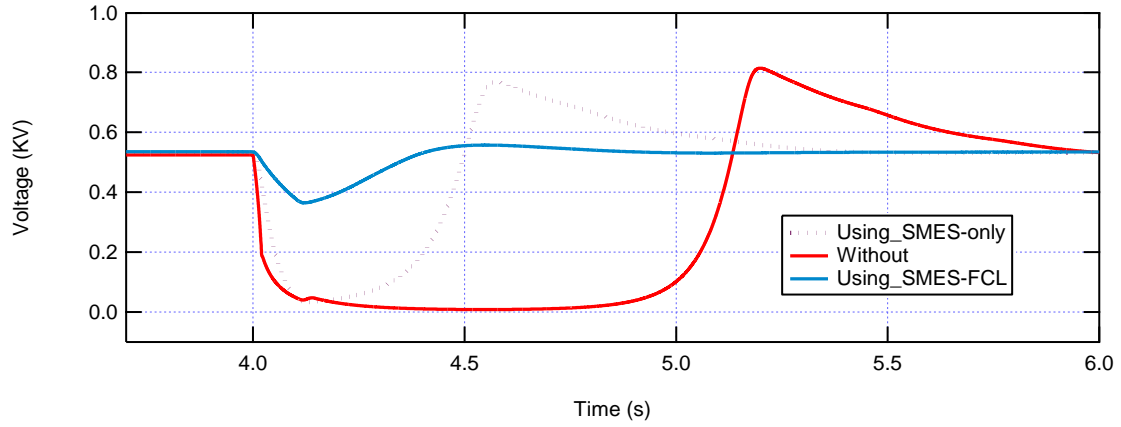


Figure 4-21 Scenario 2: RMS voltages at the generator terminals

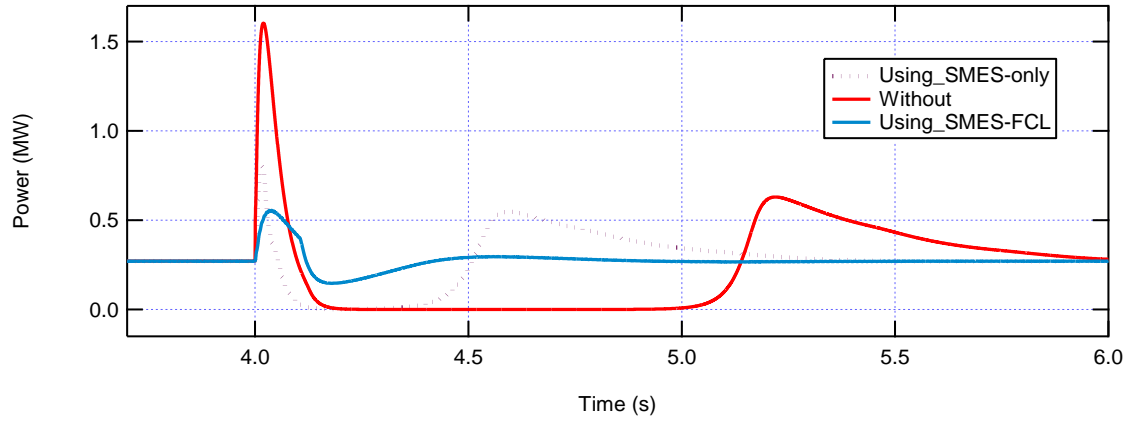


Figure 4-22 Scenario 2: active power generated

4.8.3 Fault scenario 3: Line-to-ground fault with 0.1 Ω fault resistance

The third scenario involves the application of a single line-to-ground fault at the load terminals and study of the limitation effect on the generator parameters. The same parameters are to be studied here to investigate the limitation in this fault type. Figure 4-23 shows the generated currents without SMES or SMES-FCL devices, while Figure 4-24 represents them with SMES only and Figure 4-25 with SMES-FCL. SMES-FCL effectively limits the fault current from a prospective value of 4 kA to ~0.6 kA. SMES-FCL minimizes the effects of the single line-to-ground fault, as illustrated in Figure 4-26 and Figure 4-27. With SMES-FCL, the RMS voltage almost attains its normal value during

the fault, and the increase in active power is just 0.01 MW, compared to 0.54 MW in its absence.

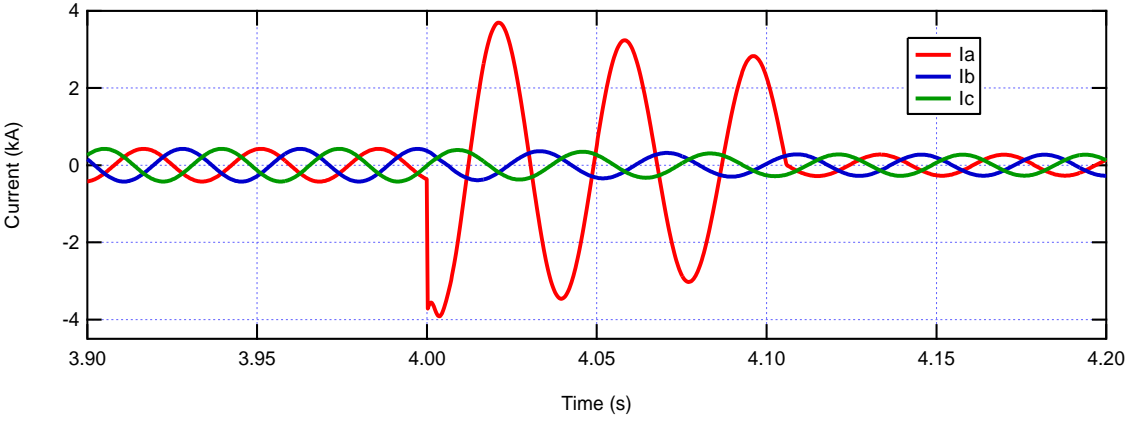


Figure 4-23 Scenario 3: generated currents without SMES or SMES-FCL

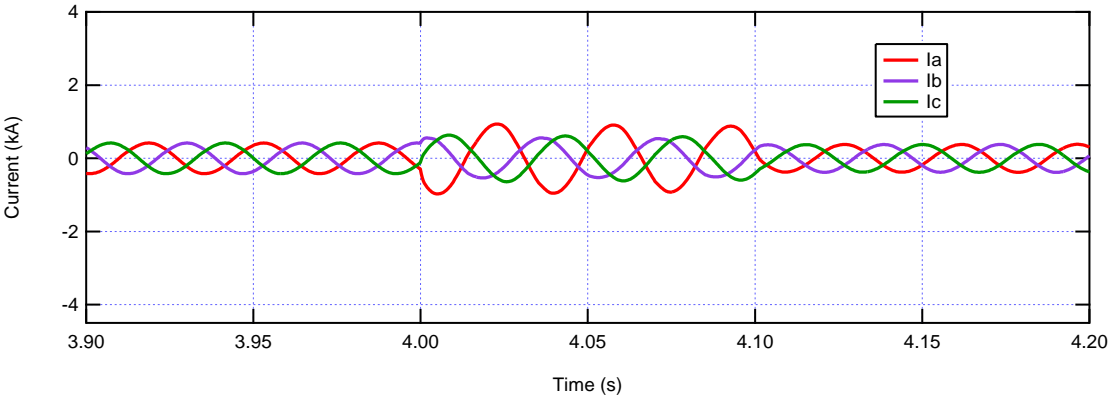


Figure 4-24 Scenario 3: generated currents using SMES only

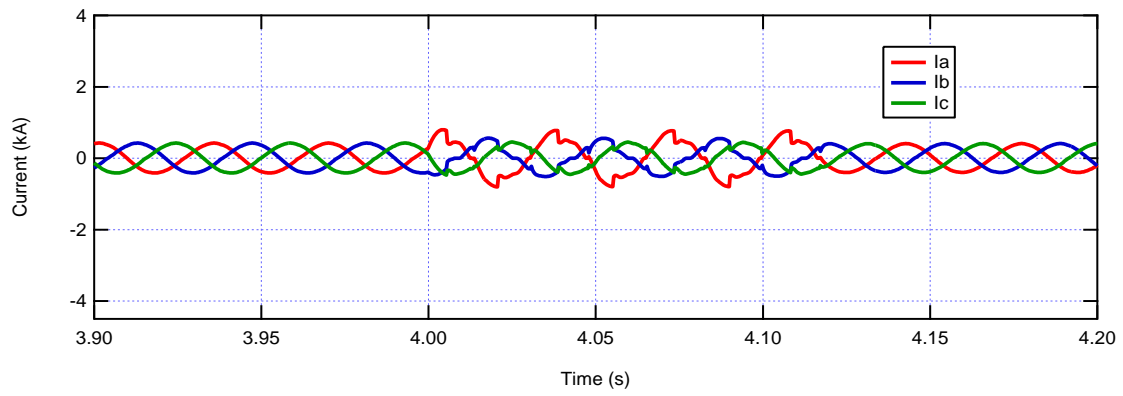


Figure 4-25 Scenario 3: generated currents using SMES-FCL

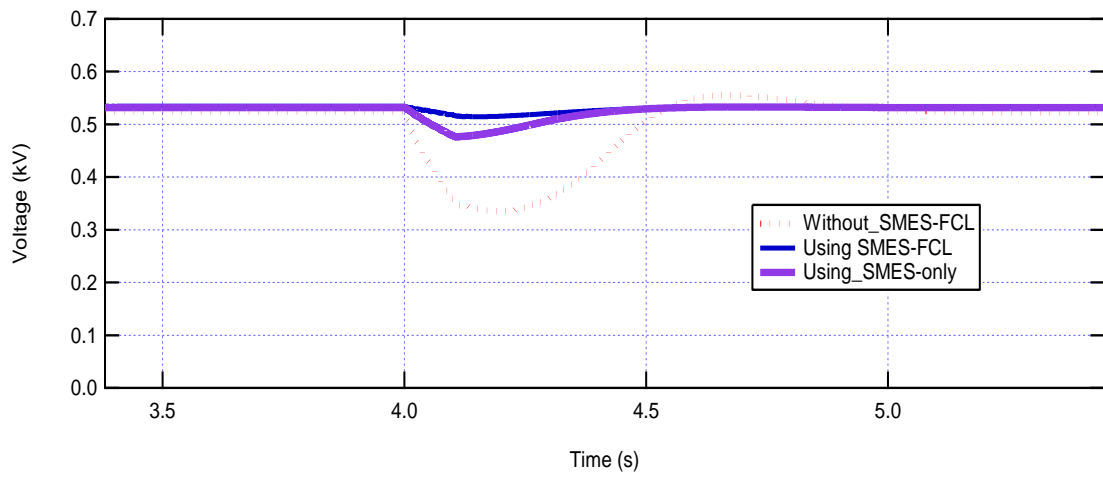


Figure 4-26 Scenario 3: RMS voltages at the generator terminals

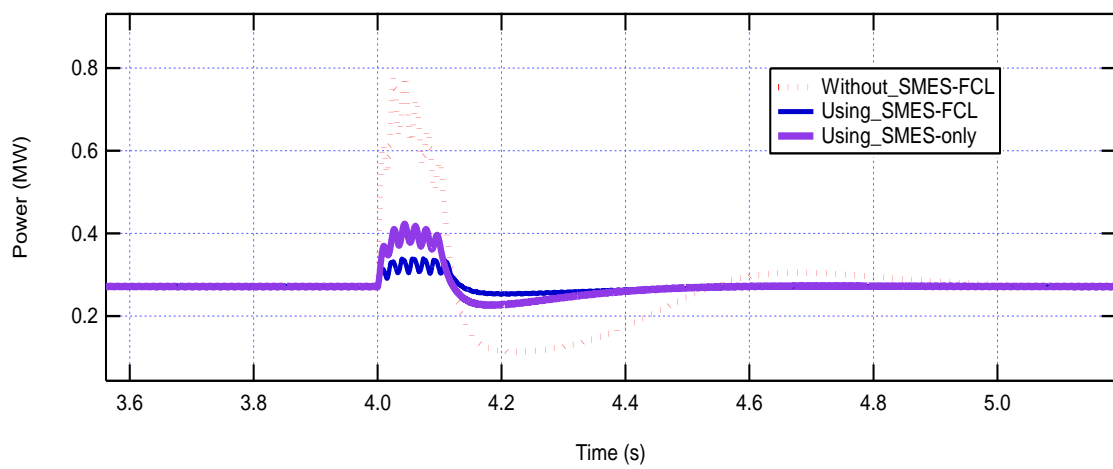


Figure 4-27 Scenario 3: active power generated

4.8.4 Fault scenario 4: Line-to-line fault with 0.1 Ω fault resistance

In the final fault scenario, a line-to-line fault is applied between phases *a* and *b*. The three-phase currents of the generator without SMES-FCL are shown in Figure 4-28. The two faulted phases have an average current value of 3.8 kA during the fault period. With SMES-FCL, this value is limited to ~ 1 kA, as shown in Figure 4-29.

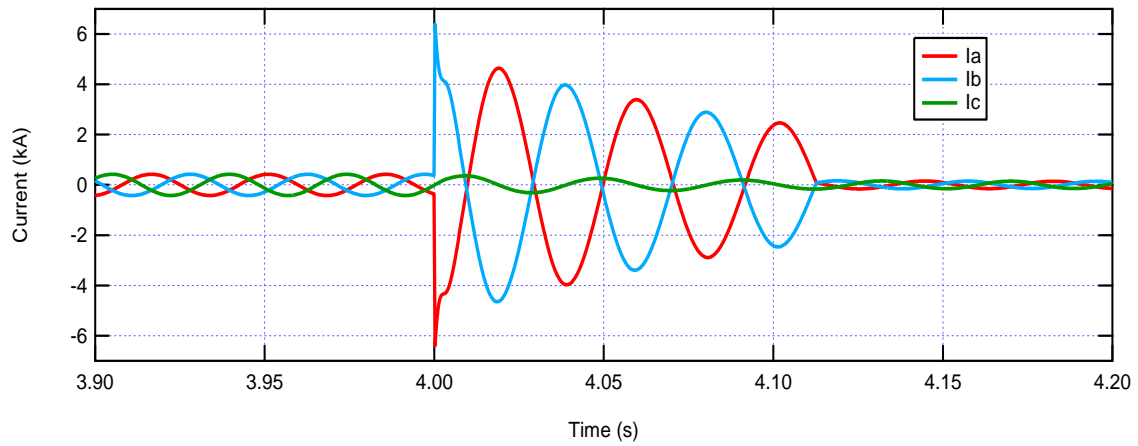


Figure 4-28 Scenario 4: generated currents without SMES-FCL

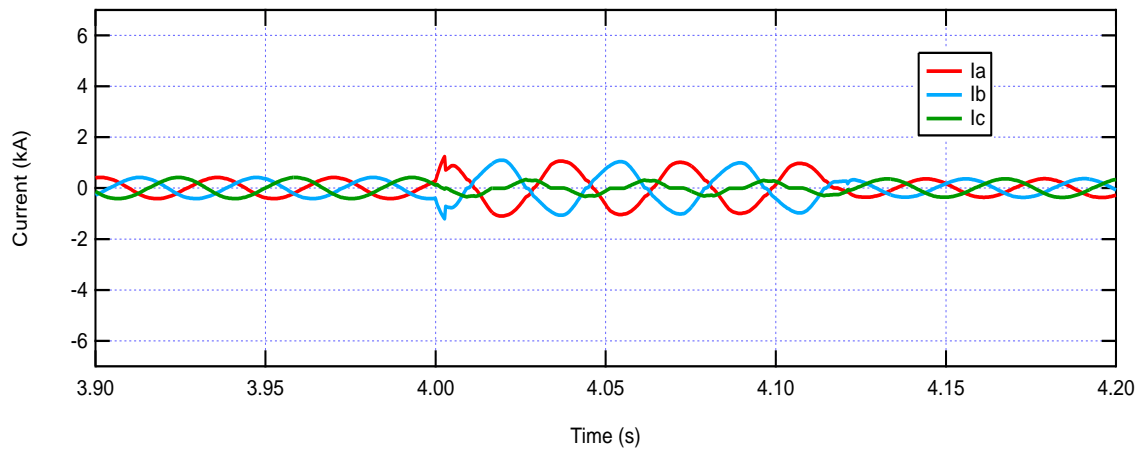


Figure 4-29 Scenario 4: generated currents with SMES-FCL

The results from these four fault scenarios show the benefits of using SMES-FCL for fault limitation. As previously stated, the extent of the current limitation depends on the level

of resistance introduced by the superconducting coils during faults. This resistance can be changed by changing the number of pancakes inserted into the system during the fault period. Depending upon the specific objective of the current limitation, a SMES-FCL system can be designed accordingly. SMES-FCL can be used for the integration of new generation units into an existing power system to lower the fault levels such that they remain compatible with the existing protection system. In this case, the fault current must not be limited to such low values that the protection system cannot detect it.

4.9 Summary

This chapter introduced a SMES-FCL system as a multifunctional device to limit fault currents, in addition to its energy storage function. This system depends on designing a control circuit to switch the operation modes between energy storage and fault current limitation modes. The performance of the proposed system was investigated in a wind energy-based power system. The SMES-FCL could effectively smooth the output power generated from the wind turbine generator. During a voltage dip at the generator terminals, the SMES-FCL supports the load at its full power and compensates for the voltage drop at the load terminals.

The performance of the system in limiting fault currents in different fault scenarios was investigated, with four scenarios covering different fault resistances and fault types. Within all cases, SMES-FCL could limit the fault currents to low levels and also improve the fault ride-through capability of the system; the system restores its stability faster with SMES-FCL. Moreover, the voltage profile of the SMES-FCL system during the faults shows good enhancement in relation to grid code requirements. Using such systems should encourage the integration of new wind turbine generators into the existing power networks without the need to upgrade the protection system. Moreover, in three-phase AC systems, instead of using three SFCLs (one per phase), this new approach uses only one SFCL coil that can be inserted into the three phases according to the fault condition. In addition, coordination between this system and the protection system can be undertaken to achieve full protection for the whole system within a few milliseconds.

Despite these promising results, the cost of the superconducting materials remains a big issue, but this SMES-FCL concept may be applicable within the next few years with a significant drop in the price of the superconducting materials and further developments

in cryogenic systems. Further studies need to be carried out on the thermal and mechanical stresses on the coils, especially large ones as special precautions must be done to ensure the mechanical and thermal stability of the system, which may requires addition costs.

Chapter 5

Application of SMES-FCL in DC grids

This chapter considers the use of SMES in limiting fault currents in DC systems. First, a simulation system is built to investigate the circuit and choose suitable parameters. Then a system is built in an experimental platform and tested in terms of its energy storage and fault-current-limiting functions. Finally, a wind turbine generator system based on a doubly-fed induction generator (DFIG) is built with MATLAB/Simulink and connected to a DC line. The effect of SMES-FCL on this DC system is investigated under different scenarios.

5.1 Introduction

With recent developments in power electronics technologies, renewable-energy-based DC grids have been widely investigated [123] [124]. Many distribution generation outputs are in DC form so it is more straightforward to be connected to a DC network than an AC one. This will save unnecessary power-conditioning steps, which will also lower losses and save cost. In addition, with the increases in DC loads such as electric vehicles, solid-state lighting, and speed controllers for ventilation and air conditioning systems [125], DC grids are often the best option. Although in some cases there will be a need to incorporate a power-conversion stage, DC grids also can perform with high efficiency by increasing the transmission voltage. Nowadays, there are several examples of DC grids in marine, aviation, automotive, and manufacturing industries [126].

In the case of wind energy, most wind turbine generators are located remotely from the load demand. In this regard, connecting wind farms to remote grids or loads using DC lines will be more efficient. The problems associated with wind energy integration into DC grids are similar to those of AC grids; the intermittent nature of the generation is still an issue with DC grids. Fault ride-through capability and load support during faults are still important issues too. Wind turbine generators have been connected to DC grids in several projects previously. Thus, a squirrel-cage induction generator-based wind farm was connected to a DC microgrid with a diode rectifier and a capacitor bank [127], and a permanent-magnet synchronous generator wind turbine system was connected to a DC

grid [128]. Variable schemes to connect wind turbines to DC systems also have been introduced [129] [130].

In general, DC grids are more sensitive to faults than AC grids. The DC fault amplitude depends on the type and location of the fault. Because the resistance of the DC line is small and the fault can be supplied with the sources and capacitors, the fault currents could be catastrophic [131] [132]. In terms of protection devices, DC grids cannot use normal circuit breakers that depend on the zero-crossing trip. Recently, several solutions have been proposed to reduce fault currents in DC grids. The normal method is fault isolation, which depends on normal AC circuit breakers placed on the AC side of interconnector stations [133]. However, in multi-terminal DC networks, placing the circuit breaker on the AC side might lead to de-energization of the whole DC network [134]. Special types of circuit breakers have been proposed for DC grids, such as moulded-case, isolated-case, and hybrid DC circuit breakers [135] [134].

Superconducting fault-current limiters (SFCL) have also been proposed to limit fault currents in high-voltage DC (HVDC) systems [136] [137]. In addition, integration of an SFCL with circuit breakers to achieve current limitation and tripping with suitable fault currents has been proposed [138] [134].

This chapter uses an SMES system to limit the DC fault currents in a DC system, which allows the circuit breakers to trip at lower values and enables the wind turbine generator to remain connected and support loads during the fault period and after fault clearance. The system is built and tested in a simple DC system. It is investigated in simulation and experimental platforms. Following this, a DFIG-DC system is simulated in MATLAB/Simulink and the effectiveness of SMES-FCL in supporting this system's stability and fault ride-through capability is investigated.

5.2 Principle of operation of the DC SMES-FCL

The idea of the DC SMES-FCL is similar to that of the AC SMES-FCL, which is described in Chapter 4, but the connection of the circuit and the control scheme change to fit the DC system. To use the device as a SMES, the whole SC coil is used in the normal operational mode to charge or discharge energy to the main system as required. Only a portion of the SMES is separated and used as a resistive-type superconducting FCL. The

two coils are referred to as SC1 and SC2 in Figure 5-1. Both are used as energy storage coils but only SC2 is used as a fault-current limiter; SC1 is isolated during fault conditions to reduce heat losses and allow it to retain its stored energy.

When connecting the SMES system to a DC grid, it does not need the AC-to-DC conversion stage, which represents a significant cost saving and reduces system complexity. It uses only a DC chopper as a power-conditioning stage. The main control circuit used for the SMES is an H-bridge. This contains two IGBT switches (Q1 & Q2) and two diodes (D1 & D2), as shown in Figure 5-1. Two further diodes (D3 & D4) and three more IGBT switches (Q3, Q4 & Q5) are also connected to the H-bridge, in addition to Q6, which is connected in series with the main DC line. The operational modes of the SMES-FCL are determined by the reference value of the current in the main system. When the current in the main system (I_{dc}) is lower than the reference value (I_{ref}), the system operates in normal operational mode or energy storage mode. When the current in the main system is higher than the reference value, the system operates in fault-current-limitation mode.

During the energy storage mode, switches Q4 and Q6 are kept on, switches Q3 and Q5 are kept off, and the two diodes D3 and D4 are forward- and reverse-biased, respectively. The two main IGBT switches (Q1 & Q2) are turned on or off according to the voltage on the DC line in the connection point. When the voltage is higher than the reference value, the two switches are turned on and off to charge the coil. When the voltage is lower than the reference value, Q1 and Q2 are switched off while the two diodes D1 and D2 are forward-biased to discharge the coil and support the main system. If the voltage is the same as the reference value, the coil retains its energy by circulating it through Q2 and D2. When the current increases to fault level, Q6 is opened while Q5 is closed to allow the high system current to pass through SC1. Once the current reaches the critical value of the coils, SC2 quenches and introduces resistance to the main system for the duration of the fault.

The resistance of the superconducting material increases to a high value, determined by the precise current and temperature. More details about the behaviour of superconducting material during such faults can be found in Chapter 3. The other major concern during this period is isolation of the rest of the SC (SC1) to maintain its energy. This is done by

opening Q4 and closing Q3 and Q1, with D1 forward-biased to allow the stored current to circulate.

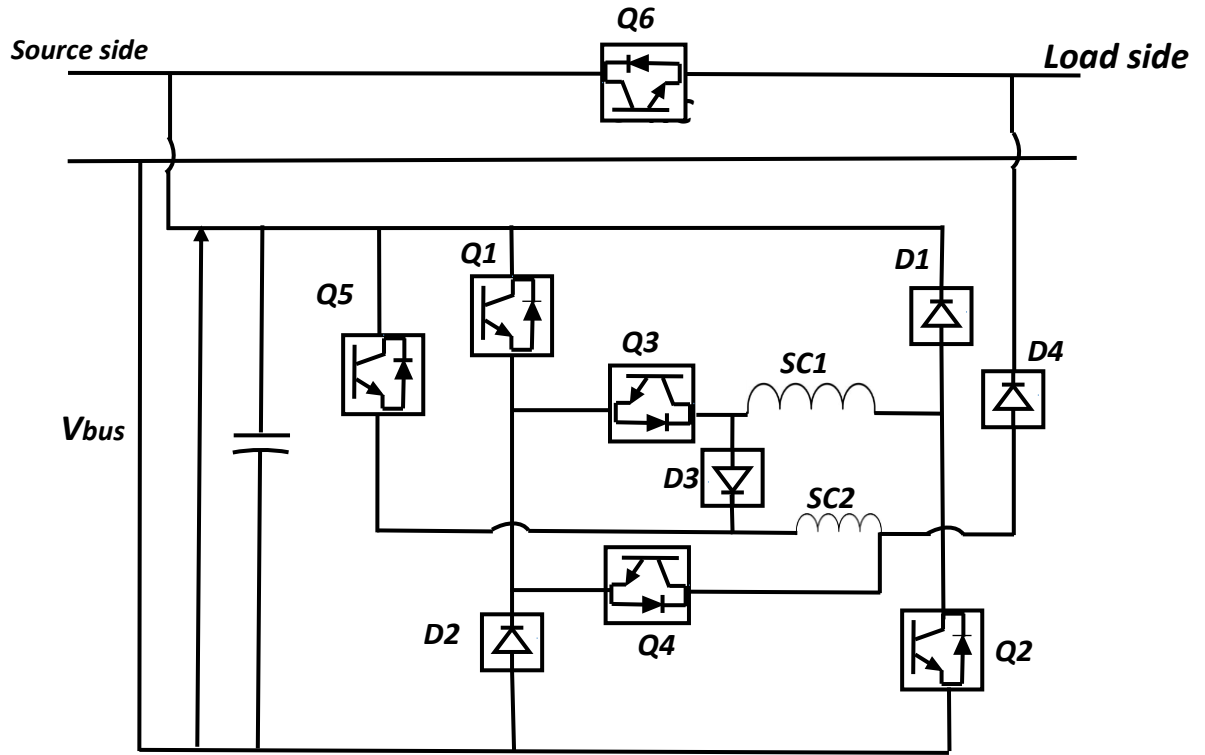


Figure 5-1 Circuit configuration of the DC SMES-FCL

The operational modes of this system are illustrated in Figure 5-2 and can be summarized as follows:

If $I_{dc} < I_{ref}$: (Energy storage mode)

Q3, Q5, D4: OFF

Q4, Q6, D3: ON

Q1, Q2: ON or OFF

If $I_{dc} > I_{ref}$: (Fault-current-limitation mode)

Q3, Q5, D4, Q1, D1: ON

Q4, Q6, D3, Q2, D2: OFF

The limitation in current is determined mainly by the value of the FCL resistance, which depends on the number of pancakes that are used for this purpose (as well as for energy

storage). The limitation on the current must be chosen carefully in order not to limit the current to values lower than the protection system settings. If the latter occurs, it will prevent the protection system from recognizing the fault. The aim is not to prevent the protection system from tripping but to decrease the rating of the circuit breakers, and provide limitation in the case of any protection failure. In addition, adding more generation units to an existing system may require an upgrade of the protection system to higher values. However, by using the current-limitation function we can decrease the fault-current magnitude, aligning it to the rating of the existing circuit breakers and avoiding the need to upgrade them. . On the studied systems, only current limitation with the proposed SMES-FCL and the circuit breaker ratings and operation are not simulated to consider the protection system failure.

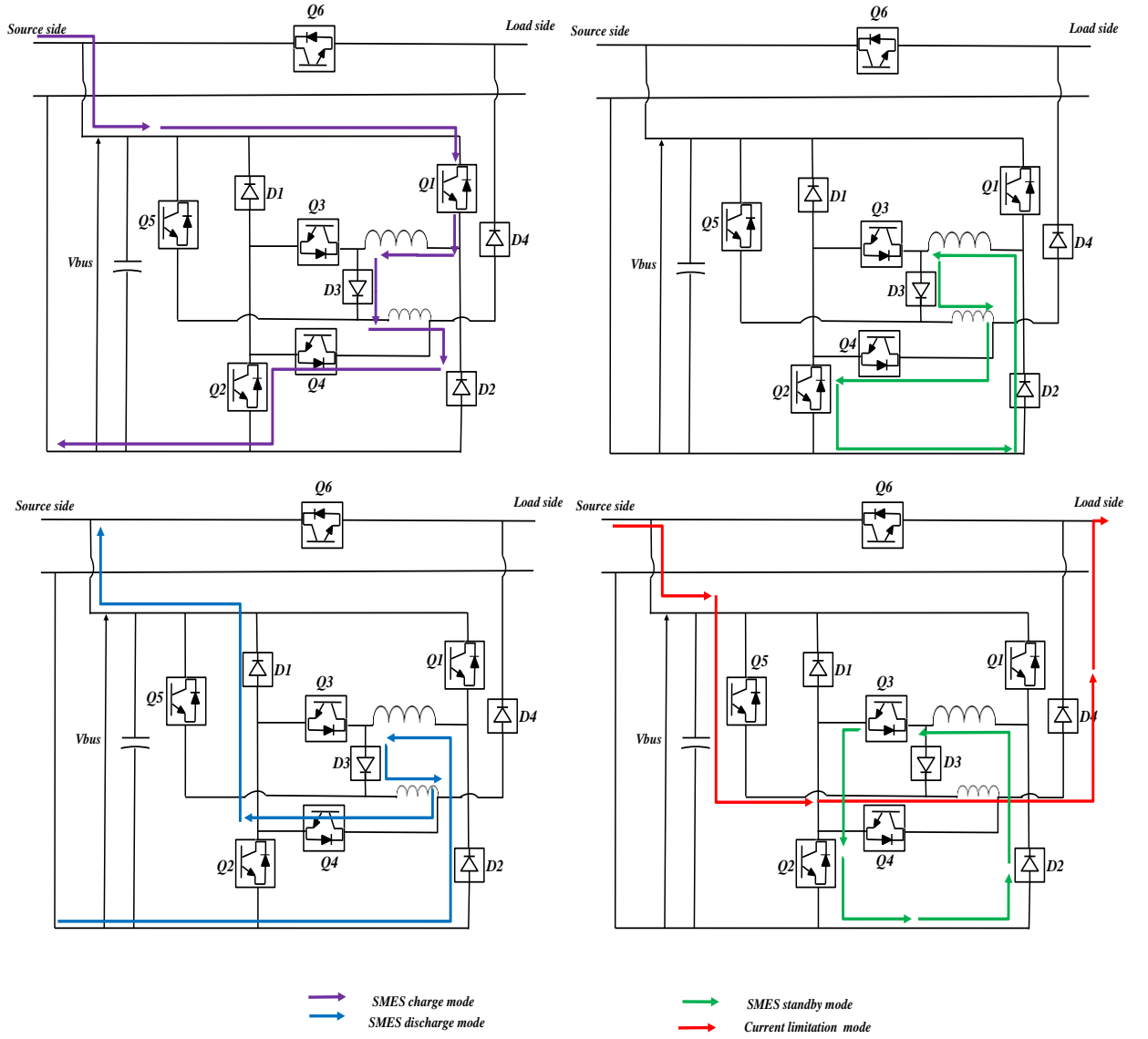


Figure 5-2 DC SMES-FCL modes of operation

5.3 Simulation results for DC SMES-FCL

The DC SMES-FCL system is built and tested using MATLAB/Simulink. A controllable voltage source is used to simulate the variation of the voltage on the source side. An increase and a decrease in the source voltage are simulated to test the charge and discharge of the SMES system. The normal value of the load voltage is 7.15 V, which is taken as the reference for the system. For the SMES coil, different inductance values are used to illustrate the effect on SMES performance of varying the inductance. Figure 5-3 illustrates the load voltage during the variation of the source voltage for coils of different inductances; the higher the coil inductance, the higher the energy stored and the better the

performance. The inductance values for coils L1 to L4 are 0.5, 0.3, 0.1 and .05 H, respectively. SMES improves the voltage profile by a noticeable amount even with the lowest inductance value. In coils L1 and L2, SMES absorbs most of the increase in source power and delivers the same reference voltage to the load, as well as supporting the load voltage for the whole duration of the voltage drop.

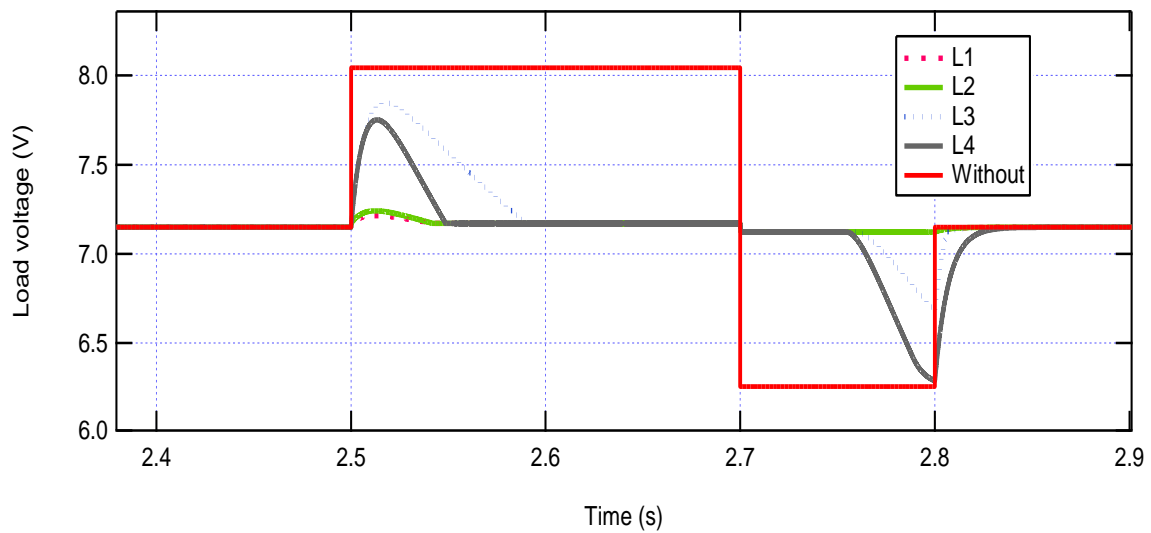


Figure 5-3 Load voltage with increase and decrease in the source-voltage value

The fault-current limitation is also tested in a MATLAB simulation by applying a DC fault on the load side and focusing on the limitation effect on the source current. The SC responsible for the current limitation is represented by resistance with a switch in parallel. The switch is normally closed and is opened when the current is higher than the reference value in the main system. The current that passes through this coil in the fault case must be greater than the critical current to cause it to quench and increase the resistance such that the fault current is reduced. As shown in Figure 5-4, increasing the resistance of the coil increases the current limitation up until a certain limit. R1, R2, and R3 have resistance values of 0.5, 0.3, and 0.1 Ω , respectively. As previously stated, the value of the resistance depends on the number of pancakes used for current limitation and the length of the pancake. R3 reduces the fault current from 32 A to 24.5 A, while R1 and R2 both exert limitations of about 20 A below the prospective fault-current value.

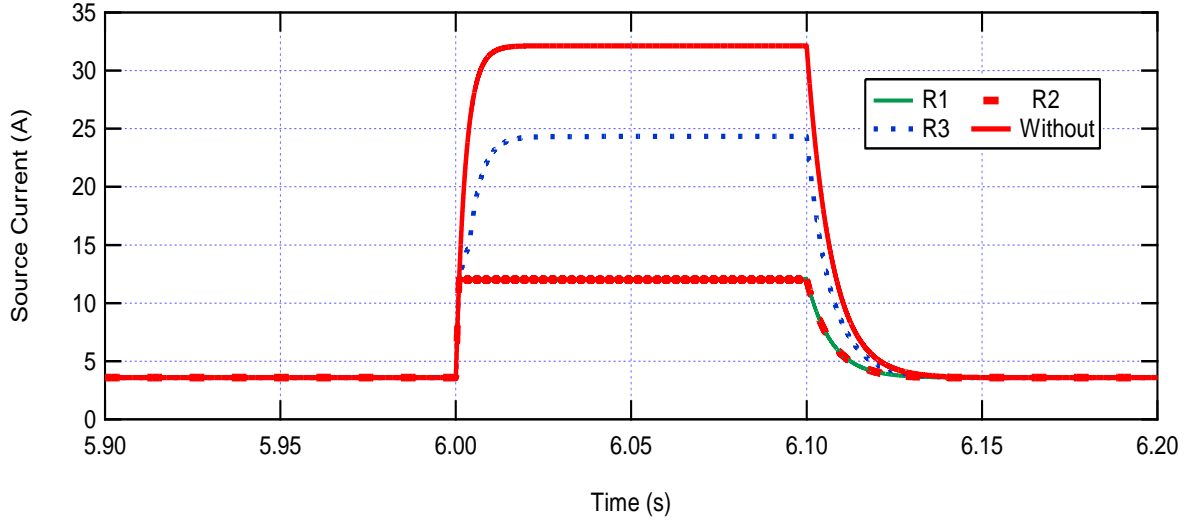


Figure 5-4 Source currents during the DC fault for different coil resistances

5.4 DC quench test of the superconducting coils

The proposed scheme depends on the use of the SC as a fault-current limiter in addition to its energy storage function in a DC circuit. Hence, the quench of the SC represents a major aspect of the investigation. The resistive-type fault-current-limitation concept that is used in our proposed system depends on a rapid switch from a superconducting to a resistive state, which can be as short as 1.7–3 ms [139]. To investigate the quench behaviour of an SC tape after winding, a test circuit is built, as shown in Figure 5-5. The tape length is 4 m and it is wound with an inner diameter of 5 cm and an outer diameter of 6.5 cm.

To ensure that the voltage across different parts of the coils increases at the same rate as the current, the voltage is measured at three different parts of the coil. Three voltage tapes are connected to the coil at lengths of 100, 200 and 400 cm, the latter representing the entire length of the coil. The coil is then immersed in liquid nitrogen and connected to a controllable DC power supply.

The current and voltage measurements are monitored with a data acquisition (DAQ) card from National Instruments [NI cDAQ-9174], with the output processed on a PC. The E-J curve of the SC at the three different locations is illustrated in Figure 5-6. V1 represents the voltage per cm for the entire coil, while V2 and V3 represent the voltage per cm at partial coil lengths of 200 cm and 100 cm, respectively. As evident from this figure, the

increase in the voltage with respect to current is very similar at all three points. This means that the quench occurs at approximately the same time throughout the coil, which prevents overheating or damage to it. The voltage starts to increase at a value of ~ 125 A, which represents the critical current for the coil. After that, a high-current pulsed waveform is applied to the coil to monitor the voltage at the coil terminals during high current flow. Different pulse currents are applied with varying amplitudes and the corresponding voltages along the coil are monitored. In case I1, a pulse current of 120 A is applied at the coil and the correspondence voltage V1 is measured, as shown in Figure 5-7. This operation is then repeated with higher currents of 130 A, as I2, and 140 A, as I3. With 120 A, which is lower than the critical current, the voltage across the coil appears to be proportional to the rate of change of current only, as shown in Figure 5-8. This means that with this current value the coil introduces only inductance, which represents the energy storage mode. When the current increases to 130 A, the voltage starts to acquire a resistive voltage component, but it is still not very large, which indicates that the resistance of the coil starts to rise above that of its superconductive state. Finally, with 140 A, the voltage starts to be proportional to the current waveform, which means that the resistive voltage component has become higher than the inductive voltage component, as shown in Figure 5-9. This case represents the current-limiting mode in which the SC resistance increases to limit high currents.

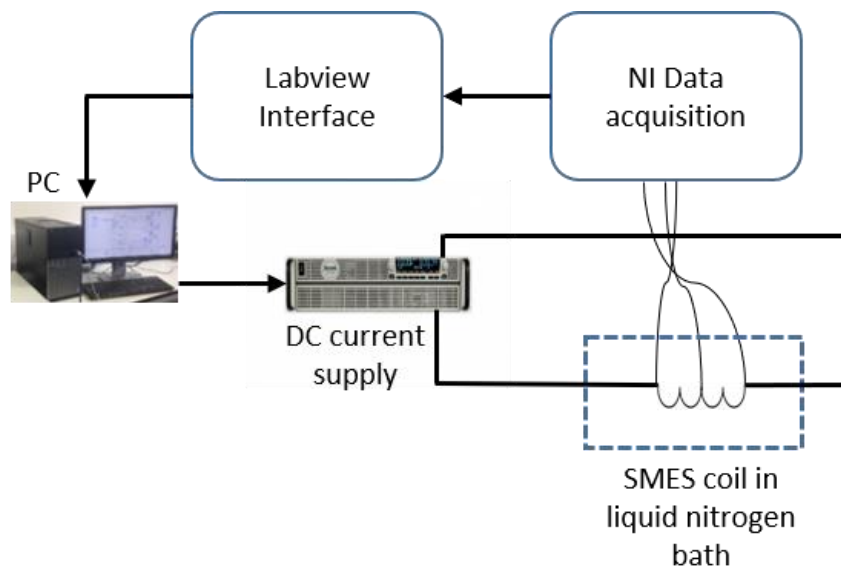


Figure 5-5 Connection diagram for the DC quench test

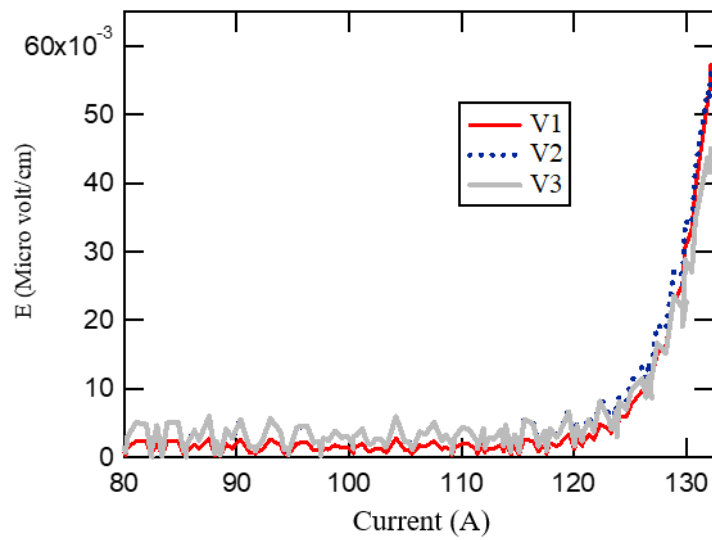


Figure 5-6 E-J c/cs of the superconducting coil at different locations along the coil

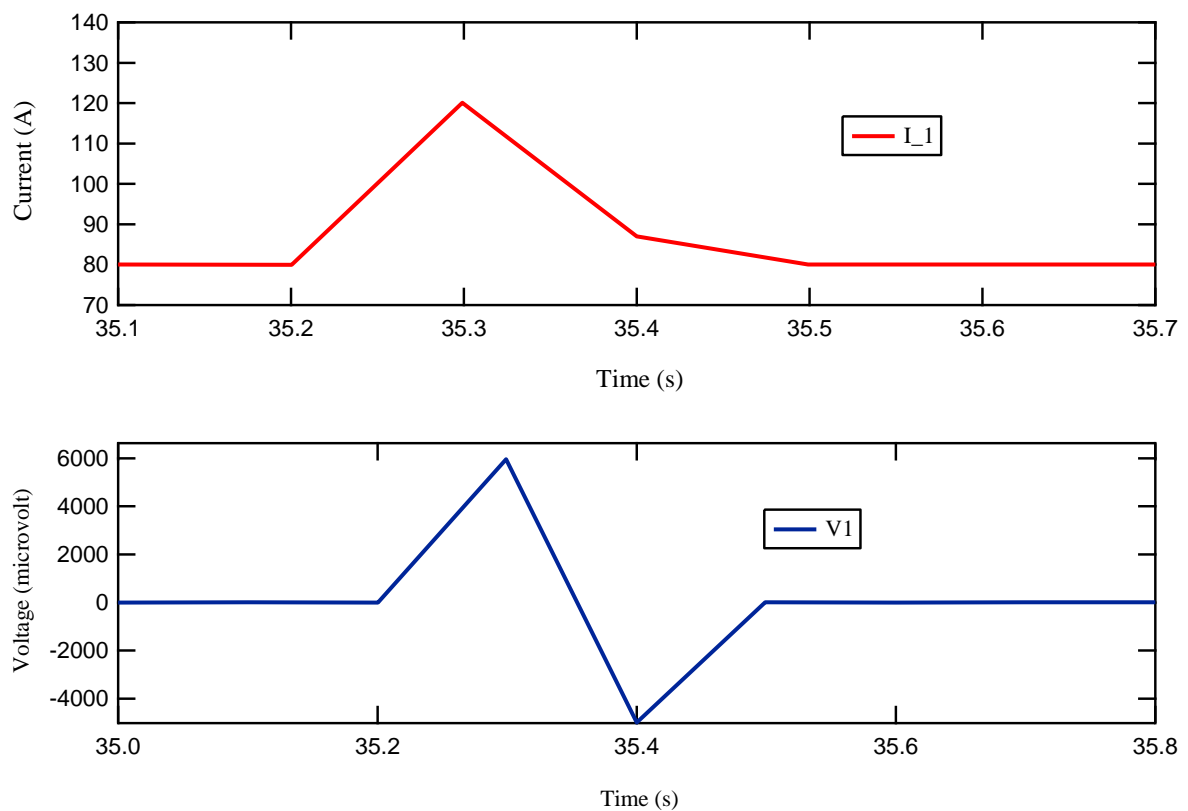


Figure 5-7 Current pulse I_1 (120 A) and voltage on the tape for the DC quench test

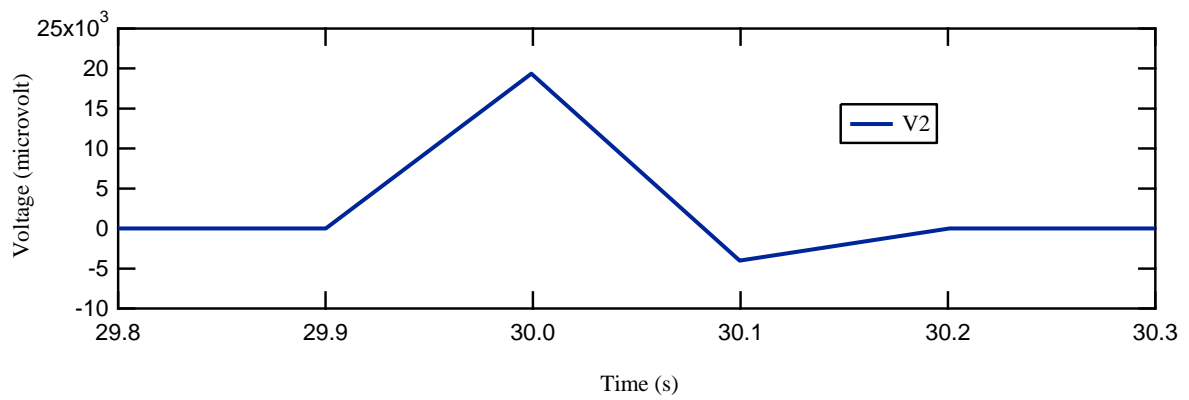
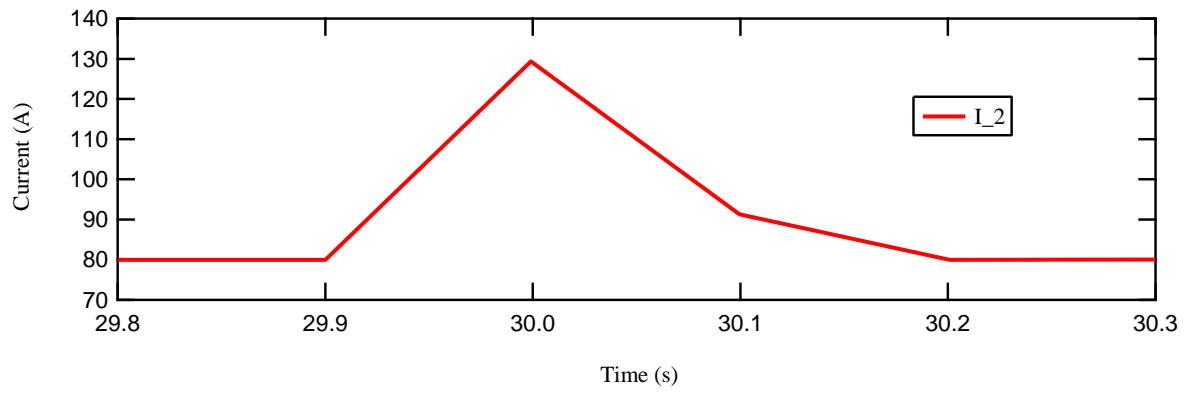


Figure 5-8 Current pulse I₂ (130 A) and voltage on the tape for the DC quench test

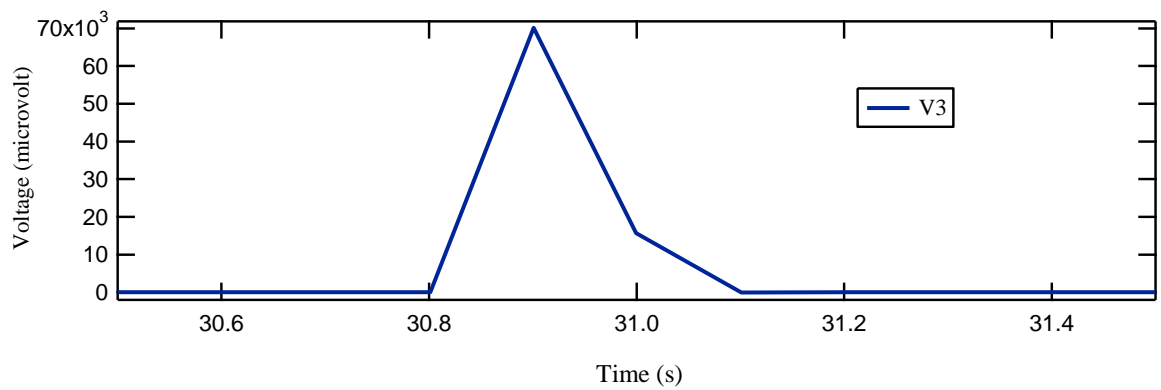
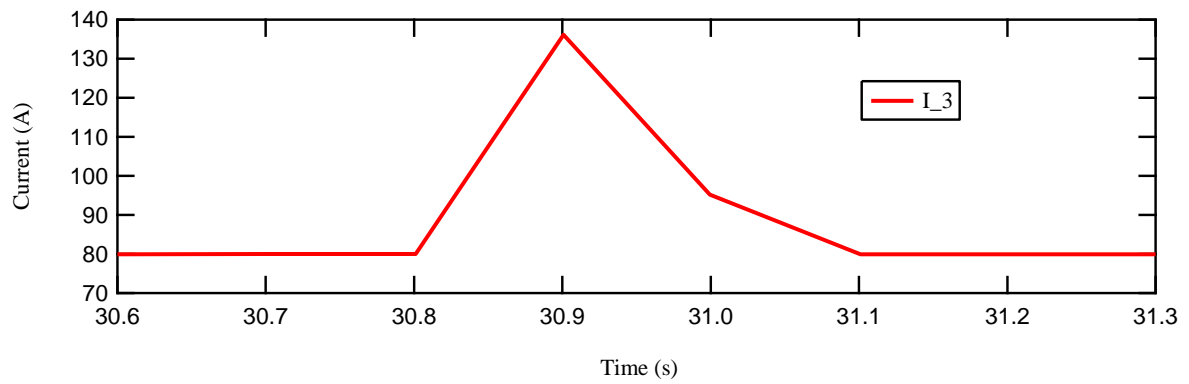


Figure 5-9 Current pulse I₃ (140 A) and voltage on the tape for the DC quench test

5.5 Experimental test of the SMES-FCL in a DC system

After testing the proposed SMES-FCL system in a simulation, a small-scale system was built to test it in a DC system. The experimental test consisted of a controllable DC power supply that is used to simulate the cases of a voltage increase, a voltage drop and a power change at the source side. The load is represented by a resistor and the line has a small resistance value to limit the current. The SMES-FCL circuit is built as described in section II above. The SMES coil used in this experiment is a double-pancake coil formed from a YBCO tape made by SuperPower Inc. (Schenectady, NY, USA). The components used in the experimental test are listed in

Table 5-1. The system is tested first in normal operational mode and a reference value for the voltage at the connection point with the SMES-FCL system is established. The control sequence is set on the PC using the LabView interface and pulses are sent to the IGBTs using the DAQ card. The experimental set-up is shown in Figure 5-10.

Table 5-1 Components used in the experimental test

Element	Number	Details
DC power supply	1	TDK-Lambda GSP10-1000 10V/1000A
R_{line}	1	0.16 Ω , 300 W
R_{load}	1	0.5 Ω , 100 W
Capacitor	1	47,000 μ F
IGBTs	7	IKW40N120CS6
Diodes	4	FFSB3065B-F085
Data acquisition system	1	National Instruments DAQ system
SMES coil	1	<ul style="list-style-type: none"> • 2-pancake coil • Inner radius 45 mm; outer radius 73 mm • Rated current 33 A; critical current 45 A
Fault-current limiter	1	Emulated by a resistor in parallel with a power electronic switch

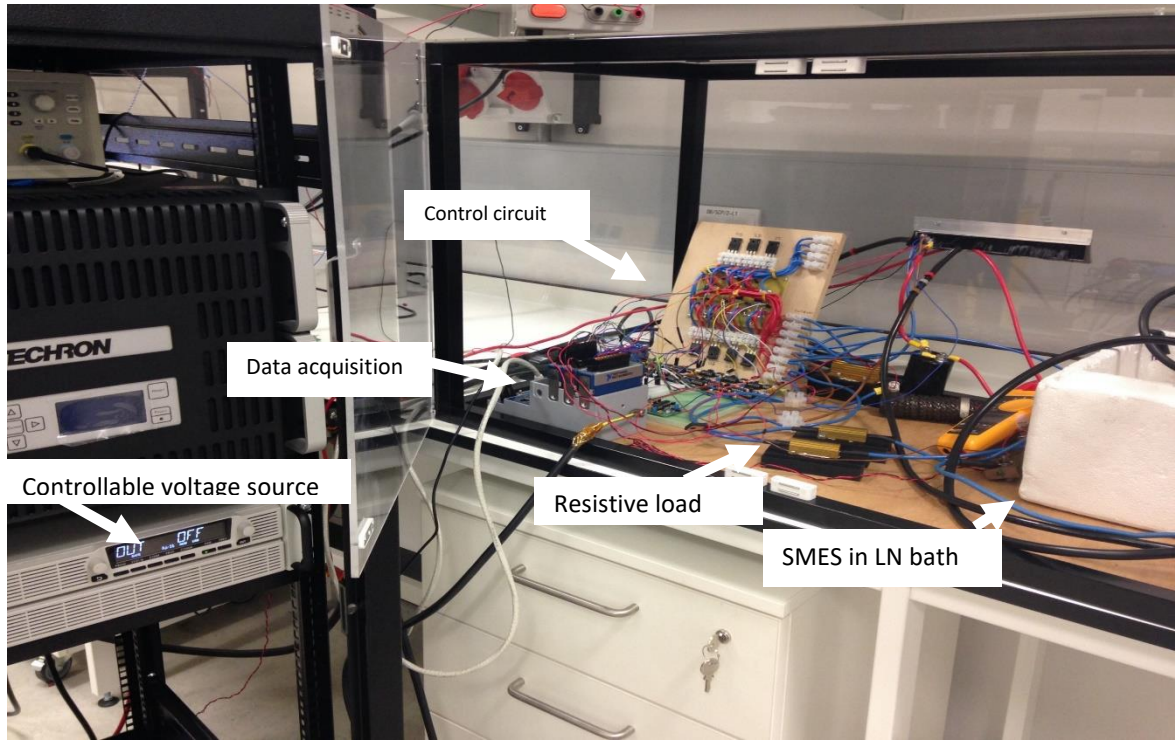


Figure 5-10 Experimental set-up (LN = liquid nitrogen)

First, the efficacy of the SMES-FCL as an energy storage device was studied. The SMES coil can store up to 30 J at an operating current of 20 A. However, the voltage rating for the power supply is 10 V, which restricts the current in the system to lower values. Thus, the SMES coil is tested only in terms of charging and not storage. The DC source is controlled to give a high-current pulse of 10 A for a short period before returning to the normal value, which is set as 6 A. The reference values for the control system can be set by the operator according to the system requirements. During this case, the reference voltage is 4 V. Figure 5-11 illustrates the voltage at the connection point with and without the SMES-FCL. During the high-current disturbance, the SMES coil reduces the value of the voltage to 5.2 V, instead of the 6.35 V seen in its absence. The currents at the load side and the connection point are shown in Figure 5-12 and the SMES current is shown in Figure 5-13. From these figures, it can be seen that the SMES coil absorbs about 2.1 A from the source current, which results in a reduction of the increase in the load-side current to 1.8 A instead of 4 A.

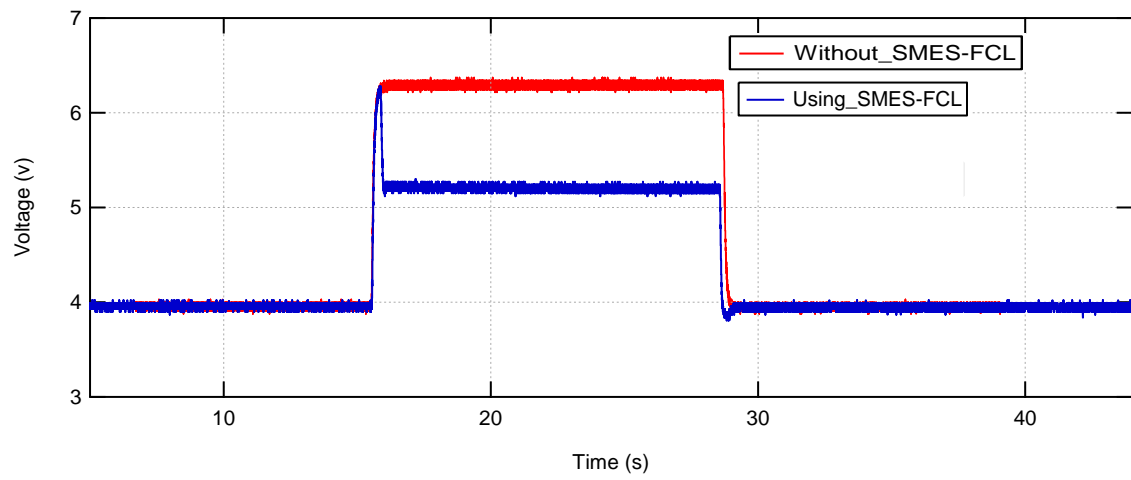


Figure 5-11 Connection-point voltage with and without SMES-FCL during an increase in the source current

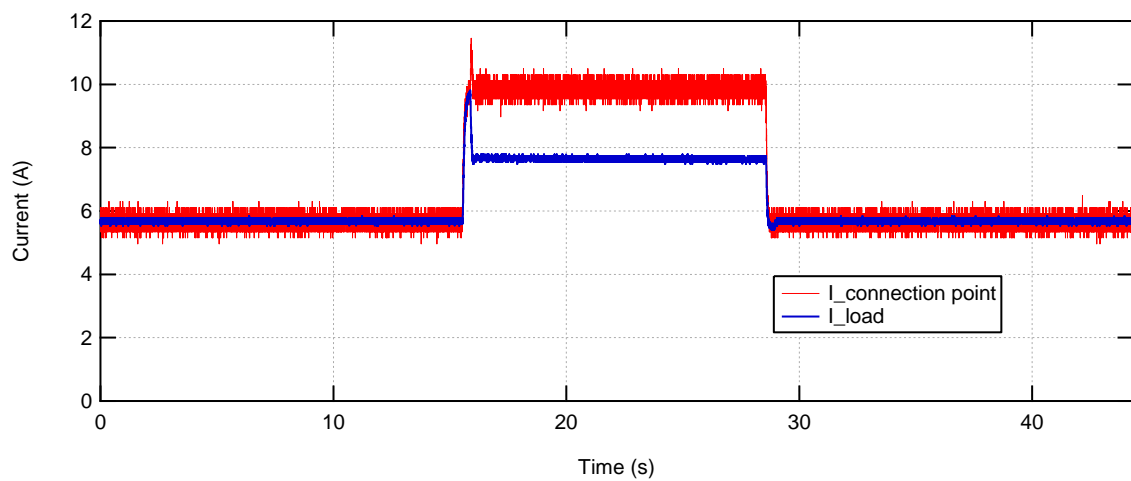


Figure 5-12 Currents in the connection point and the load during an increase in the source current

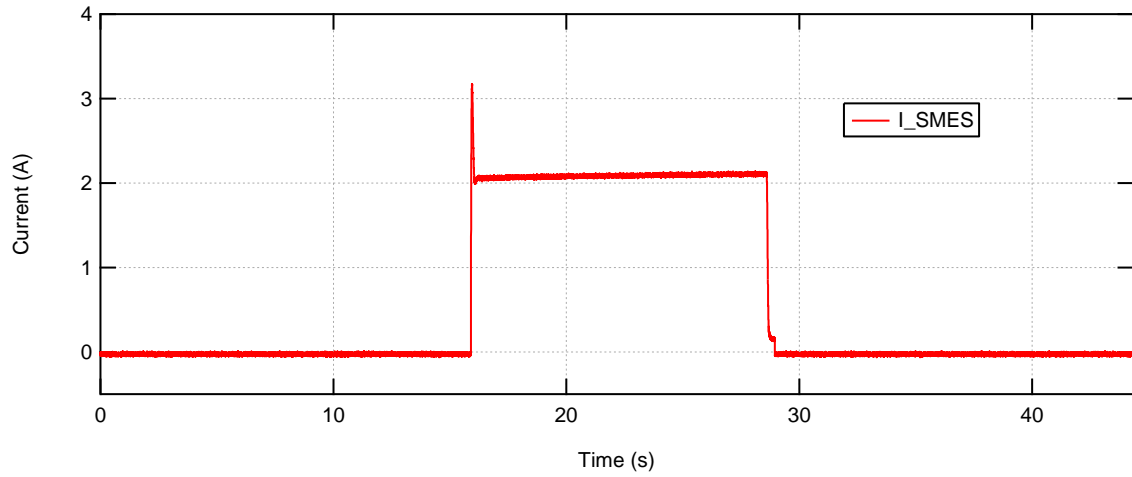


Figure 5-13 SMES-coil current during an increase in the source current

The second case considers an increase in the voltage at the source side. The source voltage increases suddenly from its normal value of 5 V to 9 V before returning to its normal value. Figure 5-14 shows the voltage at the connection point with and without SMES-FCL. The voltage increased to 7.6 V without SMES-FCL but was limited to 6.4 V through the charging of the SMES coil. As shown in Figure 5-15, the current increased to ~15.8 A in the absence of SMES-FCL. With SMES-FCL, this value is reduced to ~9.8 A through the charging of the SMES coil, as illustrated in Figure 5-16.

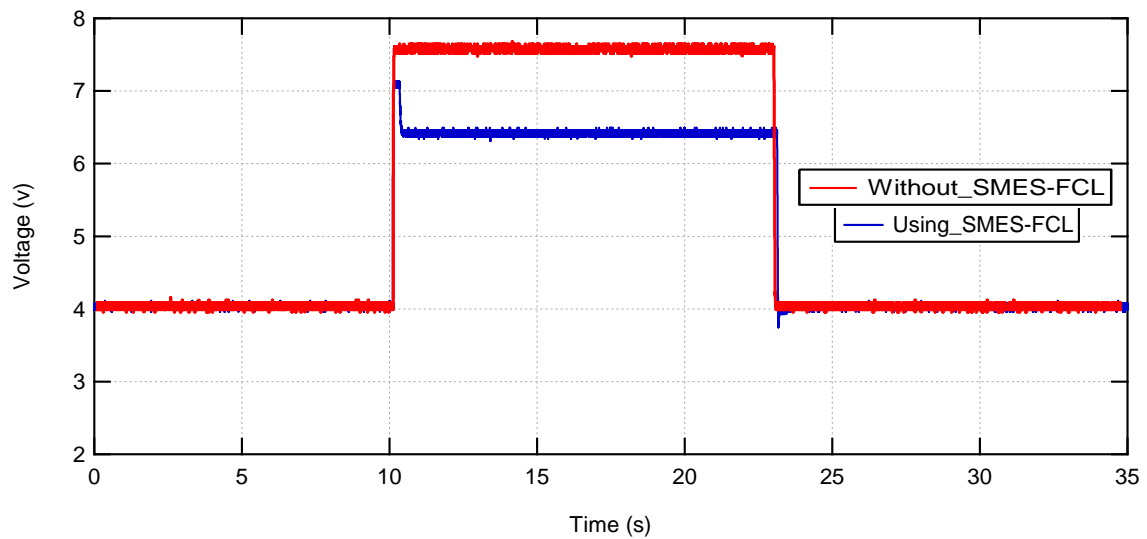


Figure 5-14 Connection-point voltage with and without SMES-FCL during an increase in the source voltage

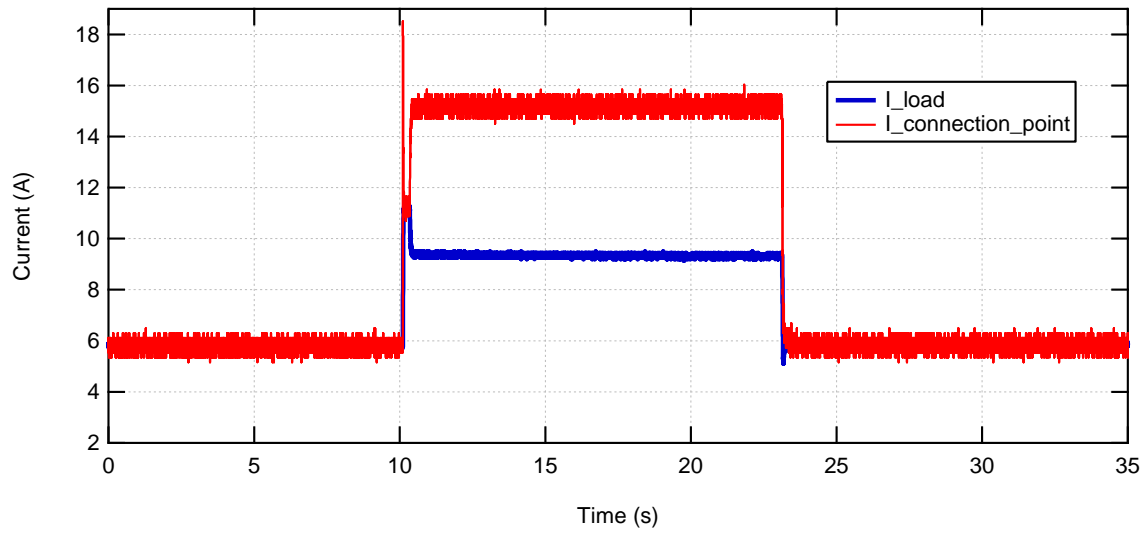


Figure 5-15 Currents in the connection point and the load during an increase in the source voltage

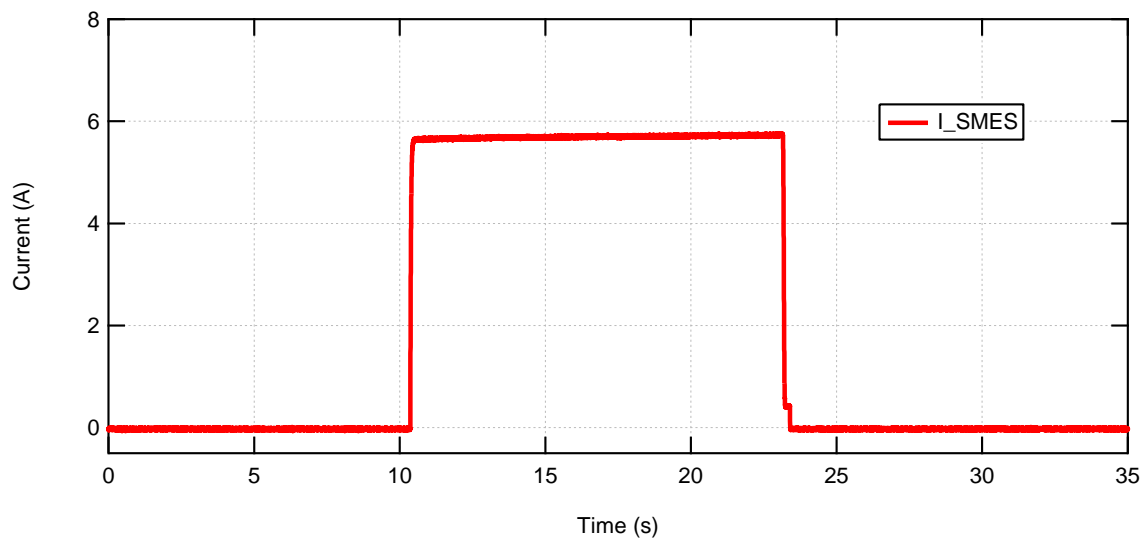


Figure 5-16 SMES-coil current during an increase in the source current

A current-limitation test was carried out by increasing the current in the main circuit to a value above the reference value. The critical current chosen for this system is 7 A. To simulate the fault case, the load is short-circuited by connecting an IGBT in parallel with it. The current in the main circuit increased to 13 A without SMES-FCL, as shown in

Figure 5-17. Using SMES-FCL limits the value of the current during the short circuit to 8 A, which represents a limitation of approximately 40% from the prospective value. However, the limitation exhibits a time delay because of the switching time of the DAQ system. The voltage at the connection point with the SMES-FCL is shown in Figure 5-18; the enhancement in the voltage is clear from this figure. During the fault period, without SMES-FCL, the voltage dropped from 3.25 to 1.8 V. With SMES-FCL, the drop in the voltage decreased to 0.65 V within milliseconds of the start of the fault. The voltage profile is very important in large power systems because it affects the performance of the generator during fault periods and determines whether or not it complies with the relevant grid code(s).

This experimental test proved the capability of the proposed technique to limit fault currents. The delay in the limitation was caused by the DAQ and not by the control sequence itself. Thus, high-speed sensors are required to detect the increase in the current and send pulses to the switches. In addition, the proposed system was used to store energy albeit with higher voltage and current ratings to avoid losing the power charge in the coil as ohmic losses in the switches.

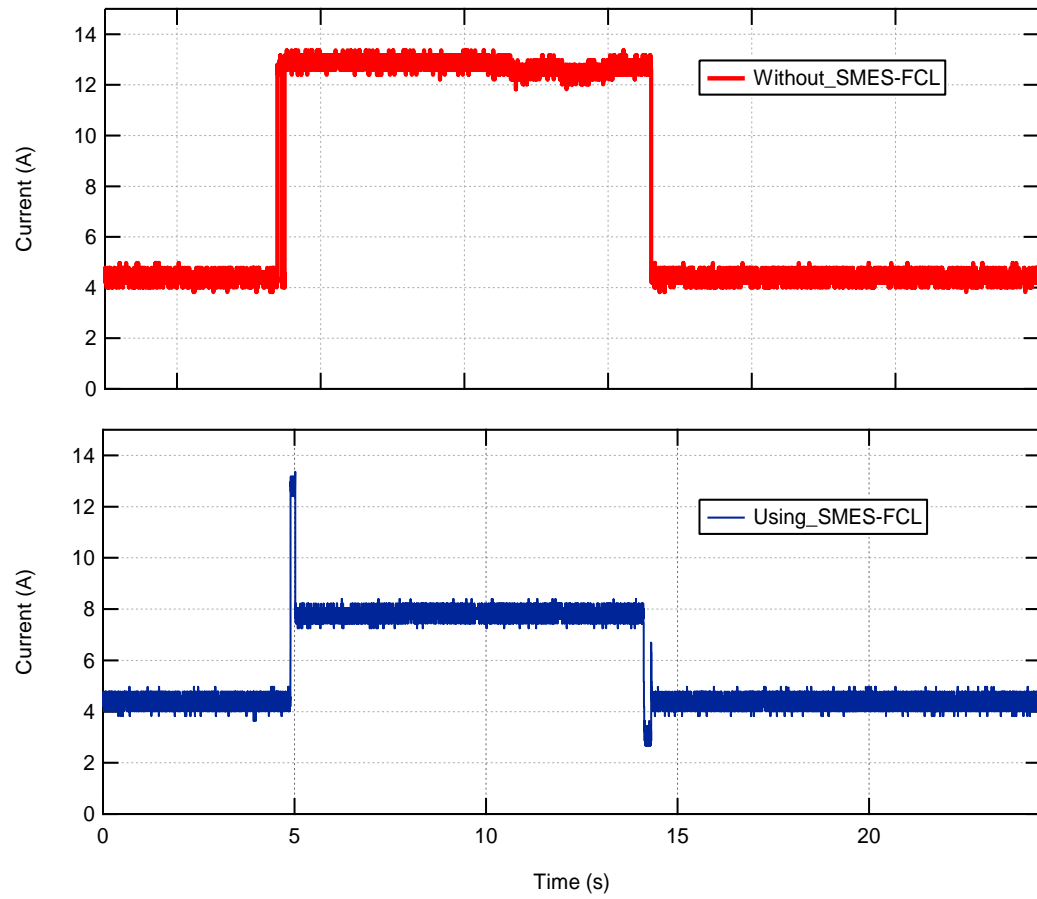


Figure 5-17 DC-line current during the current-limitation test

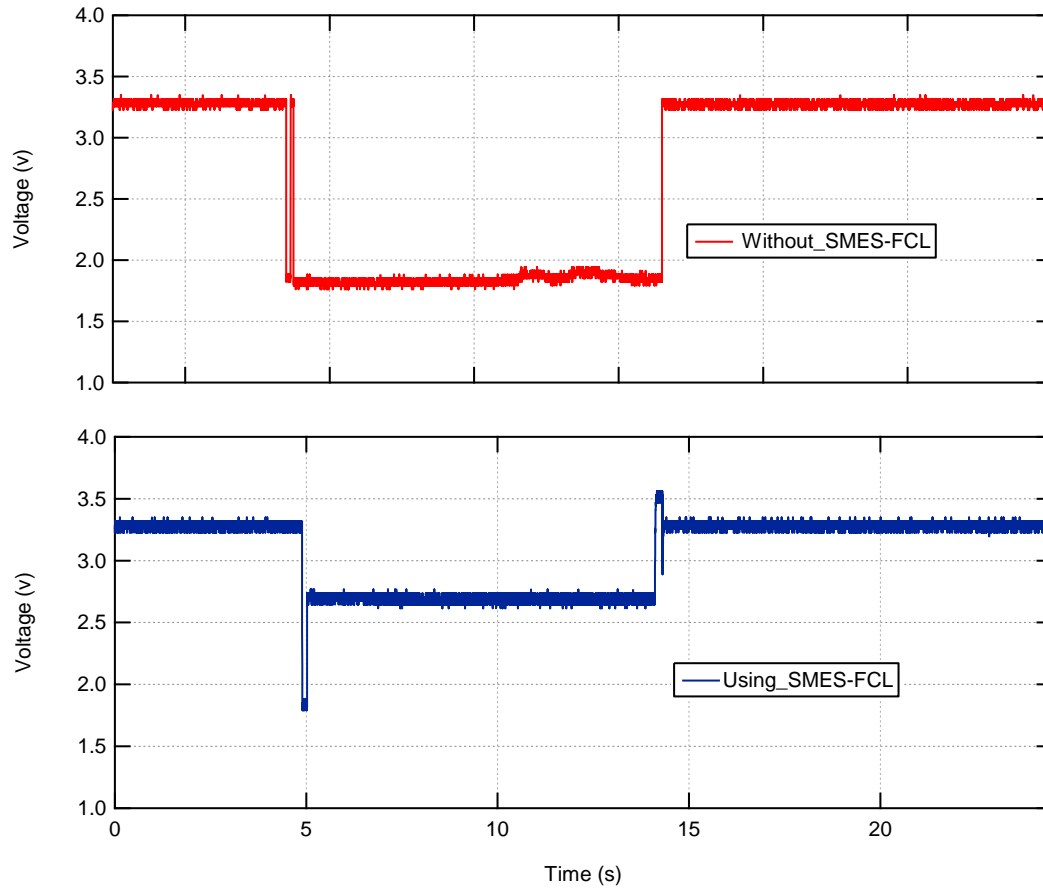


Figure 5-18 Connection-point voltage during the current-limitation test

5.6 Application of the DC SMES-FCL in a DFIG-DC system

This section investigates the effect of using SMES-FCL in a DC system connected to a DFIG-based wind turbine generator. It starts with an introduction to the connection of DFIGs to DC systems, including a brief review of the current literature. There follows a description of the system used in this study, and the connection of the generator and the SMES-FCL to the DC line is illustrated. After that, the control proposed for the DFIG-DC system is explained. Finally, the results of the system's behaviour under different fault conditions and with different coil parameters are reported and discussed.

5.6.1 Introduction to DFIG-DC systems

Due to the many outstanding features of DFIGs, many wind turbines incorporate one to form a variable-speed-based generator. This confers several advantages in comparison to other types of wind turbine generators, which can be summarized as:

- The active and reactive power outputs can be controlled independently
- The shaft speed has a wider range; it can be up to 30% below or above the rated speed for which generation can take place
- The ability to extract the maximum power from the wind
- The ability to limit output power during high wind speeds
- The ability to be controlled to reduce mechanical stresses.

The conventional connection of DFIG-based wind turbines to AC grids depends on using a partially rated back-to-back converter to achieve decoupled control of the active and reactive power output. The result is a normal induction generator with the stator connected directly to the grid and the rotor connected to the grid via the power converter. Control of the generator can be achieved through the stator-side and rotor-side converters, which are partially rated to about 30% of the rated power of the generator. Figure 5-19 illustrates the connection of the DFIG to the AC grid via the converter.

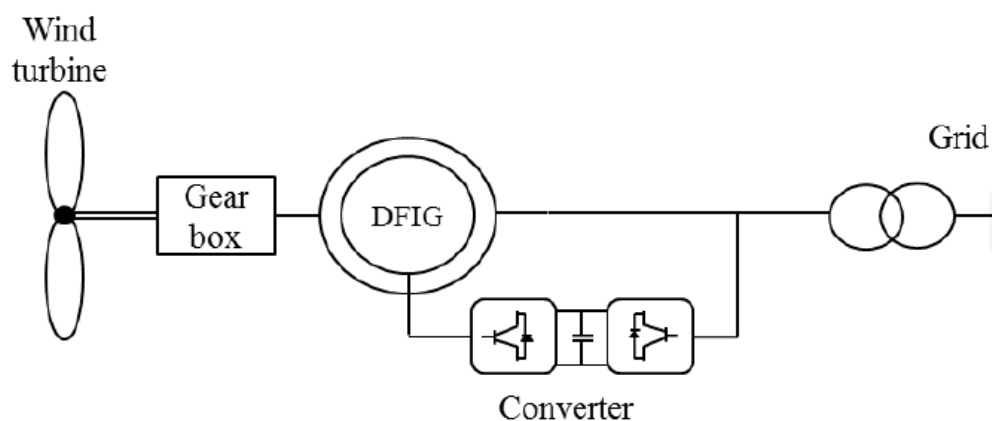


Figure 5-19 Conventional connection of a DFIG to an AC system

Due to their many outstanding features, DFIG-based wind turbines have been investigated for connection to DC grids either in stand-alone or AC-grid-connected modes [140] [141]. One system proposed in these researches is to connect the stator side of the generator to the DC bus by a controlled stator-side converter, while the rotor is connected to the same DC bus using a controlled rotor-side converter. The DC bus is then connected to the high-voltage DC line by another DC-to-DC converter. This method guarantees full control of the generation and has good stability but at increased system cost and complexity. Another method of DFIG-to-DC connection, which uses a more common topology, depends on using an uncontrolled power converter to connect the stator to the DC bus while connecting the rotor to the same bus using a rotor-side converter [142]. This topology benefits from using a partially rated converter and gives full control of the voltage and frequency of the generator. However, torque ripples and stator current harmonics appear due to the commutation of the stator diode rectifier. These problems have been solved by various control techniques [143] [144] [145]. In addition, a new control scheme has been tested that is based on resonance and PI controllers to reduce the torque ripples [10]. To reduce the current harmonics, direct control of the sinusoidal stator currents without using voltage sensors has been described and tested experimentally [11].

Despite the outstanding advantages of DFIG-based wind turbines, the high currents induced in the stator and rotor during system disturbances may destroy the converter. The solution of disconnecting the generator from the grid during disturbances is not applicable in stand-alone grids because it may affect the loads directly. Even in grid-connected mode, a loss of high-power generation will affect system stability.

5.6.2 System description

The system under test consists of a DFIG-based wind turbine generator. The stator is connected to a three-phase diode rectifier and then to the DC line, while the rotor is connected to a voltage-source converter and then to the DC line. The DC system is connected to an AC grid to simulate the grid-connected mode. The AC grid model used is from the MATLAB/Simulink library. Figure 5-20 shows a circuit diagram for the system.

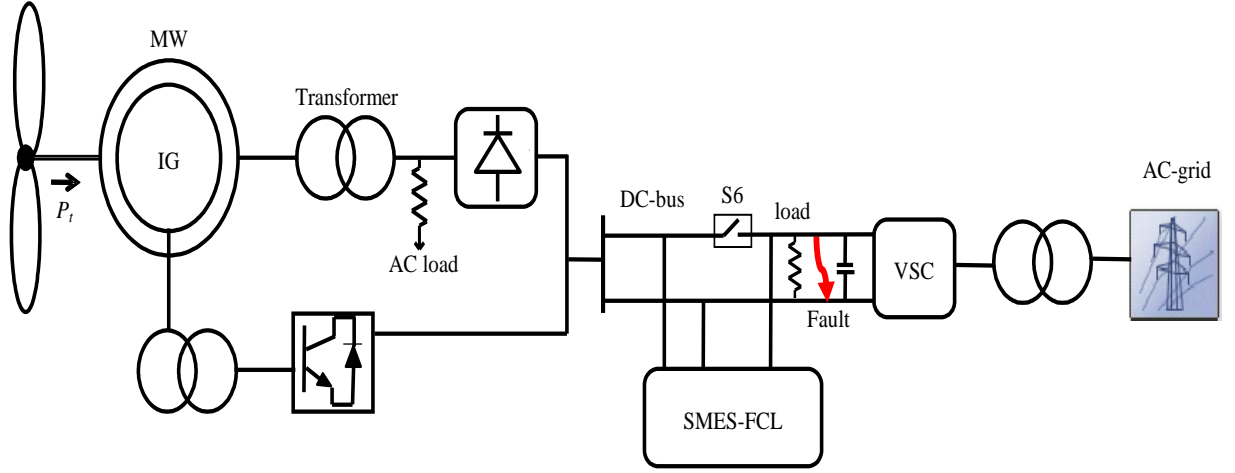


Figure 5-20 System configuration for SMES-FCL connection to a DFIG-DC system

The wind turbine generator has a power rating of 0.3 MW and voltage of 575 V. A 0.1 MW AC load is connected to the AC side while the DC load is represented by a 10 Ω resistor connected to the DC line, as shown in Figure 5-20. The parameters of the SMES-FCL system are based on the required energy storage and fault-limitation settings. The rated delivered power to the DC line is 0.2 MW assuming fully rated generation of 0.3 MW and an AC load absorption of 0.1 MW. To supply the DC load at full power for 0.5 s, we need a 0.2 MJ coil. The operating current of the SMES is chosen on the basis of the current in the main DC line. The initial value of the SMES current is 120 A and the value that activates the fault-current-limitation mode (I_{set}) is 300 A, which is 50 A below the critical current to ensure that the main SMES coil won't be quenched. By using the following equation for energy storage, the inductance of the SC coil can be calculated:

$$E = \frac{1}{2} L I_{smes}^2 \quad (5-1)$$

The inductance of the coil used in this system is 5 H. The tape used in this coil is assumed to be of YBCO material because it has better characteristics than other HTS materials [146]. With a copper stabilizer of 40 μm thickness and 4 mm width, the resistance of the tape at room temperature is 0.12 Ω/m [147]. A current-limitation resistance of 5 Ω is calculated to be suitable for the system under study. Thus, a total length of 40 m is required for the fault-current-limiting pancakes, with the resulting inductance being based on the winding configuration, which is assumed as 50 mH for this study.

5.6.3 Control of DC-DFIG

A conventional connection of DFIG-based wind turbines to AC grids depends on using a partially rated back-to-back converter to achieve decoupled control of the active and reactive power. The stator is directly connected to the AC grid while the rotor is connected to the grid using the power converter [148]. However, integration of DFIG-based wind turbines to DC grids has been proposed in the literature with different connection schemes [149] [150]. The topology used in this paper connects the stator windings to the DC bus using a three-phase diode bridge, and the rotor is also connected to the DC bus, via a voltage-source converter [142] [151]. The stator voltage and frequency are controlled using the rotor currents. A brief explanation of this DFIG-DC system follows.

The voltage equations for the generator in the d - q reference frame are given as:

$$v_{ds} = R_s i_{ds} - \omega_s \lambda_{qs} + \frac{d\lambda_{ds}}{dt} \quad (5-2)$$

$$v_{qs} = R_s i_{qs} + \omega_s \lambda_{ds} + \frac{d\lambda_{qs}}{dt} \quad (5-3)$$

$$v_{dr} = R_r i_{dr} - (\omega_s - \omega_r) \lambda_{qr} + \frac{d\lambda_{dr}}{dt} \quad (5-4)$$

$$v_{qr} = R_r i_{qr} + (\omega_s - \omega_r) \lambda_{dr} + \frac{d\lambda_{qr}}{dt} \quad (5-5)$$

where λ is the flux linkage, ω is the angular frequency, R is the resistance per phase, and s and r subscripts refer to stator and rotor, respectively. The flux linkage equations can be written as:

$$\lambda_{ds} = L_s i_{ds} + L_m i_{dr} \quad (5-6)$$

$$\lambda_{qs} = L_s i_{qs} + L_m i_{qr} \quad (5-7)$$

$$\lambda_{dr} = L_m i_{ds} + L_r i_{dr} \quad (5-8)$$

$$\lambda_{qr} = L_m i_{qs} + L_r i_{qr} \quad (5-9)$$

Choosing the synchronous rotating d - q reference frame results in alignment of the stator flux on the d -axis, while its component on the q -axis is set to zero. Thus, the d - q stator currents can be written as:

$$i_{ds} = \frac{(\lambda_{ds} - L_m i_{dr})}{L_s} \quad (5-10)$$

$$i_{qs} = (-L_m i_{qr})/L_s \quad (5-11)$$

Simple vector control is used to adjust the active and reactive control loops [140]. The q -axis rotor current is used to control the frequency of the stator, while the d -axis rotor current is used to control the DC voltage.

Figure 5-21 summarizes the control of the rotor-side converter. As shown in this figure, two PI loops are used to estimate each of the direct and quadrature reference voltages of the rotor. Then, they are transferred to (abc) frame again to produce the gate signals for the rotor-side converter. A phase-locked loop is used to align the stator voltages to the correct phase.

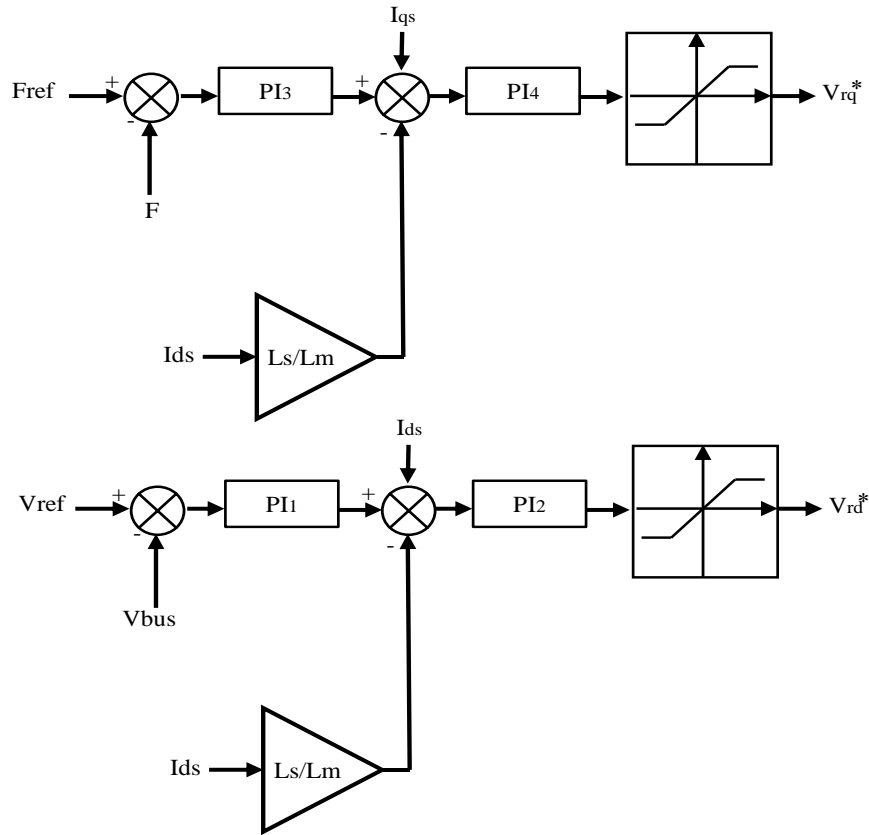


Figure 5-21 Control of the VSC in a DFIG-DC system

5.6.4 Results and discussion

The DFIG-DC system is assumed to be a microgrid that can be operated either stand-alone to supply the DC load, or in connected mode to the AC grid. These two cases are simulated and the performance of the SMES-FCL system is investigated in various scenarios. The results are divided into two: the first set is for the stand-alone mode, which includes three scenarios, and the second set is for the connected mode, which involves two further scenarios.

5.6.4.1 Stand-alone mode

To start with, the DC system is isolated from the AC grid and the generator supplies the load. The first scenario represents the normal operational mode with variable wind-speed operation. With the variable wind speed, the power delivered to the load will not be smooth. This scenario is used to investigate the ability of the SMES-FCL to smooth the output power of a wind generator in a DC grid. Figure 5-22 shows the power delivered to the DC load with and without the SMES-FCL system. It is clear that SMES-FCL is able to eliminate fluctuations in the power by charging and discharging: as illustrated in Figure 5-23, the current in the SMES coil increases when the generated power is above the reference value and decreases to discharge and support the load with the necessary power when that generated falls below the reference value.

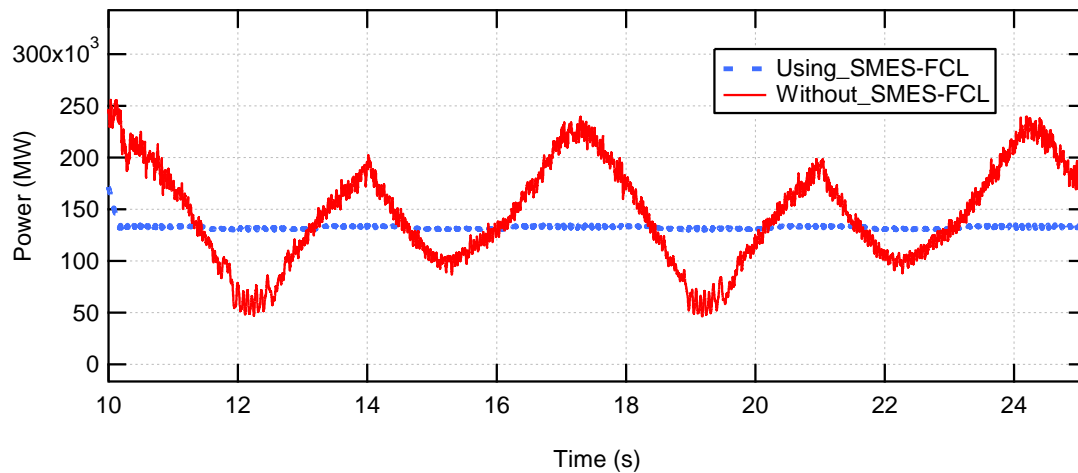


Figure 5-22 Load power with and without SMES-FCL with variable-speed operation

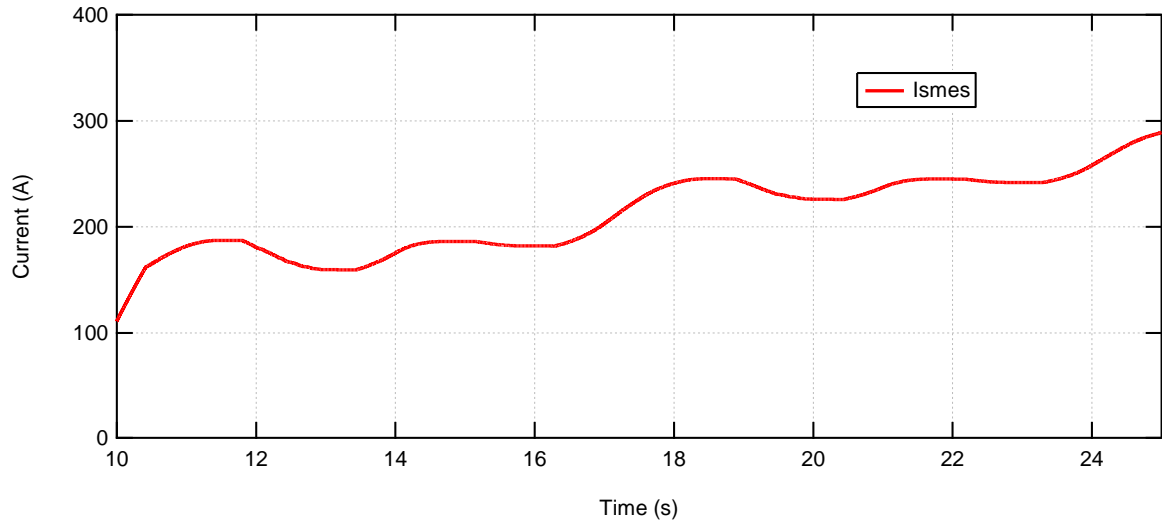


Figure 5-23 SMES current with variable wind-speed operation

The second scenario in the stand-alone mode covers compensation for a voltage drop at the load side. A drop in the generator side is applied after 15 seconds for 100 ms. The voltage and the current of the load during the voltage drop with and without SMES-FCL are monitored. As can be seen in Figure 5-24, the SMES coil can compensate for the voltage drop at the generator terminals and support the load with the full normal voltage. The current of the load is shown in Figure 5-25 where it can be seen that the SMES coil supplies the load with the required current almost instantly following the start of the voltage drop. The current in the SMES in this scenario is shown in Figure 5-26. Although these scenarios of wind farm generation and SMES systems have been studied before, they are studied here to investigate the performance of the SMES-FCL system as an energy storage device because this is the primary function of the proposed system. The fault-current-limiter element has no effect on the system in these two scenarios.

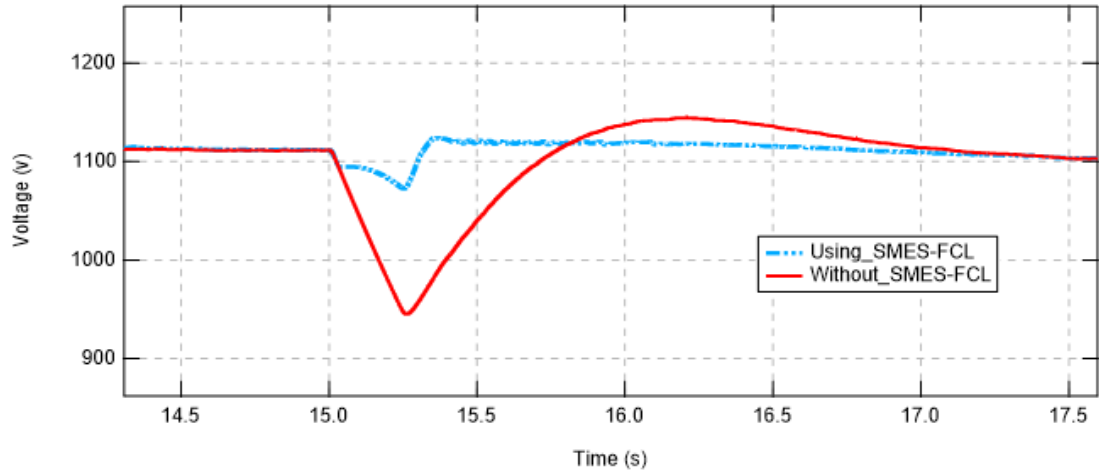


Figure 5-24 Load voltage with and without SMES-FCL during voltage-drop scenario

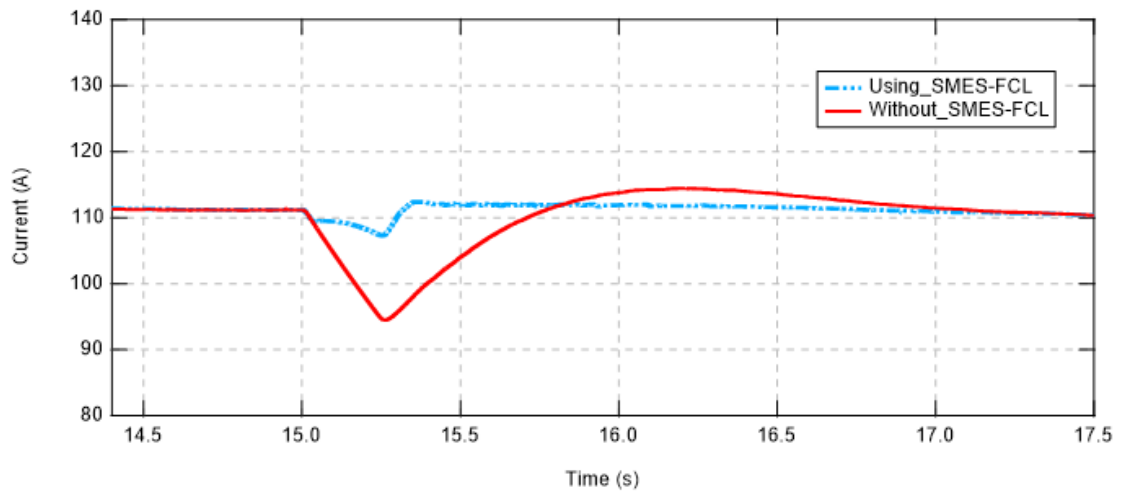


Figure 5-25 Load current with and without SMES-FCL during voltage-drop scenario

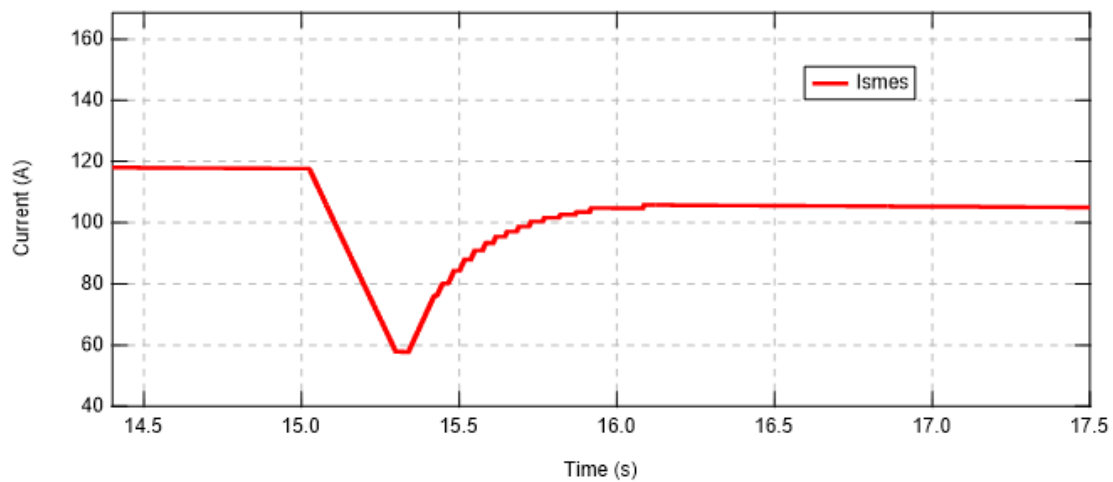


Figure 5-26 SMES current during voltage-drop scenario

The third scenario studied here is the application of a DC fault and the limitation effect of the SMES-FCL. The effect of using the SMES-FCL is compared with the use of SMES alone and not using either device. Figure 5-27 illustrates the DC-line current during application of a DC fault at the end of the DC line for 100 ms starting after 16 seconds. The prospective current increased to more than 1,200 A at the start of the fault and then dropped to zero and did not resume its pre-fault value until five seconds after the fault occurred. Using SMES alone has a very small effect on the peak fault limitation, as shown in Figure 5-27. It limits the peak of the fault current to less than 1,100 A, which corresponds to a limitation to 90% of the prospective fault value. However, the SMES helps the system resume its pre-fault current value within two seconds of the fault occurring. With SMES-FCL, the peak current is limited to 300 A, which corresponds to 25% of its prospective value. In this case, the current did not drop to zero and the SMES element again helps the system to resume its pre-fault value within two seconds.

The DC voltage at the generation side is illustrated in Figure 5-28. The prospective voltage dropped to zero before taking four seconds to return to its pre-fault value. The SMES-only case shows enhancement in the time taken to resume stability. With SMES-FCL, the voltage was 580 V at the start of the fault and this increased to 780 V during the remainder of the fault period. These values correspond to 0.5 pu and ~0.6 pu, respectively. Comparing these values to the grid code examples shown in **Error! Reference source not found.** [12] indicates that the generator can support the system during the fault and that

the wind turbine generator will not be tripped during the fault. On the other hand, according to some grid codes, the prospective voltage-drop value may cause the generator to trip during the fault period. The generated DC power is shown in Figure 5-. It is clear that the power follows the voltage behaviour. The generator speed is shown in Figure 5-. Using the SMES system helps the generator to restore its mechanical stability faster, as shown in this figure. In addition, adding the fault-current-limiting function to the SMES system reduces the increase in the generator speed during the fault period: without either device the speed reached 1.7 pu, but this value was reduced using SMES alone to 1.5 pu, and SMES-FCL reduced it further, to 1.42 pu.

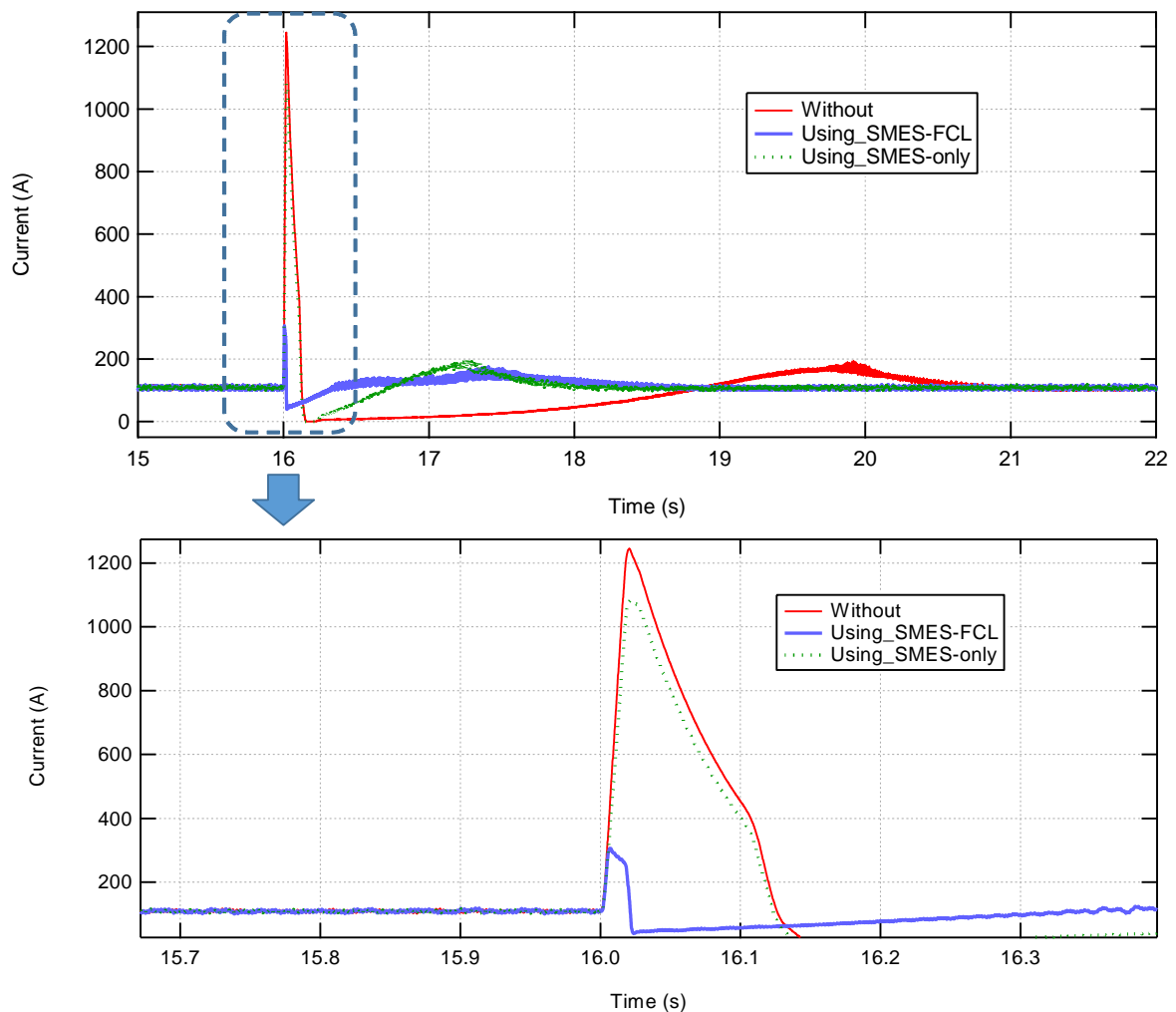


Figure 5-27 DC current with and without SMES-FCL and with SMES only in stand-alone mode during DC fault (the lower figure represents a detailed inset of the upper figure)

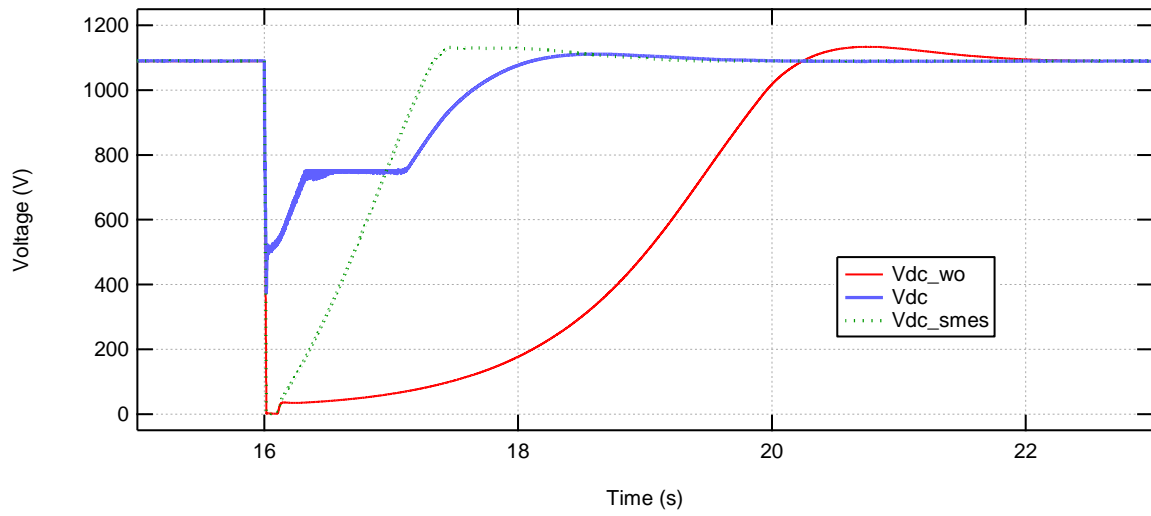


Figure 5-28 DC voltage with and without SMES-FCL and with SMES only during DC fault in stand-alone mode

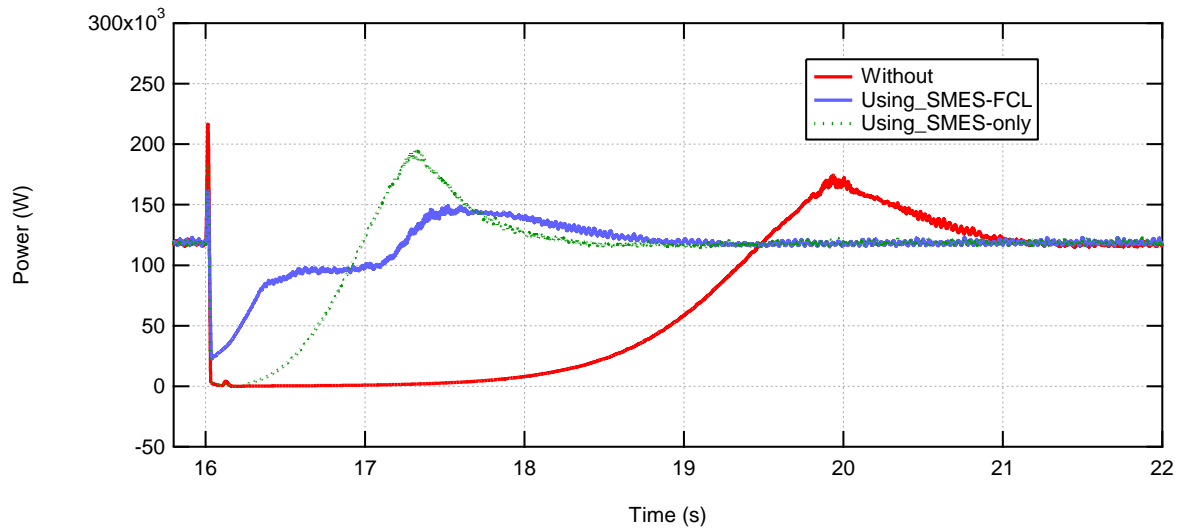


Figure 5-29 Generated DC power with and without SMES-FCL and with SMES only during DC fault in stand-alone mode

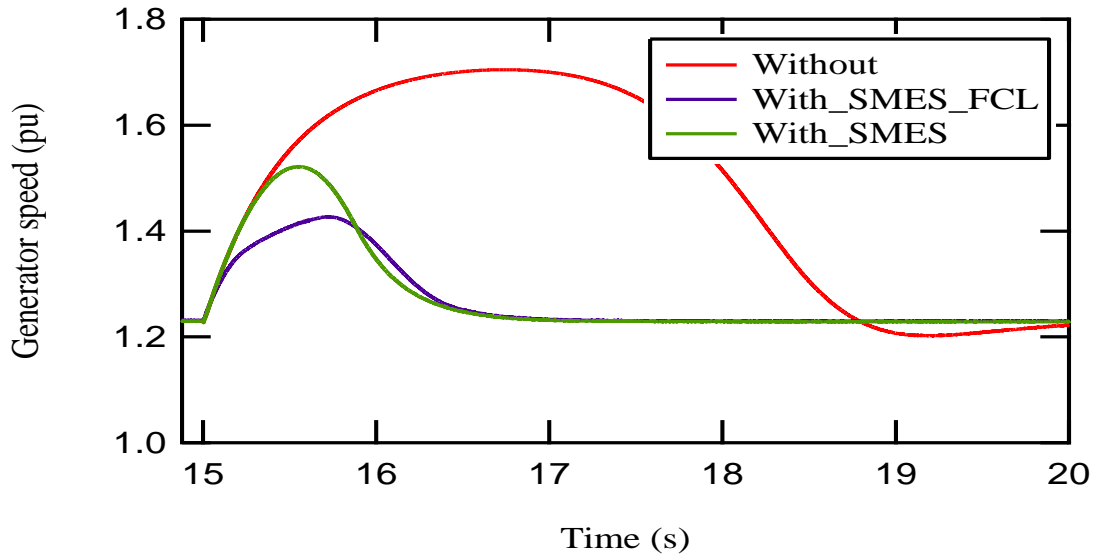


Figure 5-30 Generator speed with and without SMES-FCL and with SMES only during DC fault in stand-alone mode

5.6.4.2 Grid-connected mode

The second mode is the grid-connected mode in which the DC system is connected to an AC grid. Two scenarios are studied in this case. The first involves a DC fault and the second involves a three-phase-to-ground fault on the AC grid. The limitation of the DC current and the voltage profile on the generation side are monitored.

The DC fault is applied after 12 seconds and lasts for 100 ms. Figure 5- illustrates the DC currents in this scenario; SMES-FCL limits the current from 1400 A to 500 A, which corresponds to a 64% limitation. The DC voltage is shown in Figure 5-. The drop in voltage reaches zero during the fault and there is an increase in the voltage of 1800 V following fault clearance. Without SMES-FCL, the DC voltage fails to return to its pre-fault value. However, SMES-FCL helps the voltage to return to its pre-fault value in less than one second.

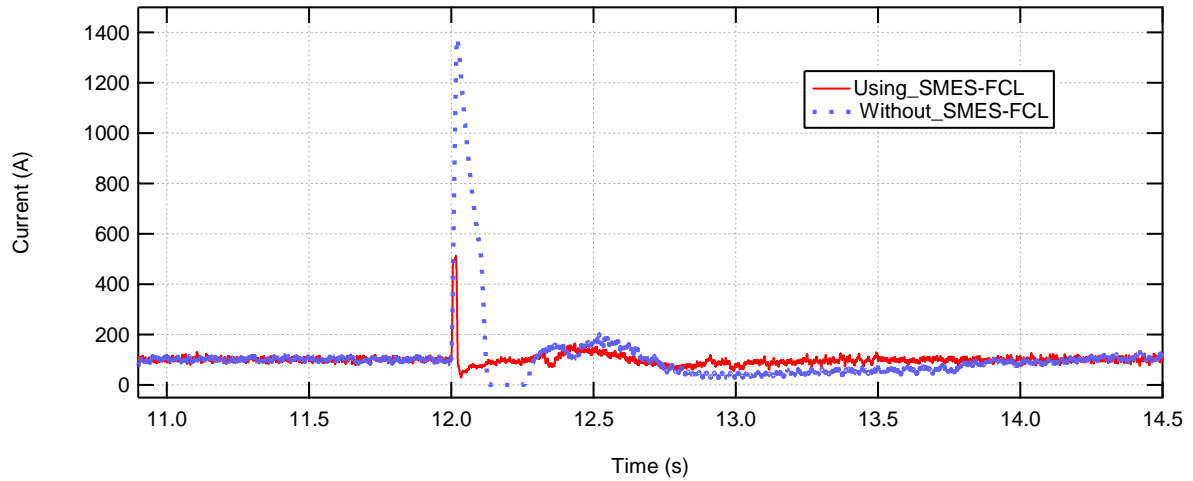


Figure 5-29 DC currents with and without SMES-FCL in case of DC fault in grid-connected mode

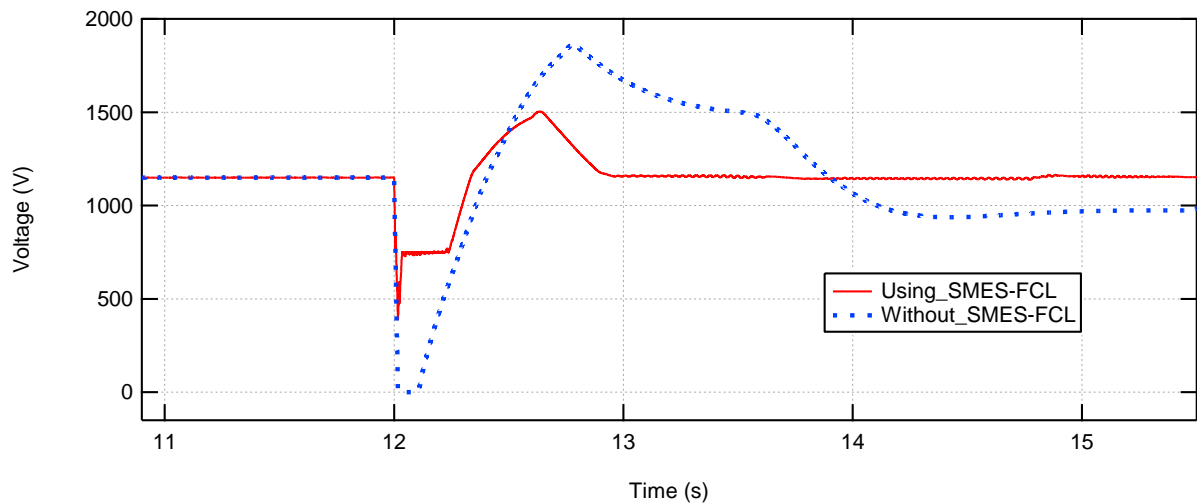


Figure 5-30 Generator-side DC voltage with and without SMES-FCL in case of DC fault in grid-connected mode

The second scenario in the grid-connected mode involves application of an AC fault to the AC grid. Because the major feed to the fault in this scenario derives from the AC grid, the increase in the current in the DC line is not severe. However, the voltage profile and the current are disturbed by the fault. In this scenario, the current-limiting part of the SMES-FCL system plays no role. The SMES system alone helps the system to restore stability after the fault. As shown in Figure 5-, the first peak in the current only reaches ~180 A, which is less than the critical current of the current-limitation system. The current

waveform exhibits a small disturbance after the fault, which is minimized by the use of SMES-FCL.

The DC voltage waveform is shown in Figure 5-, where it is clear that the AC fault causes the voltage to become unstable after the fault. Using SMES-FCL returned the voltage to its pre-fault value within one second of fault clearance.

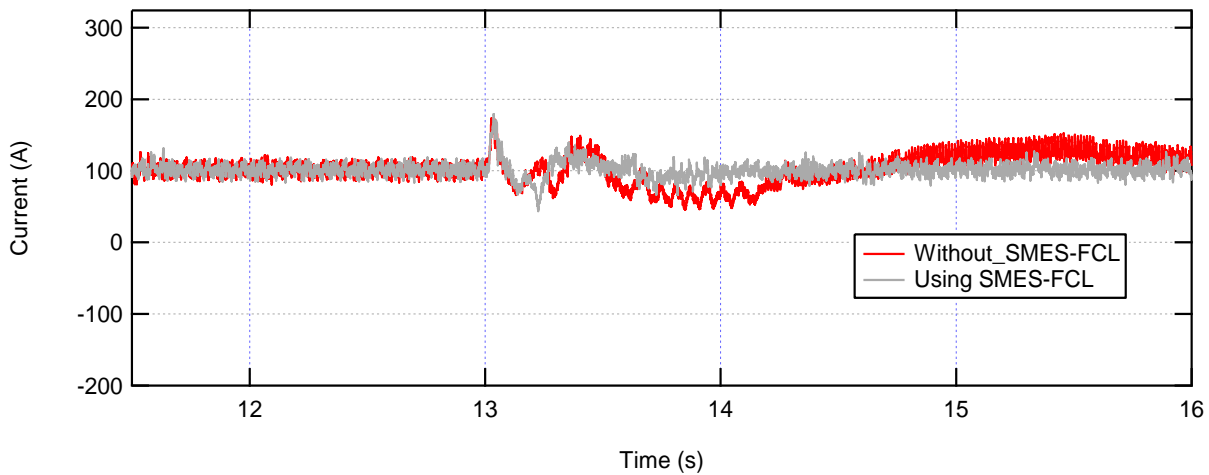


Figure 5-33 DC-line current with and without SMES-FCL during AC fault in grid-connected mode

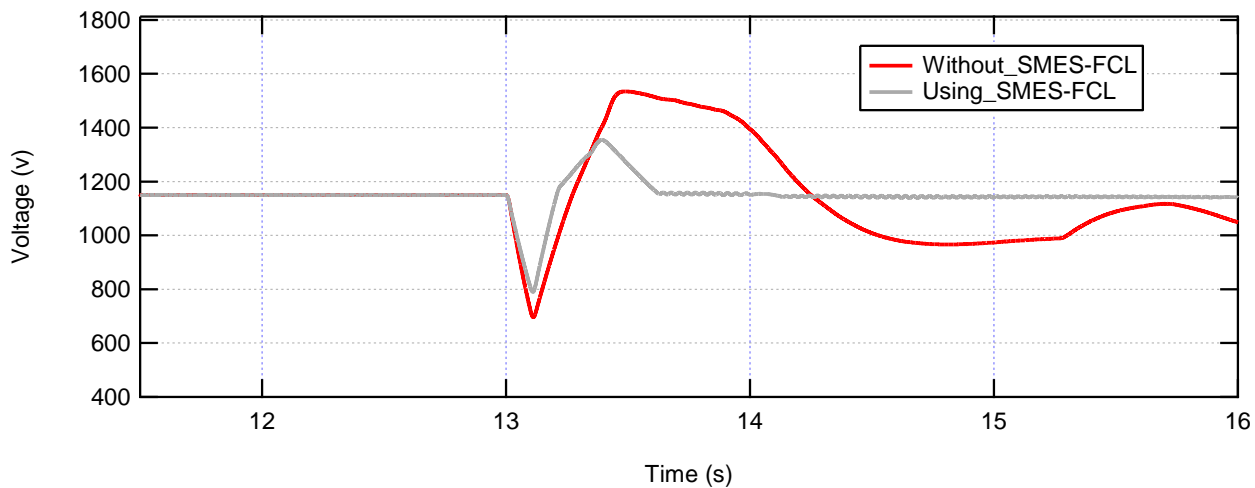


Figure 5-34 DC voltage with and without SMES-FCL during AC fault in grid-connected mode

5.7 Summary

This chapter proposed a new technique for using an SMES system to limit high fault currents in DC systems. The proposed system proved effective as an energy storage device in a simple DC system, which was tested in a simulation program and a small-scale laboratory prototype. It was also investigated in the context of limiting fault currents and the results showed good current limitation based on the parameters chosen for the system. However, the SMES-FCL system requires high-speed switches in order to limit the fault current from the outset (i.e. the first peak).

The proposed SMES-FCL device was also investigated in a wind energy-based DC system that relied on a DFIG turbine. The SMES-FCL effectively smoothed the generator output power, compensated for a voltage drop at the generator side, and supported the load with the required power. It also limited the fault current in different scenarios and connection modes and supported system stability following faults.

Chapter 6

Conclusions and future work

The aim of this thesis was to improve the integration of wind energy systems into the power grid. Because wind energy has many advantages over other types of energy generation, connecting more wind farms into electrical grids helps to address increasing power demand. However, the intermittent nature of wind energy and sensitivity to grid disturbances are two major challenges for grid operators in this integration. There are several different types of wind turbine generators and a variety of connection methods. Each type and connection has its own advantages and challenges. Two types of wind turbine generators are used in this study and three different power systems considered. The thesis focused on the intermittent nature of wind generation and the fault ride-through capability of wind farm systems.

On a separate front, superconductivity technology has evolved rapidly in recent decades. Superconducting devices have proved effective in solving some problems associated with wind energy integration. However, cost is still a significant issue in developing superconducting devices for large-scale applications. To mitigate this cost issue, multifunctional superconducting devices have been proposed in this thesis.

The first device proposed in this thesis is the superconducting fault-current-limiting transformer (SFCLT), considered in Chapter 3. The idea of integrating the current-limiting function had already been raised in previous research. However, the contribution of this thesis is the development of a model in PSCAD software for a 100 MVA transformer with both primary and secondary windings formed from superconducting materials. The model allowed consideration of the thermal and electrical behaviour of the superconducting material. Thus, the temperature of the windings, which is considered a very important factor in determining transformer performance during faults, can be monitored using the model. The parameters of the transformer can be changed in the model to allow multiple studies on different power system structures. The SFCLT model was investigated as a replacement for a conventional 100 MVA transformer in a wind energy-based power system derived from existing literature.

The effect of the SFCLT on system performance during different fault scenarios was investigated. Because fault currents change according to the location of a fault, two different fault locations were studied. In addition, different fault types were simulated, and current limitation and windings temperature were monitored. The results proved the effectiveness of the SFCLT in limiting fault currents in all scenarios from the first cycle onwards through the entire fault period.

The second device proposed in this thesis is the superconducting magnetic energy storage fault-current limiter (SMES-FCL). To tackle the problem of the variable output power from wind farms that affects the stability of grids, SMES systems have been employed in the literature to smooth the output power. In addition, fault-current limiters have been introduced to limit the fault currents of wind farms. However, instead of using two separate superconducting devices, the fault-current-limitation function is inserted into the SMES system via a new technique to save on cost, space and refrigeration effort. The entire SMES coil is used in the energy storage function, while only part of it is used as a superconducting fault-current limiter. This technique has not been presented in any previous research, and it is adaptable to any power system. The number of pancakes used to limit the fault current, as well as the control sequence, can be changed to fit with different power system requirements.

A SMES-FCL was used with an AC system dependent on a squirrel-cage induction generator-based wind turbine. The system was designed and built using PSCAD software. The SMES-FCL was connected to the system using a three-windings transformer. During normal operation, the variable wind speed causes the output power of the wind turbine generator to fluctuate. The SMES-FCL can effectively smooth the output power delivered to the load in this system. In addition, a 0.5 pu voltage drop is simulated at the generator terminals, and the SMES-FCL was able to compensate for this voltage drop instantly. After proving the energy storage function, the SMES-FCL was tested for its ability to limit fault currents. To prove its effectiveness, different fault conditions were applied to the system and a focus placed on the generator currents and voltages. The SMES-FCL could limit the fault currents in all test cases from the first cycle onwards. Using a SMES system on its own improves the performance of the system following the fault period, but has no effect on current limitation or system performance during the fault. However, SMES-FCL helped the generator to remain connected to the system during the fault and to restore normal operation shortly after fault clearance.

The third part of the thesis is the development of a DC-based SMES-FCL system. The contribution of this section can be represented in the proposed system itself, the investigation of the system, and its application to a doubly-fed induction generator (DFIG)-based wind turbine system in a DC system. The basic idea is the same as that of the AC-based SMES-FCL, but the system configuration and the control sequence are different. The DC SMES-FCL system was built in MATLAB/Simulink and tested as a fault-current limiter and energy storage device. The simulation model was used to choose suitable parameters, and the system was then built in the lab and controlled using a DAQ and the LabView interface. The energy storage function and the current limitation were tested. The proposed system and its control proved effective operationally in both storing energy and limiting high currents in the main system.

A DFIG-based wind turbine was also chosen as the main generation unit in the third power system studied. The DFIG is connected to a DC line and then to the AC grid. The control of the rotor-side converter was developed while the stator was connected to the DC line by an uncontrolled rectifier. Starting with stand-alone normal operation, different cases were studied with variable speed, voltage-drop compensation and DC faults. The SMES-FCL smoothed the output power and also effectively compensated for voltage drops at the load side. In terms of current limitation, the SMES-FCL could limit the faults to low values depending on the value of the critical current involved. Fault currents were also limited in grid-connected mode and the system was restored to stability faster following fault clearance. Even with an AC fault in the AC grid, where the current did not increase to high values because the AC grid was the main feeder to the fault, the SMES-FCL still helped the system to restore stability faster than without it.

In brief, integrating the fault-current-limiting function into superconducting devices provided good performance and could be a strong candidate for pushing the use of superconducting technology to improve and increase wind power integration into both AC and DC grids.

The main benefit of limiting the fault current is the reduction of short-circuit levels. With more sources integrated into grids the short-circuit levels may increase to values beyond the existing circuit-breaker ratings. Fault-current limiting devices can be used to reduce fault values such that existing circuit breakers can cope without being upgraded. They are

also a good backup in the case of circuit-breaker failure in protecting wind turbine generators from high fault currents within a few milliseconds.

Future work in relation to the multifunctional superconducting devices proposed here might include:

- Further study of the mechanical stresses that might affect superconducting materials handling high fault currents
- Study of the most appropriate types of switches to avoid failure of a SMES-FCL system when dealing with high currents.
- Further research into reducing power electronic switch losses, especially in cryogenic systems, given that these switches cause most loss in an SMES-FCL system
- Research into hybrid energy storage systems that incorporate SMES with other energy storage mechanisms and can be used with the fault-current-limitation function to achieve SMES-related size reductions and better overall performance
- Development of better coordination between the SMES-FCL and protection systems to achieve further enhancement of system performance during faults and decrease the circuit-breaker requirements.

References

- [1] A. Growth, “Ren21 renewables 2018 global status report.”
- [2] T. Ackermann *et al.*, *Wind power in power systems*. Wiley Online Library, 2005, vol. 140.
- [3] “Wind energy generates £1.25bn for UK economy, provides 30,000 jobs,” <https://www.edie.net/news/6/UK-invested-1-25bn-into-wind-energy-last-year/>, accessed: 2015-10-06.
- [4] A. E. Leon, M. F. Farias, P. E. Battaiotto, J. A. Solsona, and M. I. Valla, “Control strategy of a DVR to improve stability in wind farms using squirrel-cage induction generators,” *IEEE Transactions on power systems*, vol. 26, no. 3, pp. 1609–1617, 2010.
- [5] M. H. Zamani, S. H. Fathi, G. Riahy, M. Abedi, and N. Abdolghani, “Improving transient stability of grid-connected squirrel-cage induction generators by plugging mode operation,” *IEEE Transactions on Energy conversion*, vol. 27, no. 3, pp. 707–714, 2012.
- [6] I. Munteanu, A. I. Bratcu, N.-A. Cutululis, and E. Ceanga, *Optimal control of wind energy systems: towards a global approach*. Springer Science & Business Media, 2008.
- [7] D. Bang, H. Polinder, G. Shrestha, and J. A. Ferreira, “Review of generator systems for direct-drive wind turbines,” in *European wind energy conference & exhibition, Belgium*, vol. 31, 2008.
- [8] S. kumar Bisoyi, R. Jarial, and R. Gupta, “A review of the state of the art of generators and power electronics converter topologies for wind energy conversion system,” *International Journal of Emerging Technology and Advanced Engineering*, vol. 3, no. 3, pp. 283–291, 2013.
- [9] O. J. Petinrin and M. Shaaban, “Overcoming challenges of renewable energy on future smart grid,” *TELKOMNIKA Indonesian Journal of Electrical Engineering*, vol. 10, no. 2, pp. 229–234, 2012.
- [10] D. Eltigani and S. Masri, “Challenges of integrating renewable energy sources to smart grids: A review,” *Renewable and Sustainable Energy Reviews*, vol. 52, pp. 770–780, 2015.
- [11] M. Molinas, J. A. Suul, and T. Undeland, “Low voltage ride through of wind farms with cage generators: STATCOM versus SVC,” *IEEE Transactions on power electronics*, vol. 23, no. 3, pp. 1104–1117, 2008.
- [12] M. Tsili and S. Papathanassiou, “A review of grid code technical requirements for wind farms,” *IET Renewable power generation*, vol. 3, no. 3, pp. 308–332, 2009.

- [13] M. P. Palsson, T. Toftevaag, K. Uhlen, and J. O. G. Tande, "Large-scale wind power integration and voltage stability limits in regional networks," in *IEEE Power Engineering Society Summer Meeting*, vol. 2. IEEE, 2002, pp. 762–769.
- [14] A. Arulampalam, M. Barnes, N. Jenkins, and J. B. Ekanayake, "Power quality and stability improvement of a wind farm using STATCOM supported with hybrid battery energy storage," *IEE Proceedings-Generation, Transmission and Distribution*, vol. 153, no. 6, pp. 701–710, 2006.
- [15] L. Xu, L. Yao, and C. Sasse, "Comparison of using SVC and STATCOM for wind farm integration," in *2006 International Conference on Power System Technology*. IEEE, 2006, pp. 1–7.
- [16] J. Conroy and R. Watson, "Low-voltage ride-through of a full converter wind turbine with permanent magnet generator," *IET Renewable power generation*, vol. 1, no. 3, pp. 182–189, 2007.
- [17] G. Pannell, D. J. Atkinson, and B. Zahawi, "Minimum-threshold crowbar for a fault-ride-through grid-code-compliant DFIG wind turbine," *IEEE Transactions on Energy Conversion*, vol. 25, no. 3, pp. 750–759, 2010.
- [18] K. E. Okedu, S. Muyeen, R. Takahashi, and J. Tamura, "Wind farms fault ride through using DFIG with new protection scheme," *IEEE transactions on sustainable energy*, vol. 3, no. 2, pp. 242–254, 2012.
- [19] A. O. Ibrahim, T. H. Nguyen, D.-C. Lee, and S.-C. Kim, "A fault ride-through technique of DFIG wind turbine systems using dynamic voltage restorers," *IEEE transactions on energy conversion*, vol. 26, no. 3, pp. 871–882, 2011.
- [20] K.-H. Kim, Y.-C. Jeung, D.-C. Lee, and H.-G. Kim, "Lvrt scheme of PMSG wind power systems based on feedback linearization," *IEEE transactions on power electronics*, vol. 27, no. 5, pp. 2376–2384, 2011.
- [21] H. Geng, C. Liu, and G. Yang, "LVRT capability of DFIG-based WECS under asymmetrical grid fault condition," *IEEE transactions on Industrial electronics*, vol. 60, no. 6, pp. 2495–2509, 2012.
- [22] M. N. Wilson, "100 years of superconductivity and 50 years of superconducting magnets," *IEEE transactions on applied superconductivity*, vol. 22, no. 3, pp. 3 800 212–3 800 212, 2011.
- [23] J. W. Bray, "Superconductors in applications; some practical aspects," *IEEE Transactions on Applied Superconductivity*, vol. 19, no. 3, pp. 2533–2539, 2009.
- [24] Z. Zhang, "Electrical characterizing of superconducting power cable consisted of second-generation high-temperature superconducting tapes," 2016.

- [25] M. Tinkham, *Introduction to superconductivity*. Courier Corporation, 2004.
- [26] J. Hirsch, M. Maple, and F. Marsiglio, “Superconducting materials classes: Introduction and overview,” 2015.
- [27] J. G. Bednorz and K. A. Müller, “Possible high t_c superconductivity in the Ba- La- Cu- O system,” *Zeitschrift für Physik B Condensed Matter*, vol. 64, no. 2, pp. 189–193, 1986.
- [28] J. Hernandez-Llambes and D. Hazelton, “Advantages of second-generation high temperature superconductors for pulsed power applications,” in *2009 IEEE Pulsed Power Conference*. IEEE, 2009, pp. 221–226.
- [29] P. Tixador, G. Donnier-Valentin, and E. Maher, “Design and construction of a 41 kVA Bi/Y transformer,” *IEEE transactions on applied superconductivity*, vol. 13, no. 2, pp. 2331–2336, 2003.
- [30] T. Masuda, H. Yumura, M. Watanabe, H. Takigawa, Y. Ashibe, C. Suzawa, T. Kato, K. Okura, Y. Yamada, M. Hirose *et al.*, “High-temperature superconducting cable technology and development trends,” *SEI Technical Review*, vol. 59, no. 7, p. 13, 2005.
- [31] L. Xiao and L. Lin, “Recent progress of power application of superconductor in china,” *IEEE Transactions on Applied Superconductivity*, vol. 17, no. 2, pp. 2355–2360, 2007.
- [32] H. Okubo, M. Noe, J. Cho, A. Malozemoff, L. Martini, S. Nagaya, F. Schmidt, C. Sumereder, P. Tixador, B. Wacker *et al.*, “Status of development and field test experience with high-temperature superconducting power equipment,” *Electra*, no. 250, pp. 61–63, 2010.
- [33] J. Maguire, F. Schmidt, S. Bratt, T. Welsh, J. Yuan, A. Allais, and F. Hamber, “Development and demonstration of a HTS power cable to operate in the long island power authority transmission grid,” *IEEE Transactions on Applied Superconductivity*, vol. 17, no. 2, pp. 2034–2037, 2007.
- [34] H. Zhang and Y. Wang, “A self-shielding DC HTS cable using coaxial configuration with large current capacity,” *IEEE transactions on applied superconductivity*, vol. 26, no. 7, pp. 1–5, 2016.
- [35] W. V. Hassenzahl, D. W. Hazelton, B. K. Johnson, P. Komarek, M. Noe, and C. T. Reis, “Electric power applications of superconductivity,” *Proceedings of the IEEE*, vol. 92, no. 10, pp. 1655–1674, 2004.
- [36] M. Nassi, N. Kelley, P. Ladie, P. Corsato, G. Coletta, and D. Von Dollen, “Qualification results of a 50 m-115 kV warm dielectric cable system,” *IEEE transactions on applied superconductivity*, vol. 11, no. 1, pp. 2355–2358, 2001.

- [37] Z. Melhem, *High temperature superconductors (HTS) for energy applications*. Elsevier, 2011.
- [38] S. Jia, R. Qu, J. Li, H. Fang, and D. Li, "A novel vernier reluctance fully superconducting direct drive synchronous generator with concentrated windings for wind power application," *IEEE Transactions on Applied Superconductivity*, vol. 26, no. 7, pp. 1–5, 2016.
- [39] B. Maples, M. Hand, and W. Musial, "Comparative assessment of direct drive high temperature superconducting generators in multi-megawatt class wind turbines," National Renewable Energy Lab.(NREL), Golden, CO (United States), Tech. Rep., 2010.
- [40] M. Saruwatari, K. Yun, M. Iwakuma, K. Tamura, Y. Hase, Y. Sasamori, and T. Izumi, "Design study of 15-MW fully superconducting generators for offshore wind turbine," *IEEE Transactions on Applied Superconductivity*, vol. 26, no. 4, pp. 1–5, 2016.
- [41] X. Li, H. Wang, C. Jiang, R. Li, and Y. Tang, "Field winding design for a 12 MW offshore superconducting wind generator," in *2016 IEEE 8th International Power Electronics and Motion Control Conference (IPEMC-ECCE Asia)*. IEEE, 2016, pp. 837–841.
- [42] G. Klaus, M. Wilke, J. Fraunhofer, W. Nick, and H.-W. Neumuller, "Design challenges and benefits of HTS synchronous machines," in *2007 IEEE Power Engineering Society General Meeting*. IEEE, 2007, pp. 1–8.
- [43] X. Song, N. Mijatovic, B. B. Jensen, and J. Holbøll, "Design study of fully superconducting wind turbine generators," *IEEE Transactions on Applied Superconductivity*, vol. 25, no. 3, pp. 1–5, 2015.
- [44] Y. Terao, M. Sekino, and H. Ohsaki, "Comparison of conventional and superconducting generator concepts for offshore wind turbines," *IEEE Transactions on Applied Superconductivity*, vol. 23, no. 3, pp. 5 200 904–5 200 904, 2012.
- [45] M. Noe and M. Steurer, "High-temperature superconductor fault current limiters: concepts, applications, and development status," *Superconductor science and technology*, vol. 20, no. 3, p. R15, 2007.
- [46] J. Kozak, T. Janowski, S. Kozak, H. Malinowski, G. Wojtasiewicz, and B. Kondratowicz-Kucewicz, "Design and testing of 230 V inductive type of superconducting fault current limiter with an open core," *IEEE Transactions on applied superconductivity*, vol. 15, no. 2, pp. 2031–2034, 2005.
- [47] S. Abbott, D. Robinson, S. Perera, F. Darmann, C. Hawley, and T. Beales, "Simulation of HTS saturable core-type FCLs for MV distribution systems," *IEEE Transactions on Power Delivery*, vol. 21, no. 2, pp. 1013–1018, 2006.

- [48] Y. Xin, W. Gong, H. Hong, Y. Gao, X. Niu, J. Zhang, Y. Sun, A. Ren, H. Wang, L. Zhang *et al.*, “Development of a 220 kV/300 MVA superconductive fault current limiter,” *Superconductor Science and Technology*, vol. 25, no. 10, p. 105011, 2012.
- [49] M. Endo, T. Hori, T. Koyama, K. Kaiho, I. Yamaguchi, K. Arai, H. Mizoguchi, and S. Yanabu, “Development of a superconducting fault current limiter using various high-speed circuit breakers,” *IET electric power applications*, vol. 3, no. 4, pp. 363–370, 2009.
- [50] B. Lee, K. Park, J. Sim, I. Oh, H. Lee, H. Kim, and O. Hyun, “Design and experiments of novel hybrid type superconducting fault current limiters,” *IEEE transactions on applied superconductivity*, vol. 18, no. 2, pp. 624–627, 2008.
- [51] C. Neumann, “Superconducting fault current limiter (SFCL) in the medium and high voltage grid,” in *2006 IEEE Power Engineering Society General Meeting*. IEEE, 2006, pp. 6–pp.
- [52] L. Kovalsky, X. Yuan, K. Tekletsadik, A. Keri, J. Bock, and F. Breuer, “Applications of superconducting fault current limiters in electric power transmission systems,” *IEEE Transactions on Applied Superconductivity*, vol. 15, no. 2, pp. 2130–2133, 2005.
- [53] M. Noe, O. Hyun, Y. Yoon, and H. Jagels, “Investigation of the feasibility of superconducting fault current limiters in seoul and berlin,” in *Proc. of EUCAS2003*, 2003, pp. 14–18.
- [54] F. Liang, “Non-inductive solenoid coils based on second generation high-temperature superconductors and their application in fault current limiters,” Ph.D. dissertation, University of Bath, 2017.
- [55] E. Sissimatos and B. R. Oswald, “High-temperature superconducting power transformers with fault current limiting properties,” *Physica C: Superconductivity*, vol. 372, pp. 1698–1701, 2002.
- [56] Y. Ohtsubo, M. Iwakuma, S. Sato, K. Sakaki, A. Tomioka, T. Miyayama, M. Konno, H. Hayashi, H. Okamoto, Y. Gosho *et al.*, “Development of REBCO superconducting transformers with a current limiting function—fabrication and tests of 6.9 kV-400 kVA transformers,” *IEEE Transactions on Applied Superconductivity*, vol. 25, no. 3, pp. 1–5, 2014.
- [57] M. Iwakuma, K. Sakaki, A. Tomioka, T. Miyayama, M. Konno, H. Hayashi, H. Okamoto, Y. Gosho, T. Eguchi, S. Yoshida *et al.*, “Development of a $3\sqrt{3}$ -66/6.9 kV-2 MVA REBCO superconducting transformer,” *IEEE Transactions on Applied Superconductivity*, vol. 25, no. 3, pp. 1–6, 2014.

- [58] S.-H. Kim, W.-S. Kim, K.-D. Choi, H.-G. Joo, G.-W. Hong, J.-H. Han, H.-G. Lee, J.-H. Park, H.-S. Song, and S.-y. Hahn, "Characteristic tests of a 1 MVA single phase HTS transformer with concentrically arranged windings," *IEEE transactions on applied superconductivity*, vol. 15, no. 2, pp. 2214–2217, 2005.
- [59] H. Zueger, "630 kVA high temperature superconducting transformer," *Cryogenics*, vol. 38, no. 11, pp. 1169–1172, 1998.
- [60] H. Chen, T. N. Cong, W. Yang, C. Tan, Y. Li, and Y. Ding, "Progress in electrical energy storage system: A critical review," *Progress in natural science*, vol. 19, no. 3, pp. 291–312, 2009.
- [61] K. Alanne and A. Saari, "Distributed energy generation and sustainable development," *Renewable and sustainable energy reviews*, vol. 10, no. 6, pp. 539–558, 2006.
- [62] A. J. Cavallo, "Energy storage technologies for utility scale intermittent renewable energy systems," *J. Sol. Energy Eng.*, vol. 123, no. 4, pp. 387–389, 2001.
- [63] F. R. McLarnon and E. J. Cairns, "Energy storage," *Annual review of energy*, vol. 14, no. 1, pp. 241–271, 1989.
- [64] S. G. Chalk and J. F. Miller, "Key challenges and recent progress in batteries, fuel cells, and hydrogen storage for clean energy systems," *Journal of Power Sources*, vol. 159, no. 1, pp. 73–80, 2006.
- [65] M. Lazarewicz and J. Arseneaux, "Flywheel-based frequency regulation demonstration projects status," in *Proceedings of EESAT conference, San Francisco, USA*, 2005, pp. 1–22.
- [66] J. W. Shim, Y. Cho, S.-J. Kim, S. W. Min, and K. Hur, "Synergistic control of smes and battery energy storage for enabling dispatchability of renewable energy sources," *IEEE transactions on applied superconductivity*, vol. 23, no. 3, pp. 5 701 205–5 701 205, 2013.
- [67] P. McGuckin and G. Burt, "Overview and assessment of superconducting technologies for power grid applications," in *2018 53rd International Universities Power Engineering Conference (UPEC)*. IEEE, 2018, pp. 1–6.
- [68] A. Morandi, A. Anemona, G. Angeli, M. Breschi, A. Della Corte, C. Ferdeghini, C. Gandolfi, G. Grandi, G. Grasso, L. Martini *et al.*, "The DRYSMES4GRID project: development of a 500 kJ/200 kW cryogen-free cooled SMES demonstrator based on MgB₂," *IEEE Transactions on Applied Superconductivity*, vol. 28, no. 4, pp. 1–5, 2018.

- [69] S. Nomura, T. Shintomi, S. Akita, T. Nitta, R. Shimada, and S. Meguro, "Technical and cost evaluation on smes for electric power compensation," *IEEE Transactions on Applied Superconductivity*, vol. 20, no. 3, pp. 1373–1378, 2010.
- [70] S. Nagaya, N. Hirano, H. Moriguchi, K. Shikimachi, H. Nakabayashi, S. Hanai, J. Inagaki, S. Ioka, and S. Kawashima, "Field test results of the 5 MVA SMES system for bridging instantaneous voltage dips," *IEEE transactions on applied superconductivity*, vol. 16, no. 2, pp. 632–635, 2006.
- [71] T. Katagiri, H. Nakabayashi, Y. Nijo, T. Tamada, T. Noda, N. Hirano, T. Nagata, S. Nagaya, M. Yamane, Y. Ishii *et al.*, "Field test result of 10MVA/20MJ SMES for load fluctuation compensation," *IEEE Transactions on Applied Superconductivity*, vol. 19, no. 3, pp. 1993–1998, 2009.
- [72] S. M. Said, M. M. Aly, and M. Abdel-Akher, "Application of superconducting magnetic energy storage (SMES) for voltage sag/swell suppression in distribution system with wind power penetration," in *2014 16th International Conference on Harmonics and Quality of Power (ICHQP)*. IEEE, 2014, pp. 92–96.
- [73] T. Li, Y. Chen, H. Y. Gou, X. Y. Chen, M. G. Tang, and Y. Lei, "A DC voltage swell compensator based on SMES emulator and lead-acid battery," *IEEE Transactions on Applied Superconductivity*, vol. 29, no. 2, pp. 1–4, 2019.
- [74] H. Alafnan, M. Zhang, W. Yuan, J. Zhu, J. Li, M. Elshiekh, and X. Li, "Stability improvement of DC power systems in an all-electric ship using hybrid SMES/battery," *IEEE Transactions on Applied Superconductivity*, vol. 28, no. 3, pp. 1–6, 2018.
- [75] H. Jiang and C. Zhang, "A method of boosting transient stability of wind farm connected power system using S magnetic energy storage unit," *IEEE Transactions on Applied Superconductivity*, vol. 29, no. 2, pp. 1–5, 2019.
- [76] H.-y. Jung, D.-J. Park, H.-R. Seo, M. Park, and I.-K. Yu, "Power quality enhancement of grid-connected wind power generation system by SMES," in *2009 IEEE/PES Power Systems Conference and Exposition*. IEEE, 2009, pp. 1–6.
- [77] W. Xian, W. Yuan, Y. Yan, and T. Coombs, "Minimize frequency fluctuations of isolated power system with wind farm by using superconducting magnetic energy storage," in *2009 International Conference on Power Electronics and Drive Systems (PEDS)*. IEEE, 2009, pp. 1329–1332.
- [78] C.-J. Wu and Y.-S. Lee, "Application of simultaneous active and reactive power modulation of superconducting magnetic energy storage unit to damp turbine-generator subsynchronous oscillations," *IEEE Transactions on Energy Conversion*, vol. 8, no. 1, pp. 63–70, 1993.

- [79] V. T. Tran, M. R. Islam, K. M. Muttaqi, and D. Sutanto, "A novel application of magnesium Di-boride superconducting energy storage to mitigate the power fluctuations of single-phase PV systems," *IEEE Transactions on Applied Superconductivity*, vol. 29, no. 2, pp. 1–5, 2019.
- [80] A. M. Gee, F. Robinson, and W. Yuan, "A superconducting magnetic energy storage-emulator/battery supported dynamic voltage restorer," *IEEE Transactions on Energy Conversion*, vol. 32, no. 1, pp. 55–64, 2016.
- [81] P. Tixador, "13 - superconducting magnetic energy storage (SMES) systems," in *Electricity Transmission, Distribution and Storage Systems*, ser. Woodhead Publishing Series in Energy, Z. Melhem, Ed. Woodhead Publishing, 2013, pp. 442 – 477. [Online]. Available: <http://www.sciencedirect.com/science/article/pii/B9781845697846500135>
- [82] A. Morandi, L. Trevisani, P. Ribani, M. Fabbri, L. Martini, and M. Bocchi, "Superconducting transformers: key design aspects for power applications," in *Journal of Physics: Conference Series*, vol. 97, no. 1. IOP Publishing, 2008, p. 012318.
- [83] N. Hayakawa, H. Kojima, M. Hanai, and H. Okubo, "Progress in development of superconducting fault current limiting transformer (SFCLT)," *IEEE Transactions on Applied Superconductivity*, vol. 21, no. 3, pp. 1397–1400, 2010.
- [84] M. E. Elshiekh, D.-E. A. Mansour, and A. M. Azmy, "Improving fault ride-through capability of DFIG-based wind turbine using superconducting fault current limiter," *IEEE Transactions on Applied Superconductivity*, vol. 23, no. 3, pp. 5 601 204–5 601 204, 2012.
- [85] W. T. Batista de Sousa, T. Mariano Lessa Assis, A. Polasek, A. M. Monteiro, and R. de Andrade, "Simulation of a superconducting fault current limiter: A case study in the brazilian power system with possible recovery under load," *IEEE Transactions on Applied Superconductivity*, vol. 26, 2016.
- [86] T. Bohno, A. Tomioka, M. Imaizumi, Y. Sanuki, T. Yamamoto, Y. Yasukawa, H. Ono, Y. Yagi, and K. Iwadate, "Development of 66 kV/6.9 kV 2 MV a prototype HTS power transformer," *Physica C: Superconductivity and its applications*, vol. 426, pp. 1402–1407, 2005.
- [87] C. Kurupakorn, H. Kojima, N. Hayakawa, M. Goto, N. Kashima, S. Nagaya, M. Noe, K.-P. Juengst, and H. Okubo, "Recovery characteristics after current limitation of high temperature superconducting fault current limiting transformer (HTC-SFCLT)," *IEEE transactions on applied superconductivity*, vol. 15, no. 2, pp. 1859–1862, 2005.
- [88] H. Okubo, C. Kurupakorn, S. Ito, H. Kojima, N. Hayakawa, F. Endo, and M. Noe, "High-tc superconducting fault current limiting transformer

- (HTc-SFCLT) with 2G coated conductors,” *IEEE Transactions on Applied Superconductivity*, vol. 17, no. 2, pp. 1768–1771, 2007.
- [89] H. Kojima, M. Kotari, T. Kito, N. Hayakawa, M. Hanai, and H. Okubo, “Current limiting and recovery characteristics of 2 MVA class superconducting fault current limiting transformer (SFCLT),” *IEEE Transactions on Applied Superconductivity*, vol. 21, no. 3, pp. 1401–1404, 2010.
 - [90] A. Berger, M. Noe, and A. Kudymow, “Test results of 60 kVA current limiting transformer with full recovery under load,” *IEEE transactions on applied superconductivity*, vol. 21, no. 3, pp. 1384–1387, 2010.
 - [91] P. Bodger, W. Enright, and V. Ho, “A low voltage, mains frequency, partial core, high temperature, superconducting transformer,” 2005.
 - [92] A. C. Laphorn, I. Chew, W. G. Enright, and P. S. Bodger, “HTS transformer: Construction details, test results, and noted failure mechanisms,” *IEEE Transactions on Power Delivery*, vol. 26, no. 1, pp. 394–399, 2010.
 - [93] J. Choi, S. Lee, M. Park, W. Kim, S. Kim, J. Han, H. Lee, and K. Choi, “Design of 154 kV class 100 MVA 3 phase HTS transformer on a common magnetic core,” *Physica C: Superconductivity and its applications*, vol. 463, pp. 1223–1228, 2007.
 - [94] D. Abraimov, A. Ballarino, C. Barth, L. Bottura, R. Dietrich, A. Francis, J. Jaroszynski, G. Majkic, J. McCallister, A. Polyanskii *et al.*, “Double disordered YBCO coated conductors of industrial scale: high currents in high magnetic field,” *Superconductor Science and Technology*, vol. 28, no. 11, p. 114007, 2015.
 - [95] X. Zhang, Z. Zhong, H. Ruiz, J. Geng, and T. A. Coombs, “General approach for the determination of the magneto-angular dependence of the critical current of YBCO coated conductors,” *Superconductor Science and Technology*, vol. 30, no. 2, p. 025010, 2016.
 - [96] B. Lin, L. Ying, J. Sheng, J. Zhang, L. Yao, Y. Li, Z. Jin, and Z. Hong, “Test of maximum endurable quenching voltage of YBCO-coated conductors for resistive superconducting fault current limiter,” *IEEE Transactions on Applied Superconductivity*, vol. 22, no. 3, pp. 5 602 904–5 602 904, 2011.
 - [97] F. Liang, W. Yuan, C. A. Baldan, M. Zhang, and J. S. Lamas, “Modeling and experiment of the current limiting performance of a resistive superconducting fault current limiter in the experimental system,” *Journal of Superconductivity and Novel Magnetism*, vol. 28, no. 9, pp. 2669–2681, 2015.
 - [98] T. Jin, J.-p. Hong, H. Zheng, K. Tang, and Z.-h. Gan, “Measurement of boiling heat transfer coefficient in liquid nitrogen bath by inverse heat

- conduction method,” *Journal of Zhejiang University-SCIENCE A*, vol. 10, no. 5, pp. 691–696, 2009.
- [99] D. C. Giancoli, *Physics for scientists & engineers with modern physics*. Pearson Education, 2008, vol. 2.
 - [100] M. Zhang, K. Matsuda, and T. Coombs, “New application of temperature-dependent modelling of high temperature superconductors: Quench propagation and pulse magnetization,” *Journal of Applied Physics*, vol. 112, no. 4, p. 043912, 2012.
 - [101] J. Zhu, W. Yuan, M. Qiu, B. Wei, H. Zhang, P. Chen, Y. Yang, M. Zhang, X. Huang, and Z. Li, “Experimental demonstration and application planning of high temperature superconducting energy storage system for renewable power grids,” *Applied energy*, vol. 137, pp. 692–698, 2015.
 - [102] R. Boom and H. Peterson, “Superconductive energy storage for power systems,” *IEEE Transactions on Magnetics*, vol. 8, no. 3, pp. 701–703, 1972.
 - [103] J. Zhu, X. Bao, B. Yang, P. Chen, Y. Yang, and M. Qiu, “Dynamic simulation test research on power fluctuation compensation using hybrid SMES of YBCO and BSCCO tapes,” *IEEE Transactions on Applied Superconductivity*, vol. 22, no. 3, pp. 5 700 404–5 700 404, 2011.
 - [104] M. H. Ali, B. Wu, and R. A. Dougal, “An overview of SMES applications in power and energy systems,” *IEEE Transactions on Sustainable Energy*, vol. 1, no. 1, pp. 38–47, 2010.
 - [105] S. Schoenung, R. Bieri, W. Meier, and T. Bickel, “Cost savings and prospects for applications of micro superconducting magnetic energy storage (SMES) using high temperature superconductors,” *IEEE transactions on applied superconductivity*, vol. 3, no. 1, pp. 200–203, 1993.
 - [106] D. Lieurance, F. Kimball, C. Rix, and C. Luongo, “Design and cost studies for small scale superconducting magnetic energy storage (SMES) systems,” *IEEE Transactions on applied superconductivity*, vol. 5, no. 2, pp. 350–353, 1995.
 - [107] A. Ichinose, H. Kasahara, H. Sakaki, S. Akita, A. Ishiyama, A. Maruyama, and S. Koso, “Research and development of high-T/sub c/SMES,” *IEEE transactions on applied superconductivity*, vol. 15, no. 2, pp. 1947–1950, 2005.
 - [108] M. Green and B. Strauss, “Estimating the operating cost of superconducting magnet systems at various operating temperatures,” *IEEE Transactions on Applied Superconductivity*, vol. 26, no. 4, pp. 1–5, 2016.

- [109] X. Zhou, Y. Tang, S. Jing, C. Zhang, K. Gong, L. Zhang, and Y. Li, "Cost estimation models of MJ class HTS superconducting magnetic energy storage magnets," *IEEE Transactions on Applied Superconductivity*, vol. 28, no. 4, pp. 1–5, 2018.
- [110] M. A. Green and B. P. Strauss, "The cost of superconducting magnets as a function of stored energy and design magnetic induction times the field volume," *IEEE Transactions on Applied Superconductivity*, vol. 18, no. 2, pp. 248–251, 2008.
- [111] R. Soman, H. Ravindra, X. Huang, K. Schoder, M. Steurer, W. Yuan, M. Zhang, S. Venuturumilli, and X. Chen, "Preliminary investigation on economic aspects of superconducting magnetic energy storage (SMES) systems and high-temperature superconducting (HTS) transformers," *IEEE Transactions on Applied Superconductivity*, vol. 28, no. 4, pp. 1–5, 2018.
- [112] M. A. Green and B. P. Strauss, "Things to think about when estimating the cost of magnets made with conductors other than Nb-Ti," *IEEE Transactions on Applied Superconductivity*, vol. 27, no. 4, pp. 1–5, 2016.
- [113] Y. Xu, L. Ren, Y. Tang, C. Xu, Z. Zhang, W. Chen, J. Li, J. Shi, and L. Chen, "A study on the design and comparison of 1–100-MJ-class SMES magnet with different coil configurations," *IEEE Transactions on Applied Superconductivity*, vol. 27, no. 5, pp. 1–9, 2017.
- [114] L. Ren, Y. Xu, W. Zuo, X. Shi, F. Jiao, Y. Liu, J. Deng, J. Li, J. Shi, S. Wang *et al.*, "Development of a movable HTS SMES system," *IEEE Transactions on Applied Superconductivity*, vol. 25, no. 4, pp. 1–9, 2015.
- [115] K. Shikimachi, H. Moriguchi, N. Hirano, S. Nagaya, T. Ito, J. Inagaki, S. Hanai, M. Takahashi, and T. Kurusu, "Development of MVA class HTS SMES system for bridging instantaneous voltage dips," *IEEE transactions on applied superconductivity*, vol. 15, no. 2, pp. 1931–1934, 2005.
- [116] L. Chen, H. He, L. Zhu, F. Guo, Z. Shu, X. Shu, and J. Yang, "Coordinated control of SFCL and SMES for transient performance improvement of microgrid with multiple DG units," *Canadian Journal of Electrical and Computer Engineering*, vol. 39, no. 2, pp. 158–167, 2016.
- [117] C. Huang, X. Y. Xiao, Z. Zheng, and Y. Wang, "Cooperative control of SFCL and SMES for protecting PMSG-based WTG s under grid faults," *IEEE Transactions on Applied Superconductivity*, vol. 29, no. 2, pp. 1–6, 2019.
- [118] G. Zhu, Z. Wang, and G. Zhang, "Research on a combined device SMES-SFCL based on multi-object optimization," *IEEE transactions on applied superconductivity*, vol. 15, no. 2, pp. 2019–2022, 2005.

- [119] I. Ngamroo, "Optimization of SMES-FCL for augmenting FRT performance and smoothing output power of grid-connected DFIG wind turbine," *IEEE Transactions on Applied Superconductivity*, vol. 26, no. 7, pp. 1–5, 2016.
- [120] I. Ngamroo and T. Karaipoom, "Improving low-voltage ride-through performance and alleviating power fluctuation of DFIG wind turbine in DC microgrid by optimal SMES with fault current limiting function," *IEEE transactions on Applied Superconductivity*, vol. 24, no. 5, pp. 1–5, 2014.
- [121] W. Guo, L. Xiao, and S. Dai, "Enhancing low-voltage ride-through capability and smoothing output power of DFIG with a superconducting fault-current limiter-magnetic energy storage system," *IEEE Transactions on Energy Conversion*, vol. 27, no. 2, pp. 277–295, 2012.
- [122] J. Li, M. Zhang, Q. Yang, Z. Zhang, and W. Yuan, "SMES/battery hybrid energy storage system for electric buses," *IEEE Transactions on Applied Superconductivity*, vol. 26, no. 4, pp. 1–5, 2016.
- [123] S.-y. Lu, L. Wang, T.-M. Lo, and A. V. Prokhorov, "Integration of wind power and wave power generation systems using a DC microgrid," *IEEE Transactions on Industry Applications*, vol. 51, no. 4, pp. 2753–2761, 2014.
- [124] B. Liu, F. Zhuo, Y. Zhu, and H. Yi, "System operation and energy management of a renewable energy-based DC micro-grid for high penetration depth application," *IEEE Transactions on Smart Grid*, vol. 6, no. 3, pp. 1147–1155, 2014.
- [125] M. Sechilariu, F. Locment, and L. T. Dos Santos, "A conceptual framework for full optimal operation of a grid-connected DC microgrid," in *2018 IEEE International Conference on Industrial Electronics for Sustainable Energy Systems (IESES)*. IEEE, 2018, pp. 296–301.
- [126] F. Perez, A. Iovine, G. Damm, and P. Ribeiro, "DC microgrid voltage stability by dynamic feedback linearization," in *2018 IEEE International Conference on Industrial Technology (ICIT)*. IEEE, 2018, pp. 129–134.
- [127] R. Kaur, V. Krishnasamy, and N. K. Kandasamy, "Optimal sizing of wind-PV-based DC microgrid for telecom power supply in remote areas," *IET Renewable Power Generation*, vol. 12, no. 7, pp. 859–866, 2018.
- [128] D. M. Yehia, D.-E. A. Mansour, and W. Yuan, "Fault ride-through enhancement of PMSG wind turbines with DC microgrids using resistive-type SFCL," *IEEE Transactions on Applied Superconductivity*, vol. 28, no. 4, pp. 1–5, 2018.
- [129] G. Shi, X. Cai, C. Sun, Y. Chang, and R. Yang, "All-DC offshore wind farm with parallel connection: An overview," 2016.

- [130] G. Shi, J. Zhang, X. Cai, and M. Zhu, "Decoupling control of series-connected DC wind turbines with energy storage system for offshore DC wind farm," in *2016 IEEE 7th International Symposium on Power Electronics for Distributed Generation Systems (PEDG)*. IEEE, 2016, pp. 1–6.
- [131] J.-D. Park and J. Candelaria, "Fault detection and isolation in low-voltage DC-bus microgrid system," *IEEE transactions on power delivery*, vol. 28, no. 2, pp. 779–787, 2013.
- [132] P. Ruffing, N. Collath, C. Brantl, and A. Schnettler, "Dc fault control and high-speed switch design for an HVDC network protection based on fault-blocking converters," *IEEE Transactions on Power Delivery*, vol. 34, no. 1, pp. 397–406, 2018.
- [133] M. Barnes and A. Beddard, "Voltage source converter HVDC links—the state of the art and issues going forward," *Energy Procedia*, vol. 24, pp. 108–122, 2012.
- [134] X. Pei, O. Cwikowski, A. C. Smith, and M. Barnes, "Design and experimental tests of a superconducting hybrid DC circuit breaker," *IEEE Transactions on Applied Superconductivity*, vol. 28, no. 3, pp. 1–5, 2018.
- [135] D. Salomonsson, L. Soder, and A. Sannino, "Protection of low-voltage DC microgrids," *IEEE Transactions on power delivery*, vol. 24, no. 3, pp. 1045–1053, 2009.
- [136] H.-Y. Lee, M. Asif, K.-H. Park, and B.-W. Lee, "Feasible protection strategy for HVDC system by means of SFCL and passive resonance DC breaker," *The Journal of Engineering*, vol. 2019, no. 16, pp. 767–770, 2018.
- [137] L. Xiao, C. Sheng, Q. Lu, and M. Song, "Research on application and configuration of SFCL in VSC-HVDC of CSG," in *2018 2nd IEEE Conference on Energy Internet and Energy System Integration (EI2)*. IEEE, 2018, pp. 1–6.
- [138] Y. Morishita, T. Ishikawa, I. Yamaguchi, S. Okabe, G. Ueta, and S. Yanabu, "Applications of DC breakers and concepts for superconducting fault-current limiter for a DC distribution network," *IEEE Transactions on Applied Superconductivity*, vol. 19, no. 4, pp. 3658–3664, 2009.
- [139] S. Kar and V. Rao, "Comparative study on the fastest effective fault limitation for stabilized and stabilizer-free high τ_c superconductors," *Physica C: Superconductivity and its Applications*, vol. 541, pp. 50–54, 2017.
- [140] B. Touaiti, M. Moujahed, H. Ben Azza, and M. Jemli, "Fault-tolerant VSI for stand-alone DFIG feeding an isolated DC load," *International Journal of Electronics*, vol. 105, no. 10, pp. 1769–1784, 2018.

- [141] X. Yi and H. Nian, "Novel DC grid connection topology and control strategy for DFIG-based wind power generation system," in *2013 International Conference on Electrical Machines and Systems (ICEMS)*. IEEE, 2013, pp. 223–228.
- [142] M. F. Iacchetti, G. D. Marques, and R. Perini, "Operation and design issues of a doubly fed induction generator stator connected to a DC net by a diode rectifier," *IET Electric power applications*, vol. 8, no. 8, pp. 310–319, 2014.
- [143] —, "Torque ripple reduction in a DFIG-DC system by resonant current controllers," *IEEE Transactions on Power Electronics*, vol. 30, no. 8, pp. 4244–4254, 2014.
- [144] C. Wu and H. Nian, "Sinusoidal current operation of a DFIG-DC system without stator voltage sensors," *IEEE Transactions on Industrial Electronics*, vol. 65, no. 8, pp. 6250–6258, 2017.
- [145] G. D. Marques and M. F. Iacchetti, "Minimization of torque ripple in the DFIG-DC system via predictive delay compensation," *IEEE Transactions on Industrial Electronics*, vol. 65, no. 1, pp. 103–113, 2017.
- [146] Y. Xu, Y. Li, L. Ren, C. Xu, Y. Tang, J. Li, L. Chen, and B. Jia, "Research on the application of superconducting magnetic energy storage in micro-grids for smoothing power fluctuation caused by operation mode switching," *IEEE Transactions on Applied Superconductivity*, vol. 28, no. 4, pp. 1–6, 2018.
- [147] D. M. Yehia, D.-E. A. Mansour, and W. Yuan, "Overcurrent and overvoltage testing of a multifunctional superconducting coil," in *2018 53rd International Universities Power Engineering Conference (UPEC)*. IEEE, 2018, pp. 1–4.
- [148] J. J. Justo, F. Mwasilu, and J.-W. Jung, "Doubly-fed induction generator based wind turbines: A comprehensive review of fault ride-through strategies," *Renewable and sustainable energy reviews*, vol. 45, pp. 447–467, 2015.
- [149] J. Li and K. Corzine, "A sensorless flux oriented control scheme for a DFIG connected to a DC link," in *2015 Clemson University Power Systems Conference (PSC)*. IEEE, 2015, pp. 1–5.
- [150] X. Wang, X. Cui, G. Tergemessova, Q. Liu, H. Zhang, and J. Lai, "Behavior of responding to sudden change of standalone DC load supplied by a DFIG with different frequency in AC side," in *2017 Asian Conference on Energy, Power and Transportation Electrification (ACEPT)*. IEEE, 2017, pp. 1–5.

- [151] R. D. Shukla, R. K. Tripathi, and P. Thakur, “Dc grid/bus tied DFIG based wind energy system,” *Renewable Energy*, vol. 108, pp. 179–193, 2017.